Reply to Reviewer Comments

"Development of SOLWEIG-LEB v1.0: An urban radiation model integrating LAD-based canopy shortwave attenuation and leaf energy balance"

We appreciate the reviewer's time and effort in evaluating our manuscript. We are grateful for the insightful comments and constructive suggestions, which have improved the clarity and scope of the evaluation.

Author's Response to Reviewer 1

General Comments
The manuscript introduces LAD-based canopy attenuation and a leaf energy balance module into SOLWEIG. This is a potentially useful extension, but the demonstrated contribution is incremental (my major concern), the validation is limited, and the improvement in predictive performance is modest. I recommend major revision.

→ We sincerely thank the reviewer for the constructive critique regarding the scope of validation and the demonstrated contribution of the individual model components. We fully recognize that the validation in the original manuscript was constrained in both duration and scope. To thoroughly address this, we have incorporated a comprehensive 7-day dataset (29 July – 4 August 2020) from a reduced-scale street-canyon experiment in Angers, France (Herpin et al., 2024; Section 3.1 and 4.1). This dataset allowed us to evaluate 1) voxel-scale leaf temperature across multiple canopy locations (RMSE reduced from 1.82 to 1.72 °C in Region A, and from 2.19 to 1.61 °C in Region B relative to the isothermal baseline), 2) vertical PAR attenuation at three measurement heights (r = 0.81–0.99, pooled RMSE of 21.92 and 31.38 W m^{-2}), 3) tree-level daily transpiration derived from voxel-scale latent heat fluxes (r = 0.71–0.94, RMSE of 0.26–0.85 L $tree^{-1}$), and 4) pedestrian-level MRT in both vegetated and non-vegetated canyon sections. In addition, the leaf-temperature validation in Mainz, Germany, was expanded from two to four distinct sky conditions (clear-sky, slightly cloudy, mostly cloudy, and fully cloudy; Appendix B).

→ To clarify the core contributions and distinct scopes of the modules, we have substantially revised the manuscript (Sections 1, 5.1, and 5.2) to emphasize that SOLWEIG-LEB extends the existing SOLWEIG framework by incorporating voxel-scale leaf temperature and energy-flux diagnostics while retaining its primary focus on pedestrian radiative environments. Specifically, the LAD-based canopy attenuation module directly targets the primary driver of pedestrian-level radiant exposure (T_{mrt}), explaining over 97% of the total MRT error reduction in Göteborg by replacing the conventional static bulk transmissivity with 3D path-dependent extinction. Meanwhile, the principal value of the Leaf Energy Balance (LEB) module lies not in marginally adjusting pedestrian T_{mrt}, but in replacing the isothermal vegetation-temperature assumption ($T_{veg} = T_{air}$). By explicitly resolving three-

dimensional leaf temperature variations—which exceeded ambient air temperature by approximately 5 °C in Angers—and quantifying intra-canopy sensible and latent heat partitioning, the LEB module provides critical biophysical diagnostics and essential boundary conditions for future atmospheric/CFD coupling and BVOC emission modeling.

→ Detailed point-by-point responses to each specific concern are provided below.

Comment 1
The added value of the full model is insufficiently demonstrated. MRT RMSE decreases from 4.76 to 4.38 °C, while the LAD-only configuration already achieves 4.39 °C. Thus, the leaf energy balance contributes almost no additional improvement in MRT under the evaluated conditions. The authors should clarify the practical significance of this component and provide stronger validation of its leaf-temperature and energy-flux outputs.

→ We appreciate the reviewer's constructive comment. As pointed out by the reviewer, we agree that the improvement in pedestrian-level MRT accuracy under the conditions evaluated in Göteborg was primarily attributable to LAD-based canopy attenuation, while the additional contribution of the LEB module was quantitatively small, with MRT RMSE decreasing from 4.39 to 4.38 °C. This outcome is physically consistent with urban radiative transfer: pedestrian-level radiant load is predominantly governed by the physical interception of intense direct and diffuse shortwave radiation, whereas longwave emission modifications arising from canopy leaf–air temperature differences (typically within ±2 to 3 °C) exert only a secondary radiative influence at pedestrian height.

→ Beyond marginally adjusting pedestrian MRT, the principal objective and practical significance of the LEB module lie in eliminating the isothermal vegetation assumption ($T_{veg} = T_{air}$) used in the original SOLWEIG and resolving three-dimensional canopy biophysical processes that were previously unrepresented in the model. Specifically, the LEB module calculates voxel-scale leaf temperature, net radiation, and the partitioning between sensible and latent heat fluxes, capturing intra-canopy thermal gradients (where leaf temperatures exceeded air temperature by approximately 5 °C in sunlit leaves) and quantifying transpirational water loss. Furthermore, these voxel-scale heat and moisture fluxes provide essential volumetric source and sink terms for future coupling with computational fluid dynamics (CFD) or multi-layer urban canopy models, as well as critical biophysical inputs for biogenic volatile organic compound (BVOC) emission modeling. We clarified this development objective and the distinct roles of LAD-based attenuation and the LEB module in Sections 5.1 and 5.2 of the revised manuscript, emphasizing that LAD-based attenuation primarily governs pedestrian-level MRT accuracy, whereas the LEB module provides indispensable capabilities for diagnosing intra-canopy thermal states and turbulent energy exchange.

→ In response to the reviewer's concern that the original manuscript provided insufficient validation of leaf temperature and energy-exchange processes, we conducted an additional evaluation using observations from a reduced-scale street-canyon experiment in Angers, France (Sections 3.1 and 4.1). In Angers, leaf temperature, PAR, transpiration, and MRT were evaluated in two vegetated regions with different canopy conditions and LAI values. Compared with the Legacy configuration, which assumes leaf temperature equals air temperature, the region-specific leaf-temperature RMSE of SOLWEIG-LEB decreased from 1.82 to 1.72 °C in region A and from 2.19 to 1.61 °C in region B, with correlation coefficients reaching 0.97 in both regions. Although the degree of improvement varied among individual observation locations due to leaf-scale orientation, the diurnal heating and

cooling patterns were well captured. In addition, to evaluate canopy energy and moisture exchange, the latent heat fluxes calculated by the LEB module were integrated across crown leaf areas to estimate tree-level transpiration. The correlation coefficients for daily cumulative transpiration of the three trees (G, E, and H) were 0.93, 0.94, and 0.71, respectively, with corresponding RMSEs of 0.85, 0.28, and 0.26 L $tree^{-1}$, reproducing the observed day-to-day water consumption. Downward PAR attenuation at three measurement heights (1.1, 1.5, and 2.0 m) was also reliably captured, yielding pooled correlation coefficients of 0.98 and 0.96 and RMSEs of 21.92 and 31.38 W m^{-2} in regions A and B, respectively.

→ We also expanded the Mainz leaf-temperature evaluation from two to four sky conditions covering clear-sky, slightly cloudy, mostly cloudy, and fully cloudy periods, and directly compared SOLWEIG-LEB with the isothermal vegetation assumption used in Legacy SOLWEIG at identical observation times (Appendix B). The results showed reduced leaf-temperature RMSEs under clear-sky and slightly cloudy conditions, demonstrating the predictive advantage of the LEB module under strong solar forcing, whereas improvements were limited under mostly cloudy conditions and Legacy SOLWEIG yielded a lower RMSE under fully cloudy conditions.

→ Through these revisions and additional evaluations, we have more comprehensively demonstrated the predictive performance and limitations of the LEB module, as well as its additional capability to diagnose intra-canopy leaf temperature and vegetation energy and moisture exchange, while retaining the finding that LAD-based attenuation was primarily responsible for improvements in pedestrian-level MRT accuracy.

Now, it reads:

Page 16–19:

3.1. Vegetation and radiative-environment evaluation dataset in Angers

Observations from a reduced-scale street-canyon experiment in Angers, France (Herpin et al., 2024), were used to evaluate within-canopy radiation attenuation, leaf temperature, transpiration, and MRT. The experimental site consisted of a north–south-oriented street canyon and building models on both sides, with a building height, building width, and canyon width of 2 m each (Fig. 2). Ornamental apple trees were present in regions A and B, whereas region C contained no trees (Fig. 2a). Following pruning, the canopy-top height was 1.70 m in both vegetated regions, and the canopy-base heights were 0.60 and 0.69 m in regions A and B, respectively. The corresponding LAI values were 2.49 and 1.91 m^2 m^{-2}. LAD was assumed to be vertically uniform within the canopy (Figs. 2b and c).

MRT was estimated from globe temperatures measured at 0.4 m above ground in the centre of regions A, B, and C. Leaf temperatures were measured at western, central, and eastern positions within the canopies of regions A and B at 1.5 m above ground (Fig. 2d). PAR was

measured within the canopy at heights of 1.1 and 1.5 m and above the canopy at 2.0 m (Fig. 2d). Leaf temperatures were measured using thermocouples attached to the undersides of leaves, and PAR was measured using Solems PAR/LE sensors. MRT was derived by applying a convective correction to temperatures measured using Pt100 sensors installed inside black globes with a diameter of 15 cm (Herpin et al., 2024).

Meteorological forcing consisted of air temperature, relative humidity, downward shortwave and longwave radiation, and wind speed. Radiation, air temperature, and relative humidity were observed in the non-vegetated region C, whereas wind speed was measured between regions B and C at 2 m above ground (Figs. 2e and f). Air temperature and relative humidity were measured using Vaisala HMP sensors, wind speed using an LCJ CV7 ultrasonic anemometer, and radiation using a Kipp & Zonen CNR radiometer (Herpin et al., 2024). Air temperature and wind speed observations at 2 m above ground were used, and direct and diffuse shortwave radiation were partitioned internally from the input global shortwave radiation. Air temperature, relative humidity, and wind speed were applied uniformly across the domain. The evaluation covered seven days from 29 July to 4 August 2020, with simulations performed at 30 min intervals (Fig. 3). Time is expressed in local standard time (LST, UTC+1).

The Legacy reference configuration retained the common non-vegetation settings while applying a fixed canopy transmissivity and prescribing vegetation temperature as $T_{\mathrm{veg}} = T_{\mathrm{air}}$. Representative transmissivity along a vertical path was calculated using the Beer–Lambert law as follows:

$$\tau = \exp\left(-G_{proj}\, LAI\right). \tag{25}$$

Applying $G_{\mathrm{proj}} = 0.5$ to the LAI values of regions A and B yielded vertical-path transmissivities of approximately 29 % and 38 %, respectively. Separate Legacy simulations were conducted using fixed transmissivities of 30 % and 40 %, which approximated these values. Results for regions A were compared with the 30 % simulation, whereas results for regions B and C were compared with the 40 % simulation. SOLWEIG-LEB used a spherical leaf angle distribution ($G_{\mathrm{proj}} = 0.5$) and LAD-based shortwave attenuation, and calculated the leaf energy balance using the CANOAK photosynthesis–stomatal coupling. The characteristic leaf dimension was set to 0.05 m, and the background CO_2 concentration was set to 420 ppm. The horizontal grid spacing was 0.2 m, and the vertical spacing of vegetation voxels was 0.1 m. The leaf energy balance was calculated during both daytime and nighttime, with leaf temperature and vegetation longwave emission updated iteratively. Solid-surface temperatures were calculated using daytime and nighttime empirical equations calibrated against site observations. Wall albedo and emissivity were set to 0.40 and 0.87, respectively, and the corresponding ground values were 0.25 and 0.94. PAR was calculated by applying the model's PAR energy fraction f_{PAR} (= 0.45) to the downward shortwave radiation ($K_{\downarrow}$) at the receiver (Baldocchi, 1994; Harley and Baldocchi, 1995).

Transpiration was evaluated for two trees in region A (G and E) and one tree in region B (H). Herpin et al. (2024) used covers and mulch on the tree containers to minimize rainfall infiltration and soil evaporation, and estimated daily transpiration from soil-water depletion during periods without irrigation or drainage. Changes in soil water content were calculated from volumetric water content measured using two Decagon EC-5 sensors in each container,

with a soil volume of 44.5 L per tree. Observed transpiration was estimated for the period from 06:00 to 20:30 LST. Modelled transpiration per tree (V_{tr}) was calculated by weighting voxel-scale latent heat fluxes by leaf area and integrating over the observation period. Cumulative transpiration per tree (V_{tr}, L tree^{-1}) was calculated as the product of total leaf area per tree (A_{leaf}, m^2 tree^{-1}) and cumulative transpiration per unit leaf area (E_{leaf}, L m^{-2}).

$$\begin{aligned} V_{tr} &= A_{leaf} \cdot E_{leaf} \\ &= A_{leaf} \cdot \frac{10^3}{\rho_w} \int_{t_1}^{t_2} \frac{\overline{LE}(t)}{\lambda_{vap}(t)}\, dt \\ &= A_{leaf} \cdot \frac{10^3}{\rho_w} \int_{t_1}^{t_2} \frac{\sum LE_v(t) LAD_v V_v}{\lambda_{vap}(t) \sum LAD_v V_v}\, dt \end{aligned} \quad . \qquad (26)$$

Here, A_{leaf} was 2.59 and 2.02 m^2 in regions A and B, respectively (Herpin et al., 2024). The mean latent heat flux ($\overline{LE}$) was calculated as the leaf-area-weighted average of the latent heat flux per unit leaf area in each voxel (LE_v), using the total leaf area of the corresponding voxel ($= LAD_v \cdot V_v$) as the weight. LE_v, LAD_v, and V_v denote the latent heat flux per unit one-sided leaf area (W m^{-2}), leaf area density (m^2 m^{-3}), and volume (m^3) of voxel v, respectively. λ_{vap} is the latent heat of vaporization (J kg^{-1}), ρ_w is water density (kg m^{-3}), and 10^3 converts water volume from m^3 to L. The integration interval t_1–t_2 was 06:00–20:30 LST.

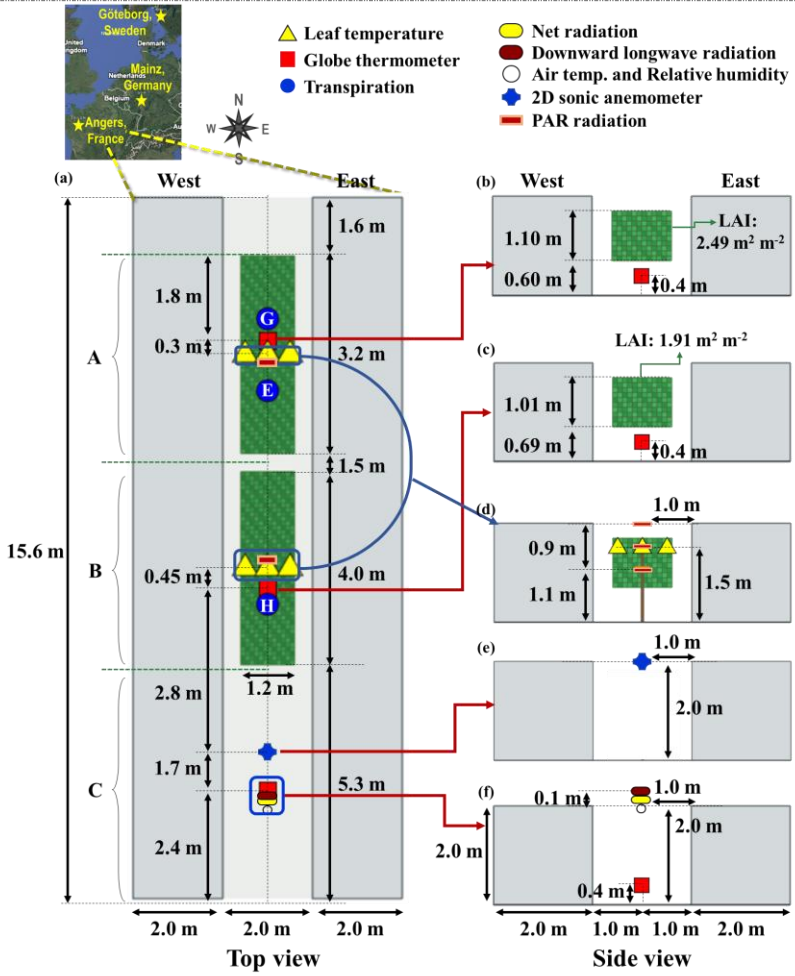

Figure 2. Geometry and instrument layout of the reduced-scale street-canyon experiment in Angers, France, reconstructed based on Herpin et al. (2024). (a) Plan view of the experimental site and measurement locations. (b, c) Canopy geometry, leaf area index (LAI), and MRT measurement locations in regions A and B, respectively. (d) Leaf-temperature and photosynthetically active radiation (PAR) measurement locations in regions A and B. (e) Wind-speed measurement location. (f) Measurement locations for global shortwave radiation, downward longwave radiation, air temperature, relative humidity, and MRT.

Page 25–32:

4.1. Model evaluation using observations from Angers

Observations from Angers were used to evaluate leaf temperature, transpiration, PAR, and MRT calculated by SOLWEIG-LEB. Figure 6 presents observed and simulated leaf temperatures at 1.5 m above ground in regions A and B. Observed leaf temperatures followed diurnal variations similar to those of the background air temperature but occasionally exceeded air temperature by more than 10 °C during daytime. These high leaf temperatures were particularly evident at the western observation point in region B. SOLWEIG-LEB reproduced the overall leaf-temperature variations associated with daytime heating and nighttime cooling and, unlike Legacy SOLWEIG, which assumes leaf temperature equals air temperature, calculated leaf temperatures above air temperature during daytime. However, its leaf-temperature performance varied among observation locations. High daytime leaf temperatures were underestimated at the eastern point in region A and the western point in region B, whereas overestimation occurred during some periods at the western point in region A. The correlation coefficient for temporal leaf-temperature variations increased relative to Legacy SOLWEIG at five observation points, with the central point in region A being the exception, whereas RMSE decreased at only three of the six points. These differences may also be associated with the different spatial scales represented by the observations and the model. The observations were obtained using thermocouples attached to individual leaves, whereas the model calculates a representative temperature for each vegetation voxel, limiting its ability to reproduce all temperature differences associated with the solar exposure and orientation of individual leaves.

When valid paired data from the three observation points were pooled within each region (Table 3), leaf-temperature RMSE decreased from 1.82 °C in Legacy SOLWEIG to 1.72 °C in SOLWEIG-LEB in region A, and from 2.19 to 1.61 °C in region B. The correlation coefficient (r) increased from 0.96 to 0.97 in region A and from 0.95 to 0.97 in region B. MBE also decreased from 0.36 to 0.09 °C and from 0.22 to −0.04 °C, respectively.

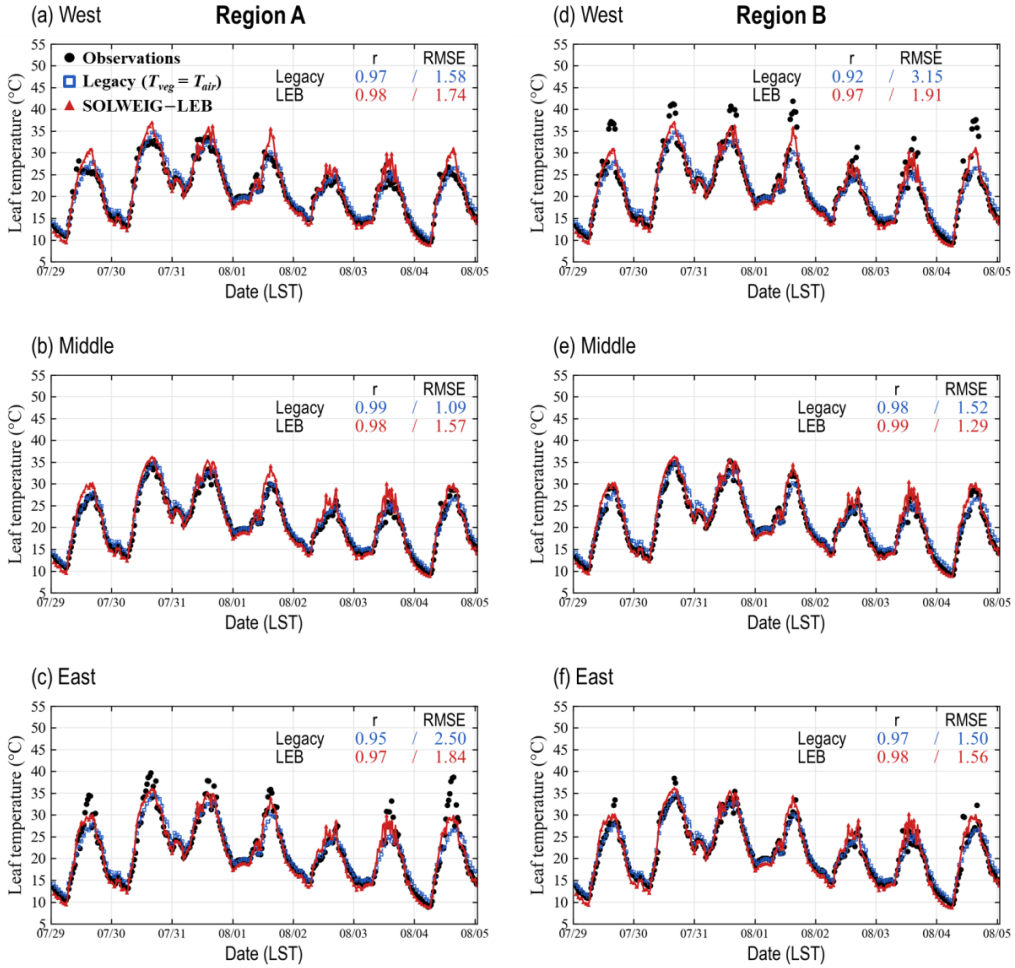

Figure 6. Comparison of observed and simulated leaf temperatures at 1.5 m above ground in vegetated regions A and B in Angers, France. The left column shows comparisons at the (a) western, (b) central, and (c) eastern observation points in region A, and the right column shows those at the (d) western, (e) central, and (f) eastern observation points in region B. Black circles indicate observations, blue open squares indicate Legacy SOLWEIG ($T_{veg} = T_{air}$), and red triangles indicate SOLWEIG-LEB.

Figure 7 compares MRT at 0.4 m above ground in vegetated regions A and B and non-vegetated region C. The MRT RMSEs of SOLWEIG-LEB were 2.32 and 2.20 °C in regions A and B, respectively, lower than the corresponding Legacy SOLWEIG values of 2.53 and 2.30 °C (Table 3). In region A, the mean bias also decreased from 0.77 to 0.39 °C. In region B, however, RMSE decreased slightly while MBE changed from -0.04 to -0.64 °C, indicating greater mean underestimation. Differences between the two models were particularly pronounced around noon, when the MRT overestimation in Legacy SOLWEIG was reduced in SOLWEIG-LEB. This is interpreted as a reduction in transmitted shortwave radiation resulting from the calculation of cumulative LAD-based attenuation along radiative paths in SOLWEIG-LEB, in contrast to the fixed canopy transmissivity used in Legacy SOLWEIG. In region C, where no trees were present, MRT differences between the two models were negligible.

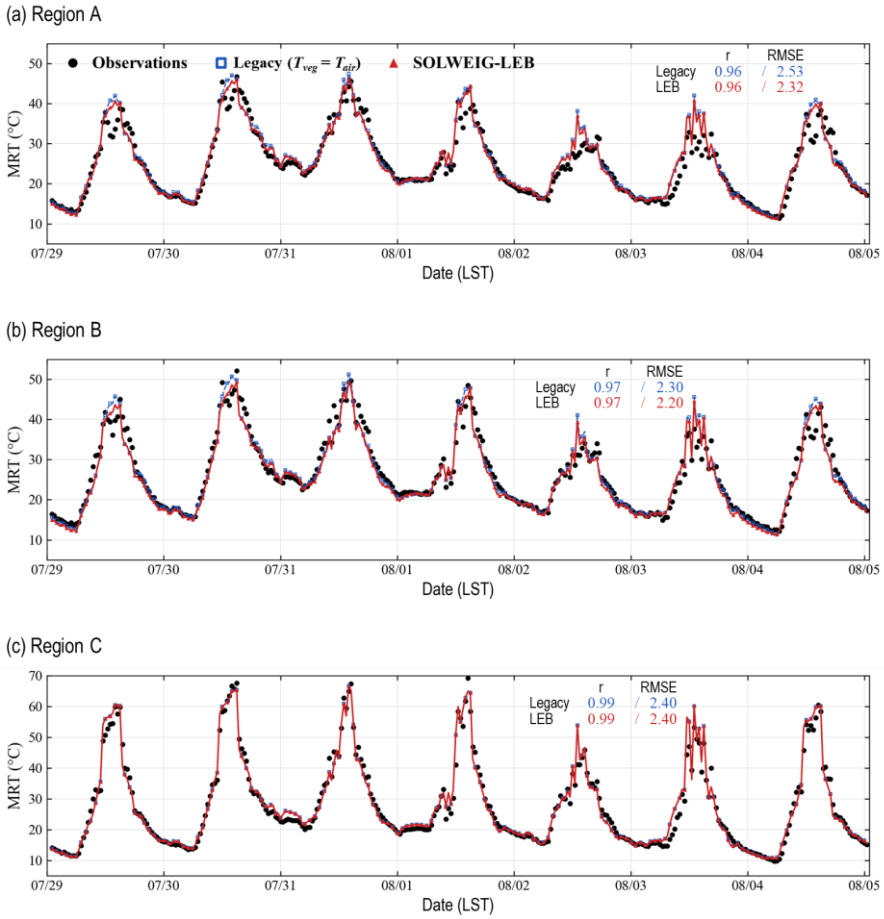

Figure 7. Comparison of observed and simulated mean radiant temperature (MRT) at 0.4 m above ground in vegetated regions A and B and non-vegetated region C in Angers, France. Panels show MRT time series for (a) region A, (b) region B, and (c) region C. Black circles indicate observations, blue open squares indicate Legacy SOLWEIG, and red triangles indicate SOLWEIG-LEB.

Figure 8 compares observed and simulated PAR at different heights in regions A and B in Angers. Observed PAR was high above the canopy and decreased toward lower levels within the canopy. SOLWEIG-LEB generally reproduced these diurnal variations and vertical attenuation. Correlation coefficients (r) at individual heights ranged from 0.81 to 0.99, and RMSEs ranged from 18.32 to 44.38 W m^{-2}. When valid paired data from the three heights were pooled within each region (Table 4), the correlation coefficients were 0.98 and 0.96 in regions A and B, respectively, and the corresponding RMSEs were 21.92 and 31.38 W m^{-2}. Errors were relatively larger in the lower canopy than at the upper levels. In particular, at 1.1 m in region B, the correlation coefficient decreased to 0.81 and RMSE was 44.38 W m^{-2}. These results indicate that SOLWEIG-LEB reproduced the overall PAR attenuation pattern, although relatively large errors remained in the local radiative environment of the lower canopy. These errors may be influenced by simplified model assumptions regarding actual canopy geometry, the spatial LAD distribution, and the leaf projection function (G_{proj}), as well as uncertainty in the leaf distribution around the measurement locations.

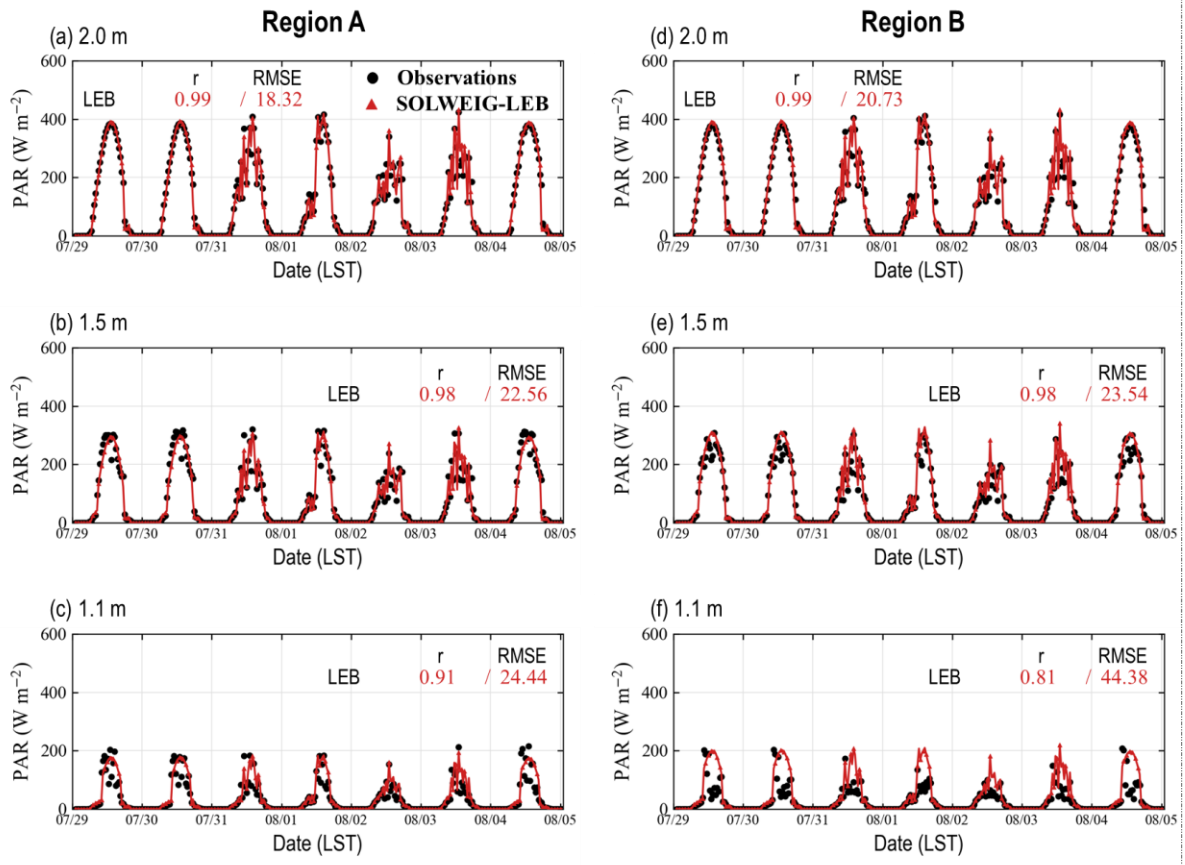

Figure 8. Comparison of observed photosynthetically active radiation (PAR) and SOLWEIG-LEB results at different heights in vegetated regions A and B in Angers, France. The left column shows PAR comparisons at heights of (a) 2.0 m, (b) 1.5 m, and (c) 1.1 m in region A, and the right column shows those at (d) 2.0 m, (e) 1.5 m, and (f) 1.1 m in region B. Black circles indicate observations, and red triangles indicate SOLWEIG-LEB.

Figure 9 compares observed daily transpiration and SOLWEIG-LEB results for two trees in region A (G and E) and one tree in region B (H) in Angers. SOLWEIG-LEB generally reproduced the overall magnitude and day-to-day variations in transpiration observed for the three trees. The correlation coefficients (r) for trees G, E, and H were 0.93, 0.94, and 0.71, respectively, and the corresponding RMSEs were 0.85, 0.28, and 0.26 L tree^{-1} (Table 4). In particular, simulated transpiration was relatively close to the observations for trees E and H, whereas transpiration for tree G was consistently overestimated despite reproducing its day-to-day variation.

Herpin et al. (2024) reported regional mean leaf areas rather than individual-tree leaf areas, with values of 2.59 ± 0.28 and 2.02 ± 0.31 m^2 tree^{-1} for regions A and B, respectively (mean ± standard error). Accordingly, transpiration was calculated using the mean leaf area for each region, and the corresponding range of simulated transpiration based on the standard error of leaf area is also shown in Fig. 9. Overestimation persisted for tree G even when this range was considered, whereas observed and simulated transpiration were generally similar for trees E and H. These results indicate that SOLWEIG-LEB can generally reproduce the

magnitude and day-to-day variations of tree transpiration, while highlighting the importance of leaf-area representativeness when evaluating transpiration for individual trees.

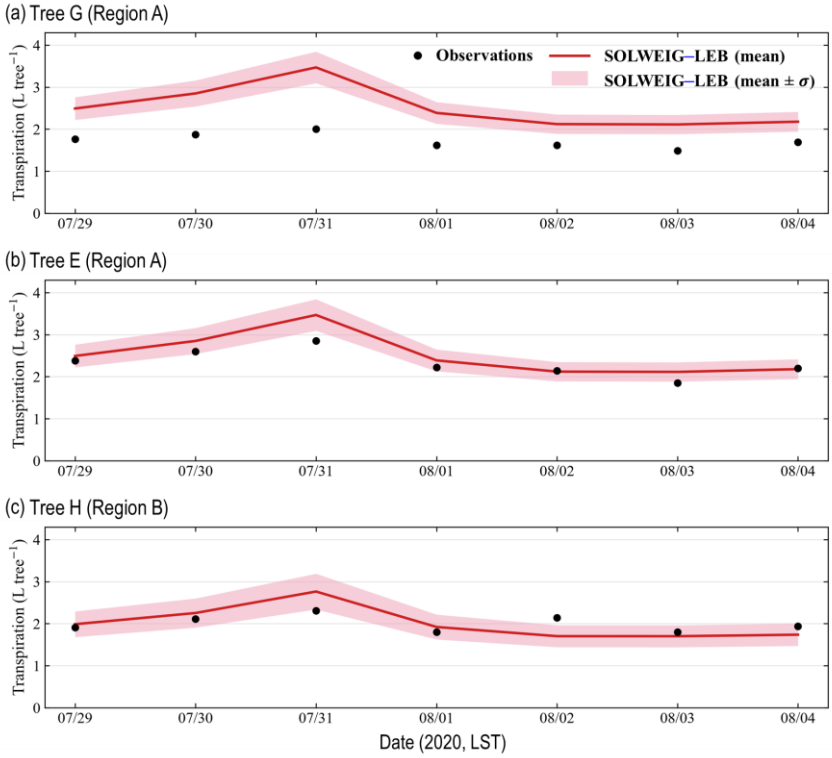

Figure 9. Comparison of observed daily transpiration per tree and SOLWEIG-LEB results in vegetated regions A and B in Angers, France. Panels show transpiration for (a) tree G in region A, (b) tree E in region A, and (c) tree H in region B. Black circles indicate observations, and red solid lines indicate SOLWEIG-LEB results calculated using the regional mean leaf area per tree. Pink shading indicates the transpiration range obtained by applying the mean leaf area ±1 standard error.

Table 3. Region-specific statistics for daytime and nighttime leaf temperature and MRT in Angers. Leaf-temperature statistics were calculated by pooling paired data from the three observation points within each region. RMSE and MBE are expressed in °C.

Region	Metric	Leaf temperature (°C)		MRT (°C)	
		Legacy	SOLWEIG-LEB	Legacy	SOLWEIG-LEB
A	N	1003	1003	336	336
	r	0.96	0.97	0.96	0.96
	RMSE	1.82	1.72	2.53	2.32
	NRMSE	0.06	0.06	0.07	0.07
	MBE	0.36	0.09	0.77	0.39
B	N	1008	1008	336	336
	r	0.95	0.97	0.97	0.97
	RMSE	2.19	1.61	2.30	2.20
	NRMSE	0.07	0.05	0.06	0.06
	MBE	0.22	-0.04	-0.04	-0.64
C	N	–	–	336	336
	r	–	–	0.99	0.99
	RMSE	–	–	2.40	2.40
	NRMSE	–	–	0.04	0.04
	MBE	–	–	0.29	0.27

Table 4. Evaluation statistics for PAR and daily transpiration in Angers, France. Valid paired PAR data from three heights (1.1, 1.5, and 2.0 m) were pooled within regions A and B, while transpiration was evaluated separately for trees G and E in region A and tree H in region B. N denotes the number of valid observation–model pairs. RMSE and MBE are expressed in W m^{-2} for PAR and L $tree^{-1}$ for transpiration.

Metric	PAR (W m^{-2})		Transpiration (L $tree^{-1}$)		
	A	B	G	E	H
N	1007	1008	7	7	7
r	0.98	0.96	0.93	0.94	0.71
RMSE	21.92	31.38	0.85	0.28	0.26
NRMSE	0.05	0.08	1.68	0.28	0.52
MBE	0.83	8.08	0.79	0.20	0.01

Additional leaf-temperature evaluation was conducted using observations from Mainz, Germany, under four contrasting sky conditions (Appendix B). SOLWEIG-LEB reproduced the observed diurnal variations, with RMSEs ranging from 1.17 to 1.45 °C (Fig. B3 and Table B1). Compared with Legacy SOLWEIG ($T_{veg} = T_{air}$), RMSE decreased from 1.56 to 1.23 °C under clear-sky conditions and from 2.08 to 1.45 °C under slightly cloudy conditions. However, the improvement was limited under mostly cloudy conditions, while Legacy SOLWEIG yielded a lower RMSE under fully cloudy conditions. These results demonstrate that explicitly calculating leaf temperature using the LEB module can improve leaf-temperature predictions, particularly under conditions with stronger solar forcing.

Page 46:

The finding in Section 4.3 that EXP1 reproduced nearly all of the MRT RMSE reduction achieved by EXP2 (accounting for over 97 % of the total error reduction) demonstrates that, under the evaluated conditions in Göteborg, improvements in pedestrian-level MRT relative to Legacy SOLWEIG were overwhelmingly governed by LAD-based canopy radiative treatment. …… The Angers evaluation complements the Göteborg analysis by assessing the vertical distribution of PAR, leaf temperature, and tree transpiration. PAR observations provide an additional assessment of canopy shortwave attenuation, whereas leaf-temperature and transpiration observations evaluate the thermal response and tree-level water loss calculated by the leaf energy balance module. Together, these comparisons extend the observational evaluation of SOLWEIG-LEB beyond its contribution to pedestrian-level MRT accuracy.

5.2. Added capabilities and intended scope of SOLWEIG-LEB

SOLWEIG-LEB integrates LAD-based canopy attenuation with a voxel-scale leaf energy balance, extending the vegetation representation in SOLWEIG to include intra-canopy thermal states and energy partitioning. This development is consistent with recent efforts to represent the thermal states of individual urban surfaces more explicitly within the SOLWEIG framework. Wallenberg et al. (2026) introduced a method for calculating wall surface temperature based on local radiative balance and material properties, and the present study advances this trajectory by establishing an explicit representation of vegetation thermal states within SOLWEIG. SOLWEIG-LEB is a diagnostic model that calculates the canopy radiative environment and leaf energy balance under prescribed meteorological forcing. Unlike prognostic microclimate models such as ENVI-met or PALM-4U, which resolve atmospheric flow and turbulent transport of heat and moisture interactively through time, SOLWEIG-LEB focuses on path-dependent radiative transfer associated with three-dimensional canopy structure and steady-state thermal response of vegetation. Although the leaf energy balance module provided only a small additional improvement in pedestrian-level MRT accuracy under the evaluated Göteborg conditions, its principal added value lies in diagnosing leaf temperature and sensible and latent heat exchange within the canopy. Specifically, the full LEB configuration enables analysis of the relationship between spatial variations in canopy radiation, leaf–air temperature differences, and the balance among net radiation, sensible heat exchange, and latent heat flux. Furthermore, the Angers evaluation

demonstrates how voxel-scale latent heat fluxes can be converted into tree-level transpiration estimates using representative leaf area. This modular model structure allows the level of detail to be flexibly selected according to the intended application and available computational resources. ……

Page 54–59:

Appendix B. Additional leaf-temperature evaluation using observations from Mainz

B1. Observational data and numerical experiments

Additional leaf-temperature evaluation used the dataset reported by Simon et al. (2018) for the Landesmuseum courtyard in Mainz, Germany. The site consists of an approximately 43 × 48 m courtyard surrounded by buildings 10–16 m in height, and the observed tree was Platanus × acerifolia (Fig. B1). Leaf surface temperature was measured using an Arduino-based infrared thermometer equipped with a Melexis MLX90614ESF-DCI sensor, with a 5° field of view and an assumed leaf emissivity of 0.97 (Simon et al., 2018). The reported factory-calibrated accuracy was ±0.5 °C over 0–60 °C, and measurements taken several times per second were averaged over 5 min intervals. The sensor was mounted on a branch approximately 5 m above ground and directed towards a dense leaf cluster approximately 3 m below it. The reported observation area was approximately 540 cm^2 and remained shaded for most of the day. The model calculated the mean and minimum–maximum range of leaf temperatures for vegetation voxels within the estimated observation area at approximately 2 m above ground. The horizontal resolution was 1 m, and LAD was prescribed as 0.6 m^2 m^{-3}. Although the approximate observation area was reported, its precise location and spatial arrangement within the canopy could not be reconstructed from the available information; the voxel selection therefore represents an estimated sampling area rather than an exact match to the observed leaves.

The evaluation periods were 2–3, 6–7, 11–13, and 16–17 August 2015, corresponding to clear-sky, slightly cloudy, mostly cloudy, and fully cloudy conditions, respectively (Fig. B2). Observed leaf temperatures and ENVI-met results were extracted from the figures in Simon et al. (2018). In the original study, air temperature and relative humidity were measured within the courtyard, whereas wind speed and shortwave radiation were obtained from a meteorological station approximately 3 km southwest of the site. Because the site-specific air-temperature and humidity time series were unavailable for the present evaluation, off-site meteorological records were used as forcing for SOLWEIG-LEB. Wind speed was set to 1.3 m s^{-1}, CO_2 concentration to 420 ppm, and soil-water conditions to REW = 1. These off-site meteorological inputs may not fully represent the air conditions surrounding the observed leaves. Downward longwave radiation was estimated from air temperature, humidity, and a solar-radiation-based clearness index. Before sunrise, the index from the same morning was used, whereas the final daytime value was used after sunset. Leaf temperatures were compared with Legacy SOLWEIG ($T_{veg} = T_{air}$), SOLWEIG-LEB, and the ENVI-met results reported by Simon et al. (2018).

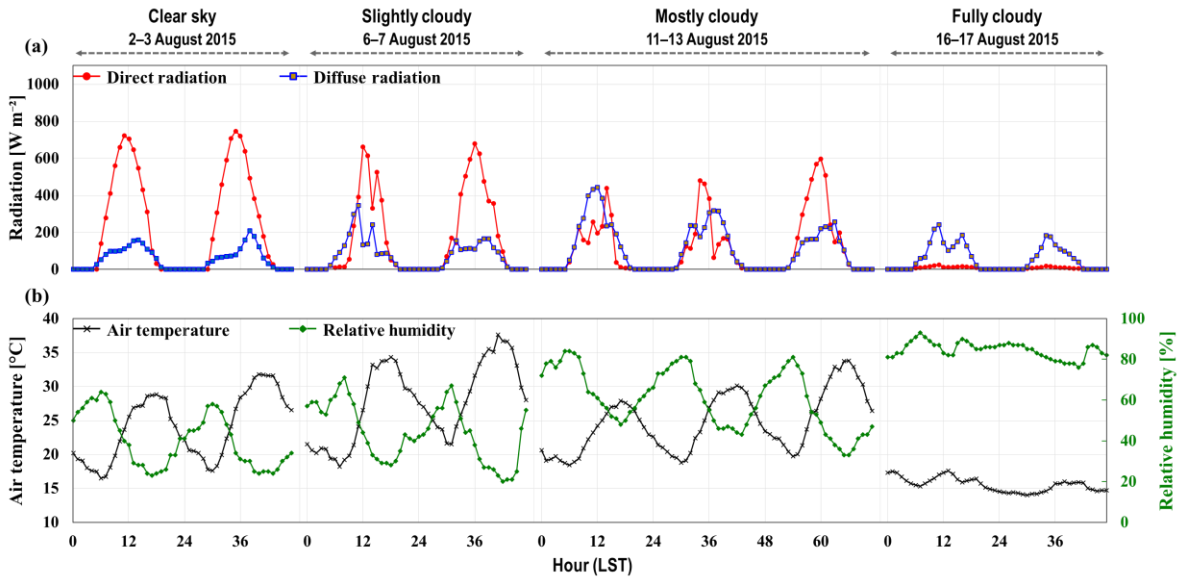

Figure B2. Meteorological forcing used for the Mainz simulations during four evaluation periods: clear-sky (2–3 August 2015), slightly cloudy (6–7 August 2015), mostly cloudy (11–13 August 2015), and fully cloudy (16–17 August 2015). (a) Direct and diffuse shortwave radiation and (b) air temperature and relative humidity.

B2. Leaf-temperature evaluation results

Figure B3 compares observed leaf temperatures with SOLWEIG-LEB, Legacy SOLWEIG, and the ENVI-met results reported by Simon et al. (2018) under four sky conditions. Overall, SOLWEIG-LEB reproduced the diurnal variations in leaf temperature under the different sky conditions and yielded smaller errors than the conventional $T_{veg} = T_{air}$ assumption, particularly under clear-sky and slightly cloudy conditions.

Under clear-sky conditions, pronounced diurnal variations were observed, with daytime leaf-temperature increases under strong solar radiation and cooling at night (Fig. B3a). SOLWEIG-LEB generally reproduced these variations, with an RMSE of 1.23 °C, lower than those of Legacy SOLWEIG (1.56 °C) and ENVI-met (1.42 °C; Table B1). By explicitly calculating the difference between leaf and air temperatures, SOLWEIG-LEB produced results closer to the observed leaf-temperature variations than the conventional isothermal assumption.

Under slightly cloudy conditions, SOLWEIG-LEB also reproduced the increases and decreases in leaf temperature associated with changes in solar radiation reasonably well (Fig. B3b). In particular, it calculated relatively lower leaf temperatures from around noon until after sunset, producing closer agreement with the observed diurnal variation. Accordingly, RMSE decreased from 2.08 °C in Legacy SOLWEIG to 1.45 °C in SOLWEIG-LEB. However, both models overestimated leaf temperature during some nighttime periods. This is interpreted as reflecting uncertainty in the background meteorological forcing associated with the use of air temperature from a station approximately 3 km away.

Under mostly cloudy conditions, SOLWEIG-LEB reproduced the temporal variation in observed leaf temperature well, with a correlation coefficient of 0.99 (Fig. B3c). However, RMSEs were similar for SOLWEIG-LEB and Legacy SOLWEIG, at 1.20 and 1.19 °C, respectively, indicating no clear reduction in error relative to the conventional air-temperature assumption.

Under fully cloudy conditions, weaker solar heating substantially reduced the diurnal range of leaf temperature (Fig. B3d). SOLWEIG-LEB reproduced these variations, with an RMSE of 1.17 °C, lower than the ENVI-met value of 1.39 °C. However, Legacy SOLWEIG yielded a smaller RMSE of 0.92 °C. At night, the absence of shortwave energy input allows leaf temperature to fall below air temperature depending on the balance among net longwave radiation loss, sensible heat supplied by the air, and latent heat exchange. During this period, observed leaf temperatures were relatively close to the input air temperature, whereas SOLWEIG-LEB exhibited a mean bias of −1.02 °C over the entire evaluation period, calculating slightly lower leaf temperatures than Legacy SOLWEIG, which had a mean bias of −0.83 °C. These differences may be associated with leaf radiative cooling and uncertainties in the background meteorological and downward longwave radiation inputs.

Overall, SOLWEIG-LEB yielded lower RMSEs than ENVI-met under all four sky conditions and reproduced the diurnal variation in leaf temperature more accurately than Legacy SOLWEIG, particularly under clear-sky and slightly cloudy conditions. These improvements were limited under cloudy conditions, indicating that leaf-temperature performance may depend on radiative conditions and the accuracy of the background meteorological forcing.

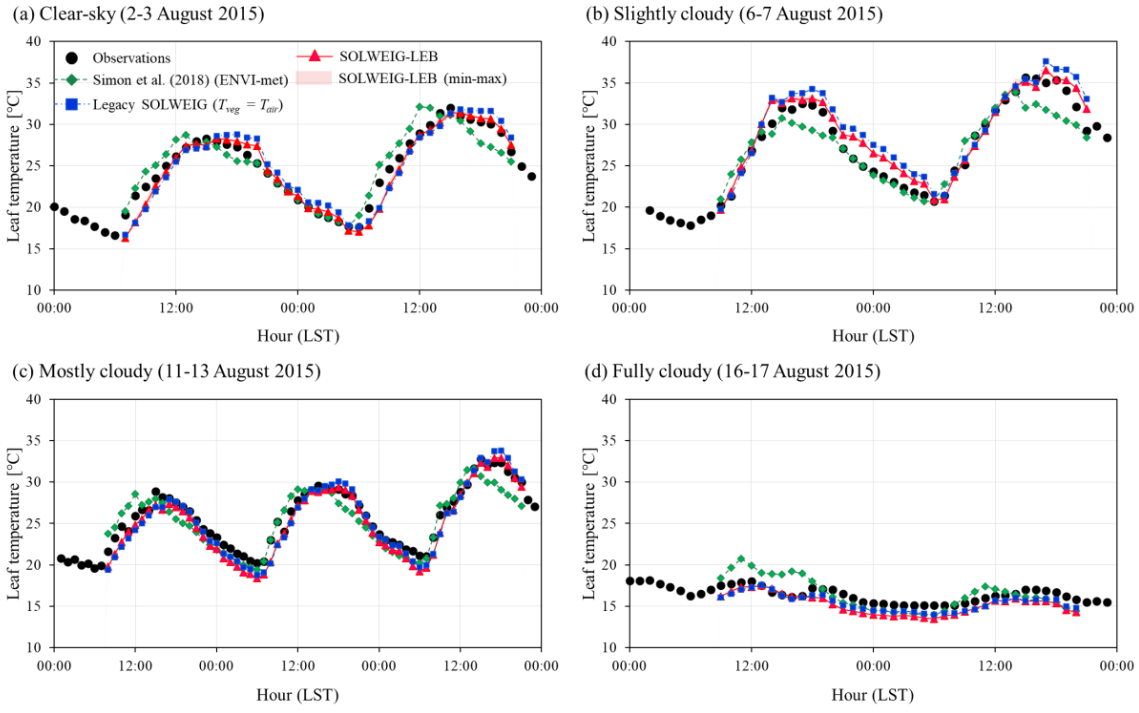

Figure B3. Comparison of observed and simulated leaf temperatures at the Mainz site under (a) clear-sky, (b) slightly cloudy, (c) mostly cloudy, and (d) fully cloudy conditions. Black

circles indicate observations, green lines represent the ENVI-met results reported by Simon et al. (2018), blue squares indicate Legacy SOLWEIG ($T_{veg} = T_{air}$), and red triangles indicate SOLWEIG-LEB. Red shading represents the minimum–maximum range of simulated leaf temperatures within the estimated observation area.

Table B1. Statistical evaluation of leaf temperature at the Mainz site.

Period (2015)	Metric	Simon et al. (2018) (ENVI-met)	Legacy SOLWEIG	SOLWEIG-LEB
Clear-sky	N	39	39	39
08/02–03	r	0.94	0.94	0.97
	RMSE [°C]	1.42	1.56	1.23
	NRMSE	0.10	0.11	0.09
	MBE [°C]	0.18	-0.09	-0.34
Slightly cloudy	N	37	37	37
08/06–07	r	0.95	0.96	0.97
	RMSE [°C]	1.84	2.08	1.45
	NRMSE	0.12	0.13	0.09
	MBE [°C]	-0.72	1.47	0.91
Mostly cloudy	N	62	62	62
08/11–13	r	0.91	0.98	0.99
	RMSE [°C]	1.54	1.19	1.20
	NRMSE	0.12	0.09	0.10
	MBE [°C]	-0.55	-0.60	-0.89
Fully cloudy	N	36	36	36
08/16–17	r	0.77	0.91	0.89
	RMSE [°C]	1.39	0.92	1.17
	NRMSE	0.48	0.32	0.40
	MBE [°C]	0.21	-0.83	-1.02

Comment 2
The validation is too limited to support general conclusions. Leaf-temperature evaluation covers one tree during two short periods, while radiation evaluation covers two locations across four days. The uncertain leaf observation footprint and meteorological forcing from a station approximately 3 km away further weaken the comparison. Longer observations, broader conditions, and clearer documentation of the measurement setup are needed.

→ We appreciate the reviewer's constructive comment regarding the observational duration, meteorological forcing, and footprint uncertainties. To address the limited evaluation periods and observational conditions in the original manuscript, we conducted an additional evaluation using seven days of observations (29 July–4 August 2020) from the reduced-scale street-canyon experiment in Angers, France, as described in our response to Comment 1. The Angers experiment comprises two vegetated regions (A and B) with different LAI values and a non-vegetated region (C), with clearly documented leaf-temperature measurement locations and heights. Importantly, the Angers experiment provides a complementary evaluation that mitigates the observational limitations noted for Mainz: meteorological forcing was obtained on site, with air temperature, relative humidity, and radiation measured in region C and wind speed measured between regions B and C at 2 m above ground, and leaf temperatures were recorded using thermocouples attached directly to the undersides of leaves, thereby reducing ambiguity in the observation locations and reliance on off-site meteorological forcing. We also expanded the model evaluation across broader conditions by incorporating vertical PAR attenuation, tree-level transpiration, and MRT observations (Sections 3.1 and 4.1). In addition, we extended the Mainz leaf-temperature evaluation from two to four periods (2–3, 6–7, 11–13, and 16–17 August 2015), covering clear-sky, slightly cloudy, mostly cloudy, and fully cloudy conditions (Appendix B).

→ To clarify the measurement environment and model–observation comparison methods, we provided comprehensive descriptions of the observational instruments, measurement locations and heights, meteorological forcing data, and evaluation period for Angers in Section 3.1 and Figs. 2–3 of the revised manuscript. In Appendix B1, we also specified the type, field of view, and installation height of the infrared leaf-temperature sensor in Mainz, the observed leaf cluster, and the comparison method based on the estimated model observation area.

→ For Mainz, Simon et al. (2018) reported a leaf-temperature observation area of approximately 540 cm^2, but did not provide sufficient information to reconstruct the precise three-dimensional location and spatial arrangement of the observed leaf cluster. Therefore, the estimated observation area used in the model may not coincide with the actual sensor footprint. Furthermore, although air temperature and relative humidity were measured within the courtyard in the original study, the corresponding time series were unavailable for the present evaluation, so data from a meteorological station approximately 3 km away were used as model inputs. We clarified these uncertainties associated with the spatial representativeness of the observation area and meteorological forcing in Appendix B1 and Section 5.3, and discussed the limitations of generalizing the results across different tree species, seasons, and observational conditions in Section 5.3.

Now, it reads:

Page 16–17:

3.1. Vegetation and radiative-environment evaluation dataset in Angers

Observations from a reduced-scale street-canyon experiment in Angers, France (Herpin et al., 2024), were used to evaluate within-canopy radiation attenuation, leaf temperature, transpiration, and MRT. The experimental site consisted of a north–south-oriented street canyon and building models on both sides, with a building height, building width, and canyon width of 2 m each (Fig. 2). Ornamental apple trees were present in regions A and B, whereas region C contained no trees (Fig. 2a). Following pruning, the canopy-top height was 1.70 m in both vegetated regions, and the canopy-base heights were 0.60 and 0.69 m in regions A and B, respectively. The corresponding LAI values were 2.49 and 1.91 m^2 m^{-2}. LAD was assumed to be vertically uniform within the canopy (Figs. 2b and c).

MRT was estimated from globe temperatures measured at 0.4 m above ground in the centre of regions A, B, and C. Leaf temperatures were measured at western, central, and eastern positions within the canopies of regions A and B at 1.5 m above ground (Fig. 2d). PAR was measured within the canopy at heights of 1.1 and 1.5 m and above the canopy at 2.0 m (Fig. 2d). Leaf temperatures were measured using thermocouples attached to the undersides of leaves, and PAR was measured using Solems PAR/LE sensors. MRT was derived by applying a convective correction to temperatures measured using Pt100 sensors installed inside black globes with a diameter of 15 cm (Herpin et al., 2024).

Meteorological forcing consisted of air temperature, relative humidity, downward shortwave and longwave radiation, and wind speed. Radiation, air temperature, and relative humidity were observed in the non-vegetated region C, whereas wind speed was measured between regions B and C at 2 m above ground (Figs. 2e and f). Air temperature and relative humidity were measured using Vaisala HMP sensors, wind speed using an LCJ CV7 ultrasonic anemometer, and radiation using a Kipp & Zonen CNR radiometer (Herpin et al., 2024). Air temperature and wind speed observations at 2 m above ground were used, and direct and diffuse shortwave radiation were partitioned internally from the input global shortwave radiation. Air temperature, relative humidity, and wind speed were applied uniformly across the domain. The evaluation covered seven days from 29 July to 4 August 2020, with simulations performed at 30 min intervals (Fig. 3). Time is expressed in local standard time (LST, UTC+1).

Page 48:

5.3. Limitations and future development

The present evaluation has several limitations that should be addressed in future investigations. First, the supplementary Mainz evaluation covered a single tree species under four contrasting sky conditions (Appendix B). In Mainz, the precise location and spatial arrangement of the observed foliage within the reported sensor footprint were unavailable, so the estimated lower-canopy sampling area may not coincide with the infrared sensor's observation footprint. Air temperature and relative humidity obtained from a meteorological

station approximately 3 km away may also differ from the conditions surrounding the observed leaves. These uncertainties may affect the agreement between simulated and observed leaf temperatures.

Second, the Göteborg evaluation covered only two distinct spatial locations across four days, restricted to foliated conditions in late spring and summer. These initial results are therefore insufficient to comprehensively establish model performance across different tree species, seasons, complex canopy geometries, and highly variable meteorological conditions. Further evaluation is warranted for leafless deciduous trees, evergreen trees, sparse canopies, and crown-edge conditions.

Third, the numerical representation of canopy structure involves several simplifying assumptions. The current version assumes a spherical leaf angle distribution with a leaf projection function of G_{proj} = 0.5, and LAD is assumed to be uniformly distributed within the canopy envelope when high-resolution observed LAD profiles are unavailable. However, actual LAD, leaf inclination and azimuth distributions, foliage clumping, and branch structure may vary with species, growth stage, canopy height, and position within the canopy. Consequently, G_{proj} may also vary with solar position and leaf orientation distribution. The sensitivity analysis in Appendix C showed that variations in G_{proj} associated with different leaf orientation distributions can affect direct shortwave transmissivity and local MRT. Therefore, future developments should incorporate measured three-dimensional canopy geometry, spatially resolved LAD and leaf orientation distributions, and foliage clumping and branch structures, using data derived from terrestrial laser scanning, hemispherical photography, or within-canopy radiation measurements.

Fourth, the leaf energy balance module solves a steady-state balance and consequently neglects internal leaf heat storage and thermal inertia effects. ……

Page 54:

Appendix B. Additional leaf-temperature evaluation using observations from Mainz

B1. Observational data and numerical experiments

Additional leaf-temperature evaluation used the dataset reported by Simon et al. (2018) for the Landesmuseum courtyard in Mainz, Germany. The site consists of an approximately 43 × 48 m courtyard surrounded by buildings 10–16 m in height, and the observed tree was Platanus × acerifolia (Fig. B1). Leaf surface temperature was measured using an Arduino-based infrared thermometer equipped with a Melexis MLX90614ESF-DCI sensor, with a 5° field of view and an assumed leaf emissivity of 0.97 (Simon et al., 2018). The reported factory-calibrated accuracy was ±0.5 °C over 0–60 °C, and measurements taken several times per second were averaged over 5 min intervals. The sensor was mounted on a branch approximately 5 m above ground and directed towards a dense leaf cluster approximately 3 m below it. The reported observation area was approximately 540 cm^2 and remained shaded for most of the day. The model calculated the mean and minimum–maximum range of leaf temperatures for vegetation voxels within the estimated observation area at approximately 2 m above ground. The horizontal resolution was 1 m, and LAD was prescribed as 0.6 m^2 m^{-3}. Although the approximate observation area was reported, its precise location and spatial arrangement within the canopy could not be reconstructed from the available information;

the voxel selection therefore represents an estimated sampling area rather than an exact match to the observed leaves.

The evaluation periods were 2–3, 6–7, 11–13, and 16–17 August 2015, corresponding to clear-sky, slightly cloudy, mostly cloudy, and fully cloudy conditions, respectively (Fig. B2). Observed leaf temperatures and ENVI-met results were extracted from the figures in Simon et al. (2018). In the original study, air temperature and relative humidity were measured within the courtyard, whereas wind speed and shortwave radiation were obtained from a meteorological station approximately 3 km southwest of the site. Because the site-specific air-temperature and humidity time series were unavailable for the present evaluation, off-site meteorological records were used as forcing for SOLWEIG-LEB. Wind speed was set to 1.3 m s^{-1}, CO_2 concentration to 420 ppm, and soil-water conditions to REW = 1. These off-site meteorological inputs may not fully represent the air conditions surrounding the observed leaves. Downward longwave radiation was estimated from air temperature, humidity, and a solar-radiation-based clearness index. Before sunrise, the index from the same morning was used, whereas the final daytime value was used after sunset. Leaf temperatures were compared with Legacy SOLWEIG ($T_{veg} = T_{air}$), SOLWEIG-LEB, and the ENVI-met results reported by Simon et al. (2018).

Comment 3

The essential leaf-temperature baseline is missing. The authors should compare their calculated leaf temperature directly with the original assumption using identical observation times. Comparison with published ENVI-met results alone does not establish improvement over the original SOLWEIG treatment. Figure 6 shows discontinuous SOLWEIG-LEB leaf-temperature results, whereas Figure 7 presents full-day radiation simulations.

Please explain the gaps in each model series, identify the hours included in Table 3, and distinguish periods with an active leaf energy balance calculation from those using the air-temperature assumption. The current presentation makes the scope of the leaf-temperature evaluation difficult to assess.

→ We appreciate the reviewer's important comment regarding the baseline comparison and the clarity of the evaluation timeline. We added the isothermal vegetation assumption ($T_{veg} = T_{air}$) used in the original SOLWEIG as a baseline and directly compared it with the leaf temperatures calculated by SOLWEIG-LEB at identical observation times. The results are presented in Fig. 6 for Angers and Fig. B3 and Table B1 for Mainz.

→ In the original manuscript, gaps appeared in the leaf-temperature time series because the LEB calculation was formulated as a daytime-only routine and was not performed at night. In the revised manuscript, we have extended the leaf energy balance calculation to nighttime conditions, where leaf temperature is governed by the steady-state equilibrium between net longwave radiative cooling and aerodynamic sensible and latent heat transfers in the absence of shortwave radiation. Thus, leaf temperature in the revised SOLWEIG-LEB is calculated using the LEB module during both daytime and nighttime, whereas the original isothermal vegetation assumption is applied only in Legacy SOLWEIG.

→ We also clarified the evaluation periods and sample sizes to remove ambiguity regarding the scope of the statistical tables. Tables 3 and B1 include valid paired samples from both daytime and nighttime. Table 3 presents the numbers of valid observation–model pairs for regions A and B in Angers (1,003 and 1,008, respectively), pooled from the three observation points in each region at 30-min intervals over the 7-day period. Table B1 reports the numbers of common valid samples for the four evaluation periods in Mainz (39, 37, 62, and 36, respectively). The Mainz ENVI-met results were obtained from the time series reported by Simon et al. (2018), and the statistics were calculated using only identical time steps for which observations and results from all three models were available.

Now, it reads:

Page 17:

The Legacy reference configuration retained the common non-vegetation settings while applying a fixed canopy transmissivity and prescribing vegetation temperature as $T_{veg} = T_{air}$. Representative transmissivity along a vertical path was calculated using the Beer–Lambert law as follows:

$$\tau = \exp(-G_{proj}\, LAI). \quad (25)$$

Applying $G_{\text{proj}} = 0.5$ to the LAI values of regions A and B yielded vertical-path transmissivities of approximately 29 % and 38 %, respectively. Separate Legacy simulations were conducted using fixed transmissivities of 30 % and 40 %, which approximated these values. Results for regions A were compared with the 30 % simulation, whereas results for regions B and C were compared with the 40 % simulation. SOLWEIG-LEB used a spherical leaf angle distribution ($G_{\text{proj}} = 0.5$) and LAD-based shortwave attenuation, and calculated the leaf energy balance using the CANOAK photosynthesis–stomatal coupling. The characteristic leaf dimension was set to 0.05 m, and the background CO_2 concentration was set to 420 ppm. The horizontal grid spacing was 0.2 m, and the vertical spacing of vegetation voxels was 0.1 m. The leaf energy balance was calculated during both daytime and nighttime, with leaf temperature and vegetation longwave emission updated iteratively. Solid-surface temperatures were calculated using daytime and nighttime empirical equations calibrated against site observations. Wall albedo and emissivity were set to 0.40 and 0.87, respectively, and the corresponding ground values were 0.25 and 0.94. PAR was calculated by applying the model's PAR energy fraction f_{PAR} (= 0.45) to the downward shortwave radiation ($K_{\downarrow}$) at the receiver (Baldocchi, 1994; Harley and Baldocchi, 1995).

Page 26:

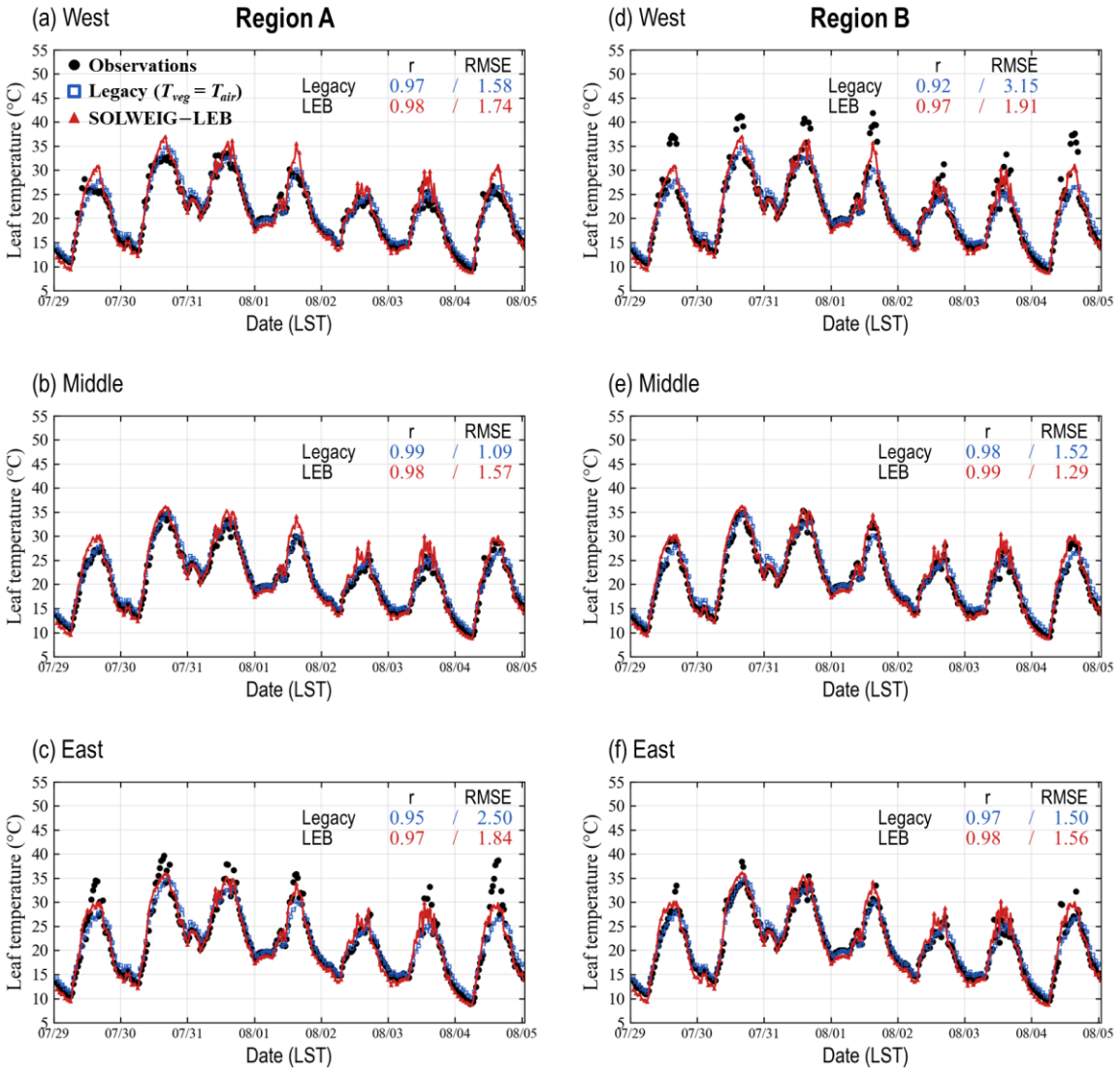

Figure 6. Comparison of observed and simulated leaf temperatures at 1.5 m above ground in vegetated regions A and B in Angers, France. The left column shows comparisons at the (a) western, (b) central, and (c) eastern observation points in region A, and the right column shows those at the (d) western, (e) central, and (f) eastern observation points in region B. Black circles indicate observations, blue open squares indicate Legacy SOLWEIG ($T_{veg} = T_{air}$), and red triangles indicate SOLWEIG-LEB.

Page 28–29:

Table 3. Region-specific statistics for daytime and nighttime leaf temperature and MRT in Angers. Leaf-temperature statistics were calculated by pooling paired data from the three observation points within each region. RMSE and MBE are expressed in °C.

Region	Metric	Leaf temperature (°C)		MRT (°C)	
		Legacy	SOLWEIG-LEB	Legacy	SOLWEIG-LEB
A	N	1003	1003	336	336
	r	0.96	0.97	0.96	0.96
	RMSE	1.82	1.72	2.53	2.32
	NRMSE	0.06	0.06	0.07	0.07
	MBE	0.36	0.09	0.77	0.39
B	N	1008	1008	336	336
	r	0.95	0.97	0.97	0.97
	RMSE	2.19	1.61	2.30	2.20
	NRMSE	0.07	0.05	0.06	0.06
	MBE	0.22	-0.04	-0.04	-0.64
C	N	–	–	336	336
	r	–	–	0.99	0.99
	RMSE	–	–	2.40	2.40
	NRMSE	–	–	0.04	0.04
	MBE	–	–	0.29	0.27

Page 54:

The evaluation periods were 2–3, 6–7, 11–13, and 16–17 August 2015, corresponding to clear-sky, slightly cloudy, mostly cloudy, and fully cloudy conditions, respectively (Fig. B2). Observed leaf temperatures and ENVI-met results were extracted from the figures in Simon et al. (2018). In the original study, air temperature and relative humidity were measured within the courtyard, whereas wind speed and shortwave radiation were obtained from a meteorological station approximately 3 km southwest of the site. Because the site-specific air-temperature and humidity time series were unavailable for the present evaluation, off-site meteorological records were used as forcing for SOLWEIG-LEB. Wind speed was set to 1.3 m s^{-1}, CO_2 concentration to 420 ppm, and soil-water conditions to REW = 1. These off-site meteorological inputs may not fully represent the air conditions surrounding the observed leaves. Downward longwave radiation was estimated from air temperature, humidity, and a solar-radiation-based clearness index. Before sunrise, the index from the same morning was used, whereas the final daytime value was used after sunset. Leaf temperatures were compared with Legacy SOLWEIG ($T_{veg} = T_{air}$), SOLWEIG-LEB, and the ENVI-met results reported by Simon et al. (2018).

Page 58:

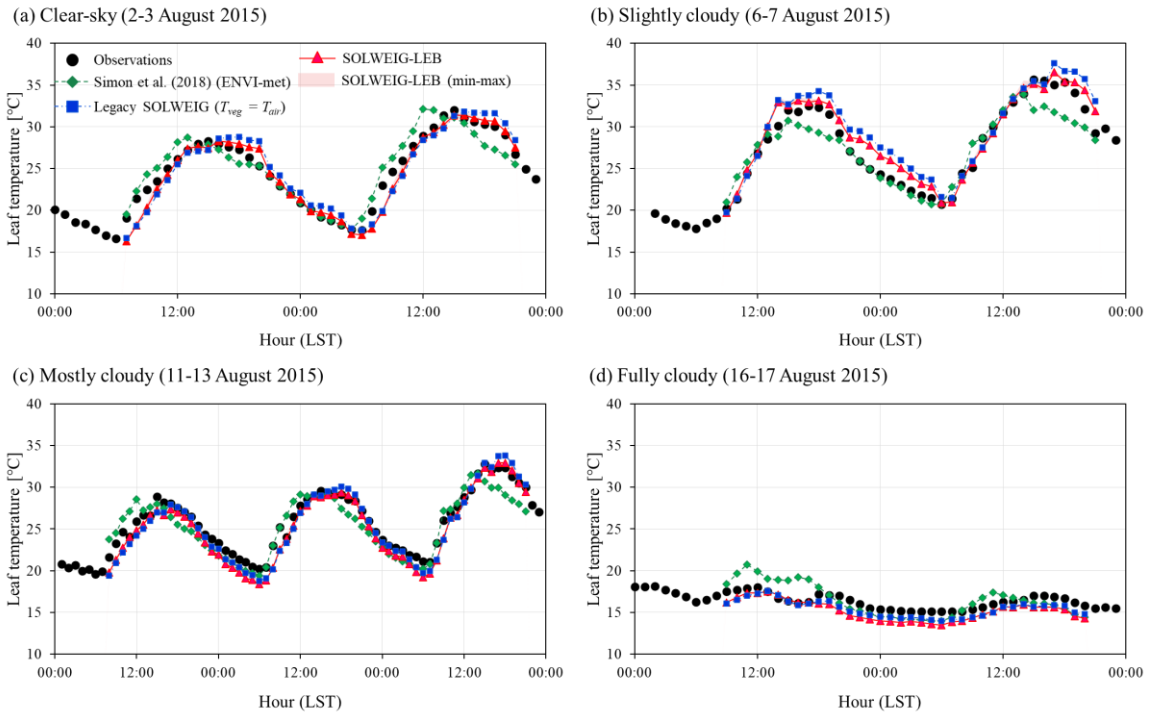

Figure B3. Comparison of observed and simulated leaf temperatures at the Mainz site under (a) clear-sky, (b) slightly cloudy, (c) mostly cloudy, and (d) fully cloudy conditions. Black circles indicate observations, green lines represent the ENVI-met results reported by Simon et al. (2018), blue squares indicate Legacy SOLWEIG ($T_{veg} = T_{air}$), and red triangles indicate SOLWEIG-LEB. Red shading represents the minimum–maximum range of simulated leaf temperatures within the estimated observation area.

Page 59:

Table B1. Statistical evaluation of leaf temperature at the Mainz site.

Period (2015)	Metric	Simon et al. (2018) (ENVI-met)	Legacy SOLWEIG	SOLWEIG-LEB
Clear-sky 08/02–03	N	39	39	39
	r	0.94	0.94	0.97
	RMSE [°C]	1.42	1.56	1.23
	NRMSE	0.10	0.11	0.09
	MBE [°C]	0.18	-0.09	-0.34
Slightly cloudy	N	37	37	37

08/06–07	r	0.95	0.96	0.97
	RMSE [°C]	1.84	2.08	1.45
	NRMSE	0.12	0.13	0.09
	MBE [°C]	-0.72	1.47	0.91
Mostly cloudy	N	62	62	62
08/11–13	r	0.91	0.98	0.99
	RMSE [°C]	1.54	1.19	1.20
	NRMSE	0.12	0.09	0.10
	MBE [°C]	-0.55	-0.60	-0.89
Fully cloudy	N	36	36	36
08/16–17	r	0.77	0.91	0.89
	RMSE [°C]	1.39	0.92	1.17
	NRMSE	0.48	0.32	0.40
	MBE [°C]	0.21	-0.83	-1.02

Comment 4

The canopy assumptions require sensitivity analysis.

The model introduces path-dependent optical depth but assumes a spherical leaf-angle distribution with G=0.5. LAD is also prescribed using simplified canopy representations rather than detailed measurements of the evaluated trees. These assumptions do not invalidate the approach, but they directly influence the transmissivity responsible for most of the reported improvement. Please quantify sensitivity to LAD, leaf projection function, and canopy geometry.

Because the strongest improvements occur near canopy boundaries, sensitivity to grid resolution and observation-point positioning is particularly important.

The study should also examine whether its advantage persists across reasonable choices of the legacy model's fixed transmissivity. This would help distinguish the benefit of spatially varying attenuation from the effect of comparing against one prescribed baseline value.

→ We sincerely thank the reviewer for these constructive suggestions regarding the sensitivity analyses. Detailed measurements of LAD and leaf orientation were unavailable for the trees evaluated in this study. Based on published values for the two species, we prescribed a reference LAD of 0.6 m^2 m^{-3} at both sites. At OP1, the reported direct shortwave transmissivity of 1.7 % corresponds to an effective LAI of approximately 8.1 along the radiation path, assuming a spherical leaf angle distribution (G = 0.5). We agree that these assumptions may not fully represent the structure of the observed canopies and therefore introduce uncertainty. As the reviewer noted, canopy geometry, grid resolution, and observation-point location, as well as LAD and G, can affect estimates of the pedestrian-level radiative environment and MRT. We agree that their influence warrants a sensitivity analysis.

→ Accordingly, we conducted additional sensitivity experiments using observations from four days in Göteborg: one at OP1 and three at OP2. We examined LAD, the leaf projection function G for different leaf orientations, horizontal grid resolution, and the fixed canopy transmissivity used in Legacy SOLWEIG. To assess uncertainties associated with canopy geometry and observation-point positioning, we reconstructed the same canopy data at different horizontal grid resolutions (0.5, 1.0, 2.0, and 4.0 m) and examined variations in MRT at sampling locations around the original observation points. Except for the changes specified in each sensitivity experiment, all other model inputs were held constant.

→ These experiments allowed us to quantify changes in MRT associated with the main canopy assumptions and input settings. We have also discussed the associated uncertainties and model limitations in the revised manuscript. The sensitivity results are summarised in Appendix C and in the discussion, conclusions, and limitations sections. The results of each experiment are presented below.

1. Sensitivity to LAD

→ We conducted sensitivity experiments using LAD values of 0.2, 0.4, 0.6, 0.8, and 1.0 m^2 m^{-3}. Differences in MRT among the LAD values occurred mainly between 06:00 and 11:00 LST at OP1 and during the daytime except between 08:00 and 10:00 LST at OP2 (Fig. R1). At both sites, lower LAD resulted in higher MRT when the canopy attenuated solar radiation. Overestimation of MRT relative to observations was particularly pronounced at an LAD of 0.2 m^2 m^{-3}.

→ To examine these differences, we compared the spatial distributions around OP1 at 10:00 LST on 23 May and OP2 at 14:00 LST on 7 July (Figs. R2 and R3). At OP1, increasing LAD from 0.2 to 0.6 m^2 m^{-3} reduced direct shortwave transmissivity from 0.357 to 0.045, downward shortwave radiation from 330.45 to 139.99 W m^{-2}, and MRT from 38.21 to 26.64 °C. Increasing LAD to 1.0 m^2 m^{-3} reduced MRT to 24.88 °C, a further decrease of 1.76 °C.

→ At OP2, increasing LAD from 0.2 to 0.6 m^2 m^{-3} also reduced direct shortwave transmissivity from 0.151 to 0.003 and downward shortwave radiation from 197.55 to 103.42 W m^{-2}, while MRT decreased from 29.34 to 23.90 °C. At an LAD of 1.0 m^2 m^{-3}, MRT was 23.45 °C, a further decrease of 0.44 °C. At both representative times, direct shortwave transmissivity was already 0.05 or less at LAD values of 0.6 m^2 m^{-3} and above. Further increases in LAD therefore produced smaller reductions in shortwave radiation and MRT. The effect of LAD thus varied with the radiative path through the canopy and the time of day. Sensitivity to further increases in LAD was low when direct solar radiation was already strongly attenuated.

→ Across the 41 observation–model pairs pooled over the full observation period, MRT RMSE was 8.01, 5.05, 4.40, 4.31, and 4.36 °C at LAD values of 0.2, 0.4, 0.6, 0.8, and 1.0 m^2 m^{-3}, respectively. MRT RMSE generally decreased with increasing LAD, but the RMSEs for LAD values of 0.6–1.0 m^2 m^{-3} differed by less than 0.1 °C. These results show that the prescribed LAD can affect canopy attenuation of solar radiation and the accuracy of MRT estimates, highlighting the importance of using an LAD value representative of the canopy under study.

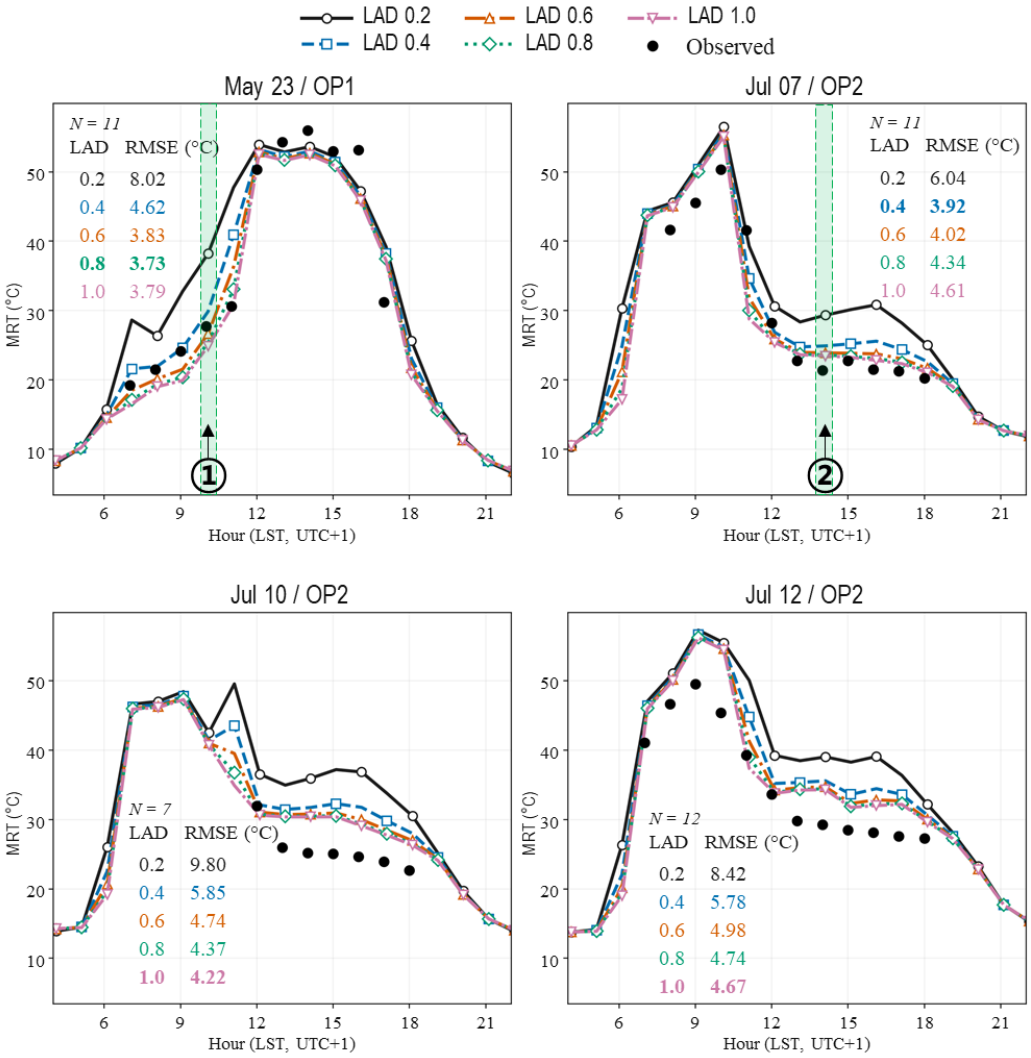

Figure R1. MRT time series for the LAD sensitivity experiments. Lines show results for LAD values of 0.2, 0.4, 0.6, 0.8, and 1.0 m^2 m^{-3}, and black circles indicate observations.

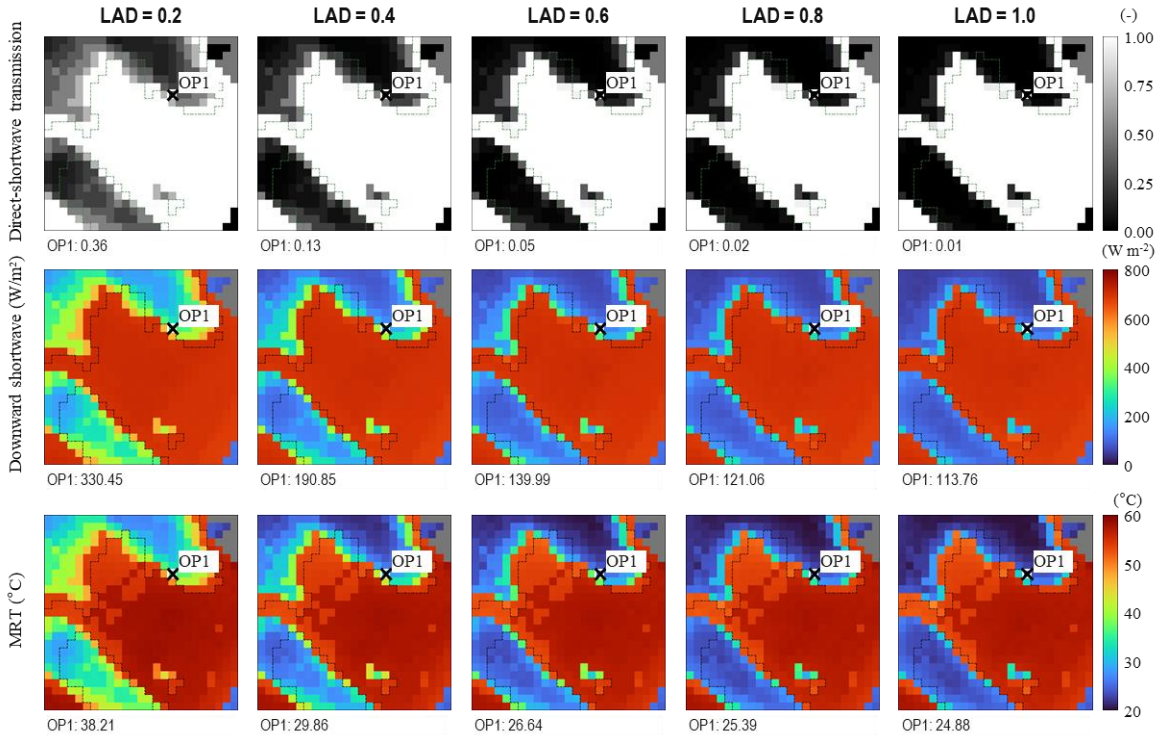

Figure R2. Spatial distributions for the LAD sensitivity experiments at 10:00 LST on 23 May. Columns show LAD values of 0.2, 0.4, 0.6, 0.8, and 1.0 m^2 m^{-3} from left to right. Rows show direct shortwave transmissivity, downward shortwave radiation, and MRT from top to bottom. The canopy boundaries and the sampling location at OP1 are shown. Numbers below the panels give the values at OP1.

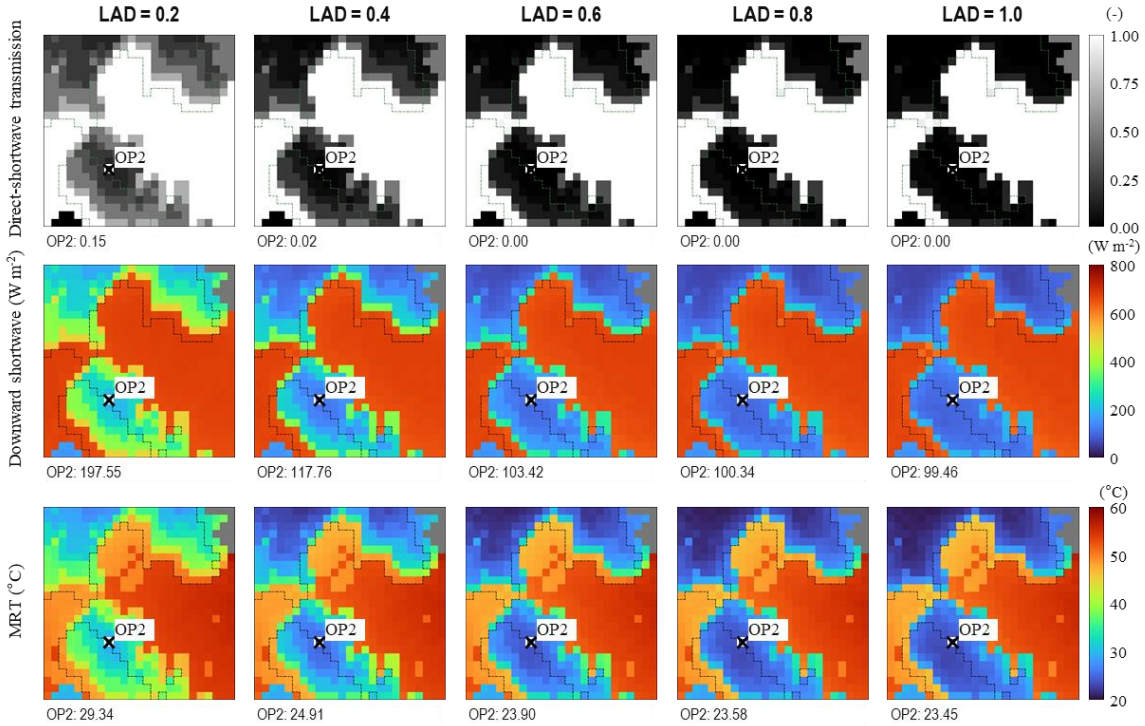

Figure R3. Spatial distributions around OP2 for the LAD sensitivity experiments at 14:00 LST on 7 July. Columns show LAD values of 0.2, 0.4, 0.6, 0.8, and 1.0 m^2 m^{-3} from left to right. Rows show direct shortwave transmissivity, downward shortwave radiation, and MRT from top to bottom. The canopy boundaries and the sampling location at OP2 are shown. Numbers below the panels give the values at OP2.

2. Sensitivity to the leaf projection function (G_{proj})

→ The leaf projection function G_{proj} is the mean projected leaf area per unit leaf area, with the projection taken onto a plane perpendicular to the direction of radiation. This dimensionless ratio depends on the orientation of the leaves relative to the sun, as determined by leaf inclination and azimuth, and affects the attenuation of direct solar radiation through the canopy (Fig. R4; Zeng et al., 2015). For a fixed leaf inclination angle γ and a uniform distribution of leaf azimuths within a voxel, G_{proj} can be expressed as a function of solar elevation angle η as follows:

$$G_{proj}(\eta, \gamma) = \frac{1}{2\pi}\int_0^{2\pi} |\sin\eta\cos\gamma + \cos\eta\sin\gamma\cos\varphi| d\varphi \quad \text{(R1)}$$

Here, η is the solar elevation angle, γ is the leaf inclination angle relative to the horizontal, and φ is the azimuthal difference between the leaf normal and the direction of the sun. The expression inside the absolute value is the dot product of the unit leaf normal and the unit vector pointing towards the sun. Averaging its absolute value over all azimuths gives G_{proj}.

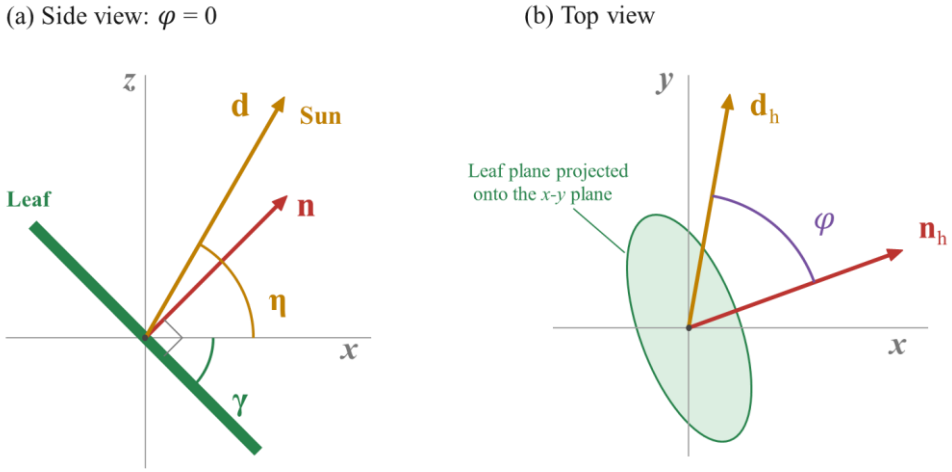

Figure R4. Definition of the angles used in the leaf projection function. (a) Side view for the case in which the leaf normal and the direction of the sun have the same azimuth ($\varphi = 0$) and (b) plan view. η is the solar elevation angle, γ is the leaf inclination angle relative to the horizontal, and φ is the azimuthal difference between the leaf normal and the direction of the sun. The vectors n and d are the unit leaf normal and the unit vector pointing towards the sun, respectively; n_h and d_h are their horizontal projections.

→ Leaf inclination angle distributions can vary with species, stage of growth, height within the canopy, and light exposure (Raabe et al., 2015). G_{proj} varies with these distributions. For example, as solar elevation increases, the projected area (G_{proj}) increases for horizontal leaves ($\gamma = 0°$) but decreases for vertical leaves ($\gamma = 90°$) with uniformly distributed azimuths. Rather than prescribing different constant values of G_{proj}, we therefore fixed the leaf orientation distribution in each experiment and allowed G_{proj} to vary with solar position according to Eq. (R1).

→ We considered four leaf orientation distributions: spherical ($G_{proj} = 0.5$), horizontal ($\gamma = 0°$), vertical ($\gamma = 90°$), and inclined at 45° ($\gamma = 45°$) (Fig. R5a–d). For the vertical and 45° cases, we assumed a uniform distribution of leaf azimuths within each voxel. Figure R5e illustrates how G_{proj} varies with solar elevation angle. LAD was fixed at 0.6 m^2 m^{-3}.

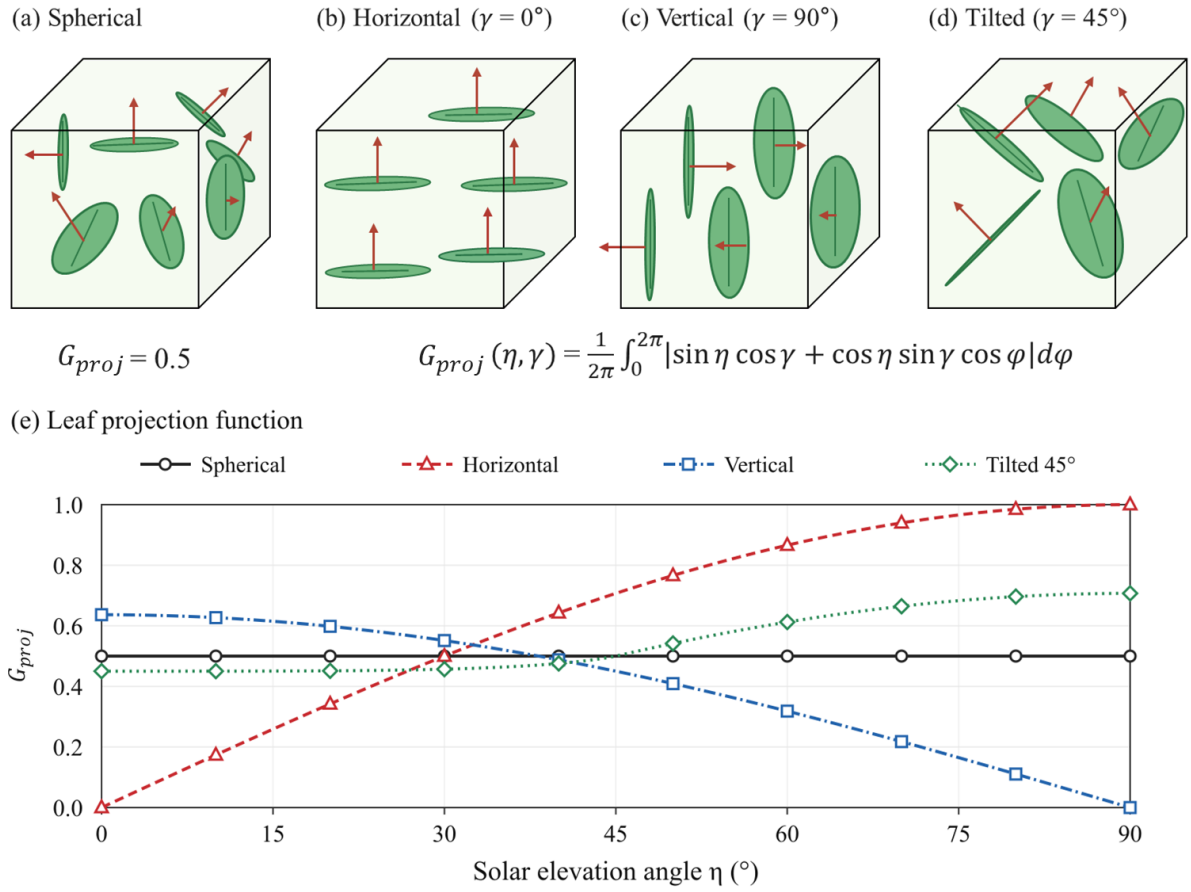

Figure R5. Schematic representation of leaf orientations and leaf normals within a voxel for (a) spherical, (b) horizontal, (c) vertical, and (*d*) 45° inclined leaves. (e) Leaf projection function G_{proj} as a function of solar elevation angle. Leaf azimuths were assumed to be uniformly distributed for the vertical and 45° cases.

→ The MRT time series showed similar diurnal variations for the four leaf orientations, although distinct differences occurred at certain times (Fig. R6). The differences were

relatively large around 07:00 and 11:00 LST on 23 May at OP1 and around 06:00 and 11:00 LST on 7 July at OP2. The maximum differences were 5.93 °C at OP1 (11:00 LST) and 8.35 °C at OP2 (06:00 LST).

→ To examine why these differences were concentrated at particular times, we compared the time series of direct shortwave transmissivity (Fig. R7). Transmissivity was close to 1 from approximately 12:00 to 16:00 LST at OP1 and close to 0 from approximately 12:00 to 18:00 LST on 7 July at OP2. Differences among the four experiments were small during these periods. In contrast, transmissivity varied with leaf orientation when the canopy partially attenuated direct solar radiation or when conditions shifted between sun and shade. Thus, the effect of *G* on MRT depended on exposure to direct solar radiation and shading.

→ To quantify these differences, we compared the spatial distributions around OP1 at 11:00 LST on 23 May (Fig. R8). At this time, *G* was 0.76 for horizontal leaves and 0.42 for vertical leaves, and the corresponding direct shortwave transmissivities were 0.18 and 0.39. Downward shortwave radiation was 244.18 W m^{-2} for horizontal leaves and 371.04 W m^{-2} for vertical leaves. The corresponding MRT values were 32.33 and 38.27 °C, a difference of approximately 5.9 °C. These results show that differences in projected leaf area associated with leaf orientation can affect direct shortwave attenuation and local MRT even with the same LAD and canopy geometry. Across all 41 observation–model pairs, MRT RMSE varied little among the four orientations (4.40–4.55 °C), and no single leaf orientation consistently improved performance.

→ This sensitivity analysis was limited to idealised leaf orientation distributions. In actual canopies, leaf inclination and azimuth distributions may vary with species and position within the canopy. Future studies should therefore incorporate measured three-dimensional distributions of leaf orientation and density and further evaluate their effects under a range of canopy conditions.

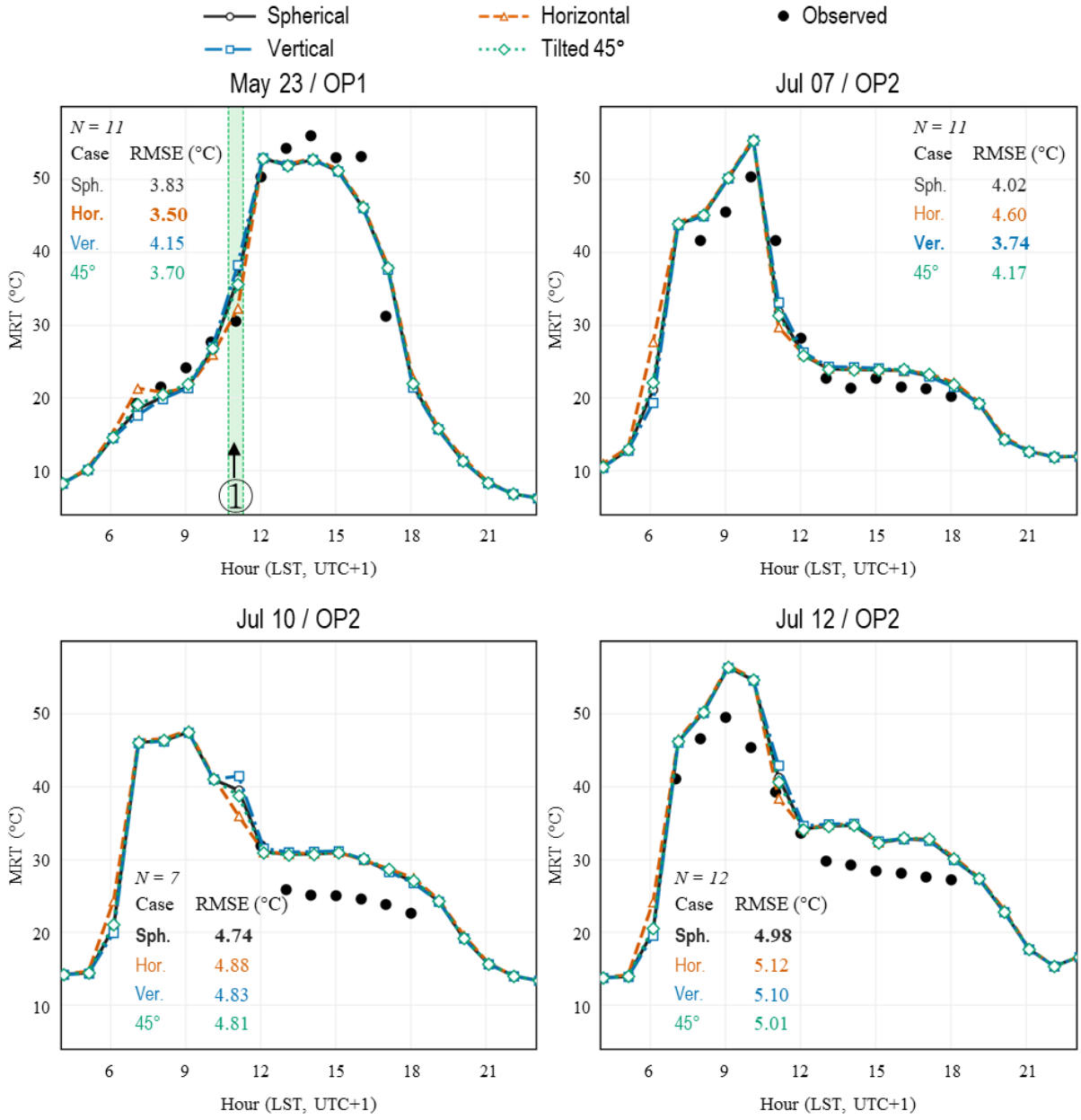

Figure R6. MRT time series for the four leaf orientations in the *G* sensitivity experiments. Lines show results for spherical, horizontal, vertical, and 45° inclined leaves, and black circles indicate observations.

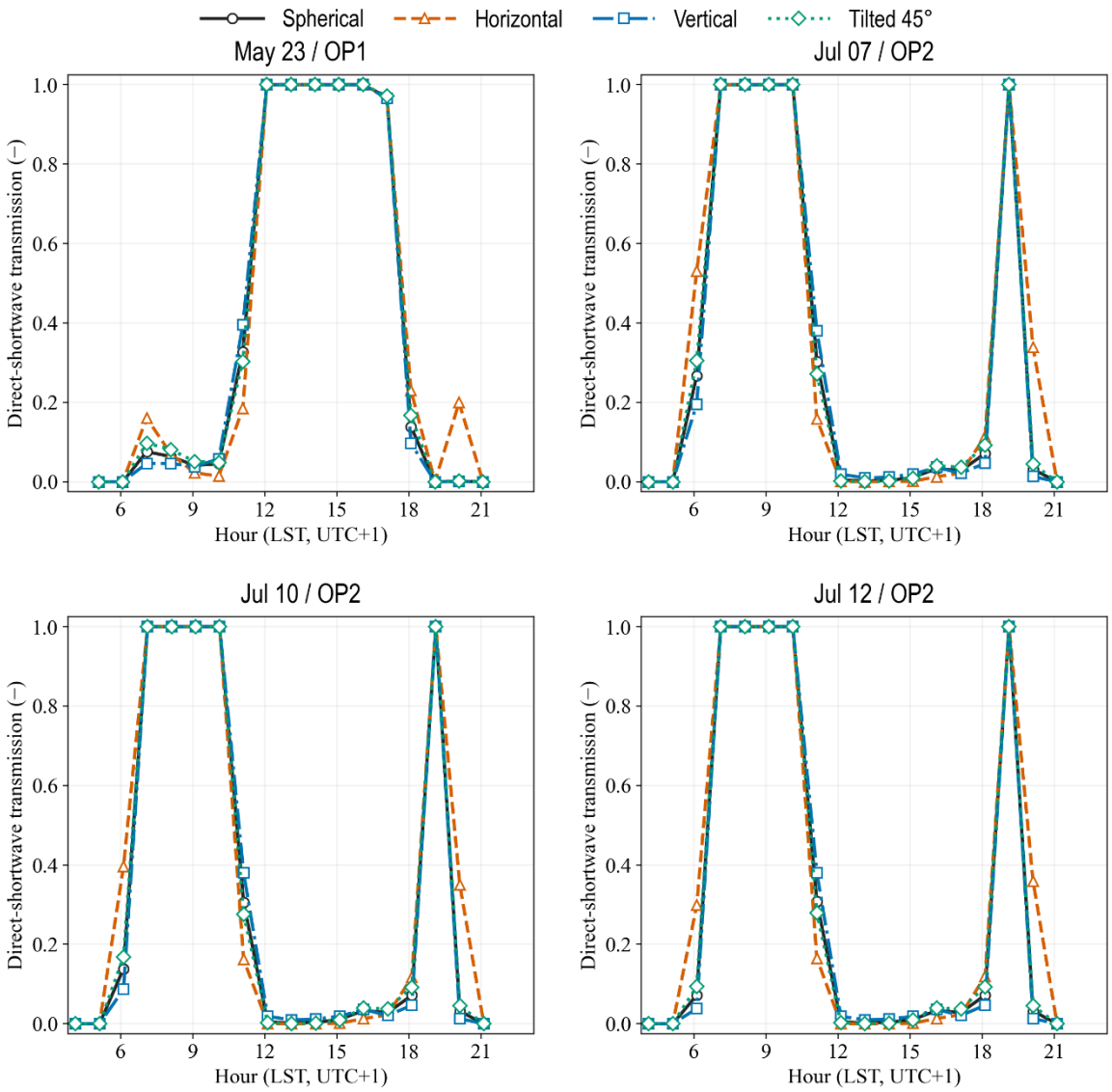

Figure R7. Time series of direct shortwave transmissivity at OP1 and OP2 for the four leaf orientations. Transmissivity accounts for both obstruction by buildings and attenuation by the canopy. A value of 1 indicates unattenuated direct solar radiation, and 0 indicates that direct solar radiation is blocked.

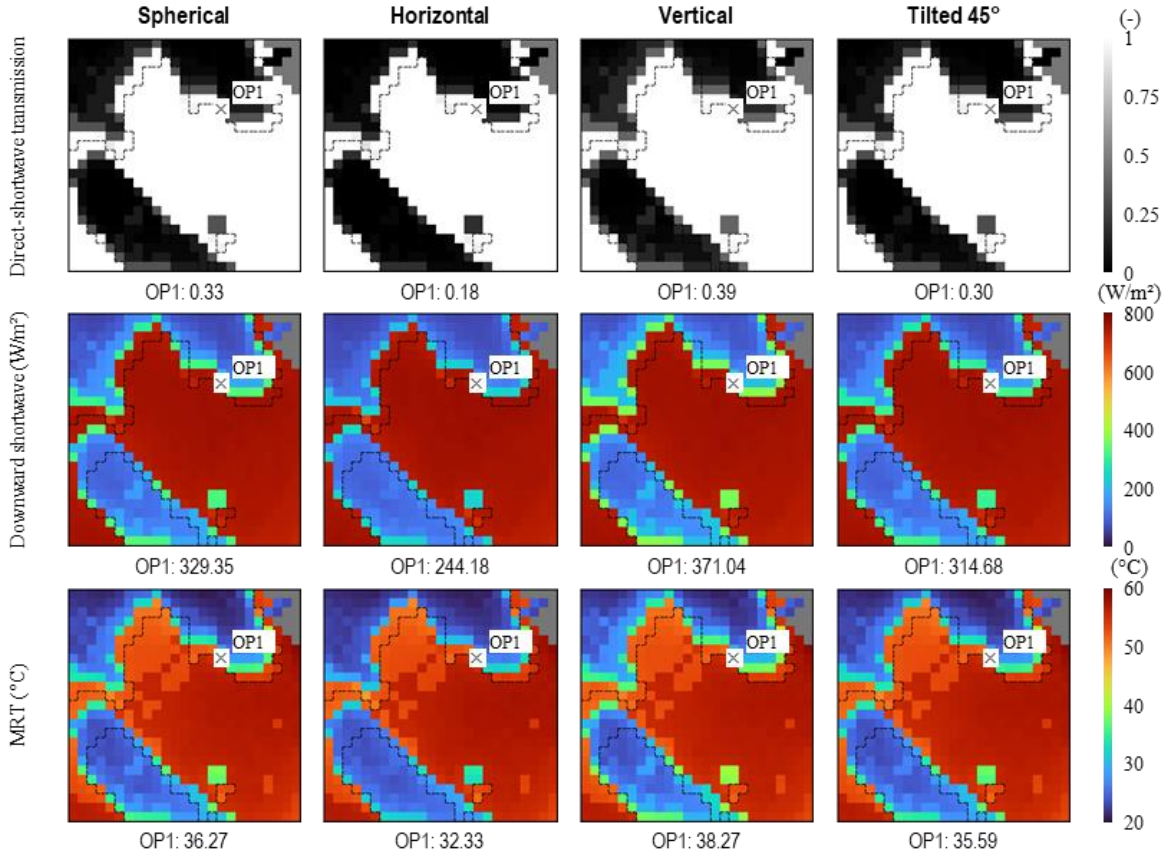

Figure R8. Spatial distributions around OP1 for the *G* sensitivity experiments at 11:00 LST on 23 May. Columns show results for spherical, horizontal, vertical, and 45° inclined leaves from left to right. Rows show direct shortwave transmissivity, downward shortwave radiation, and MRT from top to bottom. Dotted lines indicate the canopy boundaries represented on the grid. The sampling location at OP1 is shown, and numbers below the panels give the values at OP1.

3. Sensitivity to horizontal grid resolution and MRT sampling location

→ To assess how horizontal grid resolution and the resulting discretization of canopy boundary geometry affect canopy representation and MRT, we conducted experiments on a 260 m × 240 m subdomain at resolutions of 0.5, 1.0, 2.0, and 4.0 m (Fig. R9; Fig. C2 in Appendix C). To preserve the spatial geometry and structural characteristics of the canopy defined on the original 2.0 m grid as closely as possible, we divided each 2.0 m cell into 16 cells for the 0.5 m grid and four cells for the 1.0 m grid. Each new cell retained the original canopy-top and canopy-base heights and LAI. In contrast, the 4.0 m grid was constructed by combining four adjacent 2.0 m cells. If any of the original cells contained canopy, the corresponding 4.0 m cell was classified as vegetated and assigned the maximum canopy-top height and minimum canopy-base height among the canopies it contained. LAI was calculated as an area-weighted mean that included non-vegetated cells, thereby preserving total leaf area across resolutions.

→ Because grid-cell centres and canopy boundaries vary with resolution, we examined all non-building grid-cell centres within a 3 m radius of the original OP1 and OP2 coordinates on the 2.0 m grid (Fig. R9). At each resolution, we selected the sampling location that yielded the lowest MRT RMSE relative to observations. Figure R9 illustrates the canopy representation and candidate sampling locations at each resolution. The 0.5 and 1.0 m grids retained the canopy boundaries represented on the original 2.0 m grid, whereas aggregation to the 4.0 m grid altered the representation of canopy edges. The number and positions of candidate sampling cells within the 3 m search radius also varied with grid resolution.

→ Figure R10 compares the MRT time series at all candidate sampling locations for each resolution. The numbers of candidate cells were 112, 32, 9, and 1 per observation site for the 0.5, 1.0, 2.0, and 4.0 m grids, respectively. At the finer resolutions, MRT varied considerably among candidate locations during certain periods, particularly around transitions between direct solar exposure and canopy shading. In contrast, only one candidate cell was available within the search radius on the 4.0 m grid, so sampling-location variability could not be evaluated at this resolution.

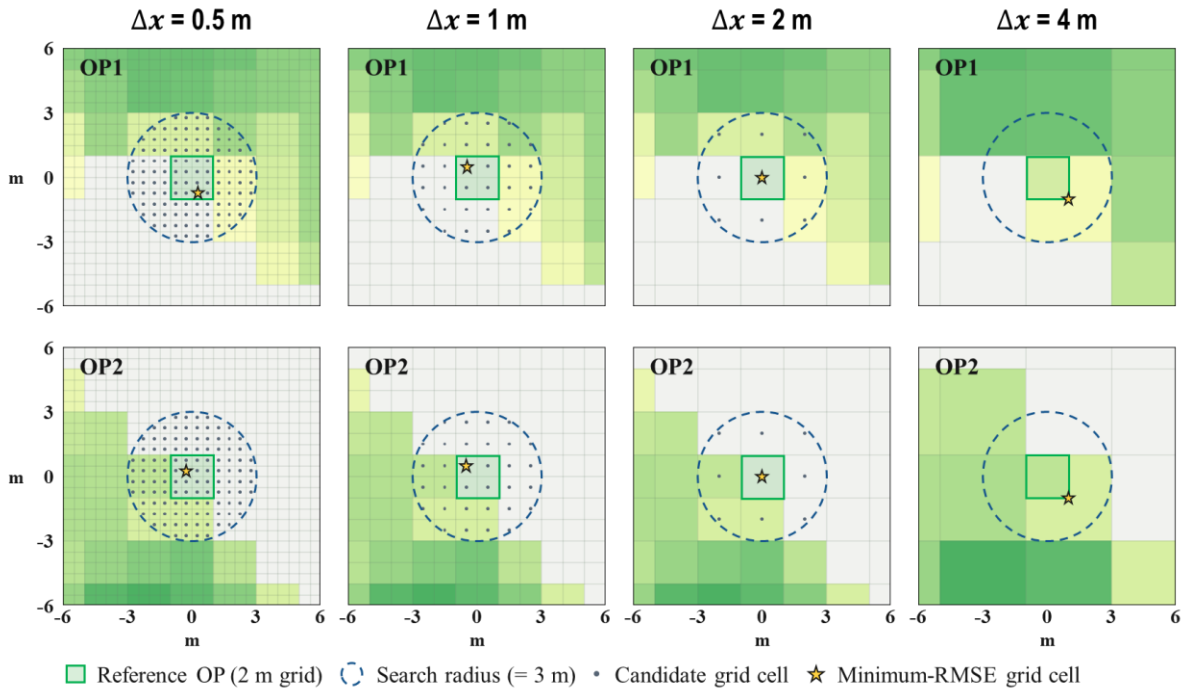

Figure R9. Canopy representation and candidate MRT sampling locations at OP1 (top) and OP2 (bottom) for horizontal grid resolutions of 0.5, 1.0, 2.0, and 4.0 m (left to right). Shades of green indicate canopy-top height, green squares mark the reference observation cells on the original 2.0 m grid, dashed circles show the 3 m search radius, dots indicate candidate sampling cells, and stars mark the minimum-RMSE cells.

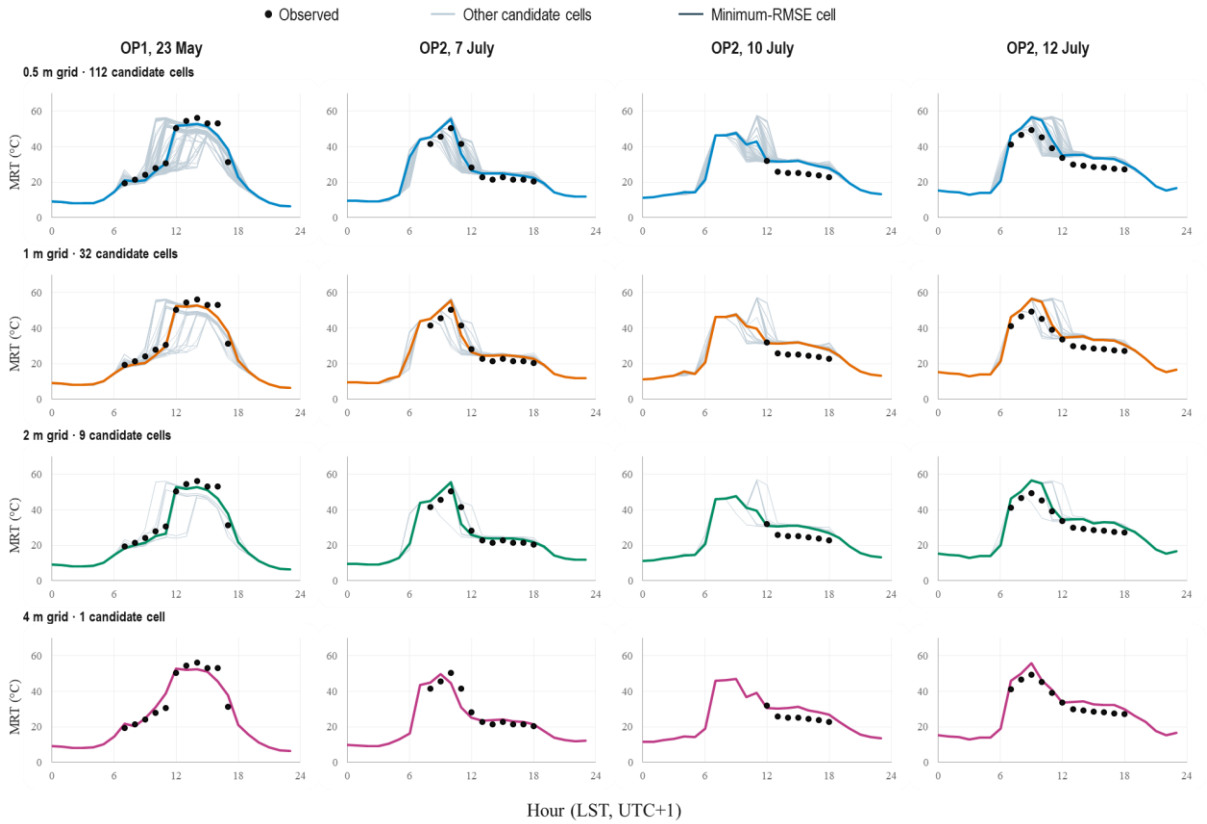

Figure R10. MRT time series at candidate sampling locations for each grid resolution (rows) and observation day (columns). Thin lines represent individual candidate cells, thick coloured lines indicate the minimum-RMSE cells, and black dots show observations.

→ Figure R11 (Fig. C3c in Appendix C) compares the MRT time series at the sampling locations with the lowest RMSE for each grid resolution, corresponding to the highlighted lines in Fig. R10. A finer grid did not consistently improve agreement with observations. At resolutions of 0.5, 1.0, 2.0, and 4.0 m, RMSEs at OP1 were 3.49, 3.62, 3.69, and 4.37 °C, respectively. The corresponding RMSEs pooled over the three observation days at OP2 were 4.82, 4.79, 4.61, and 4.23 °C. Thus, the 0.5 m grid yielded the smallest error at OP1, whereas the 4.0 m grid yielded the smallest error at OP2.

→ To examine these differences, we compared the spatial distributions of direct shortwave transmissivity, downward shortwave radiation, and MRT around OP2. At 11:00 LST on 7 July, direct shortwave transmissivity at the selected locations was 0.55 on both the 0.5 and 1.0 m grids but decreased to 0.30 on both the 2.0 and 4.0 m grids (Fig. R12). Downward shortwave radiation was 360.34, 360.06, 270.66, and 255.36 W m^{-2} at the four resolutions, respectively, and the corresponding MRT values were 36.06, 36.09, 31.84, and 30.79 °C. Observed MRT at this time was 41.61 °C. The results on the 0.5 and 1.0 m grids, where more direct solar radiation reached the selected locations, were closer to the observation.

→ In contrast, at 10:00 LST on 12 July, direct shortwave transmissivity at the selected locations was 1.00 on the 0.5, 1.0, and 2.0 m grids but decreased to 0.61 on the 4.0 m grid (Fig. R13). Downward shortwave radiation and MRT ranged from 579.30 to 579.98 W m^{-2} and from

54.61 to 54.81 °C, respectively, on the 0.5–2.0 m grids, compared with 388.37 W m^{-2} and 46.21 °C on the 4.0 m grid. Observed MRT was 45.36 °C, so the 4.0 m result was closer to the observation at this time.

→ These results show that solar radiation paths and local shading conditions can vary with grid resolution and observation-point location. No single resolution consistently performed best. However, the 0.5 and 1.0 m grids in this sensitivity experiment were obtained by subdividing the original 2.0 m canopy data and therefore did not resolve the actual fine-scale canopy geometry. On the 4.0 m grid, aggregation may also alter the canopy boundaries and height distribution. Further evaluation using measured high-resolution three-dimensional canopy data is therefore needed to assess how the accuracy of canopy geometry and the choice of grid resolution affect estimates of the radiative environment and MRT.

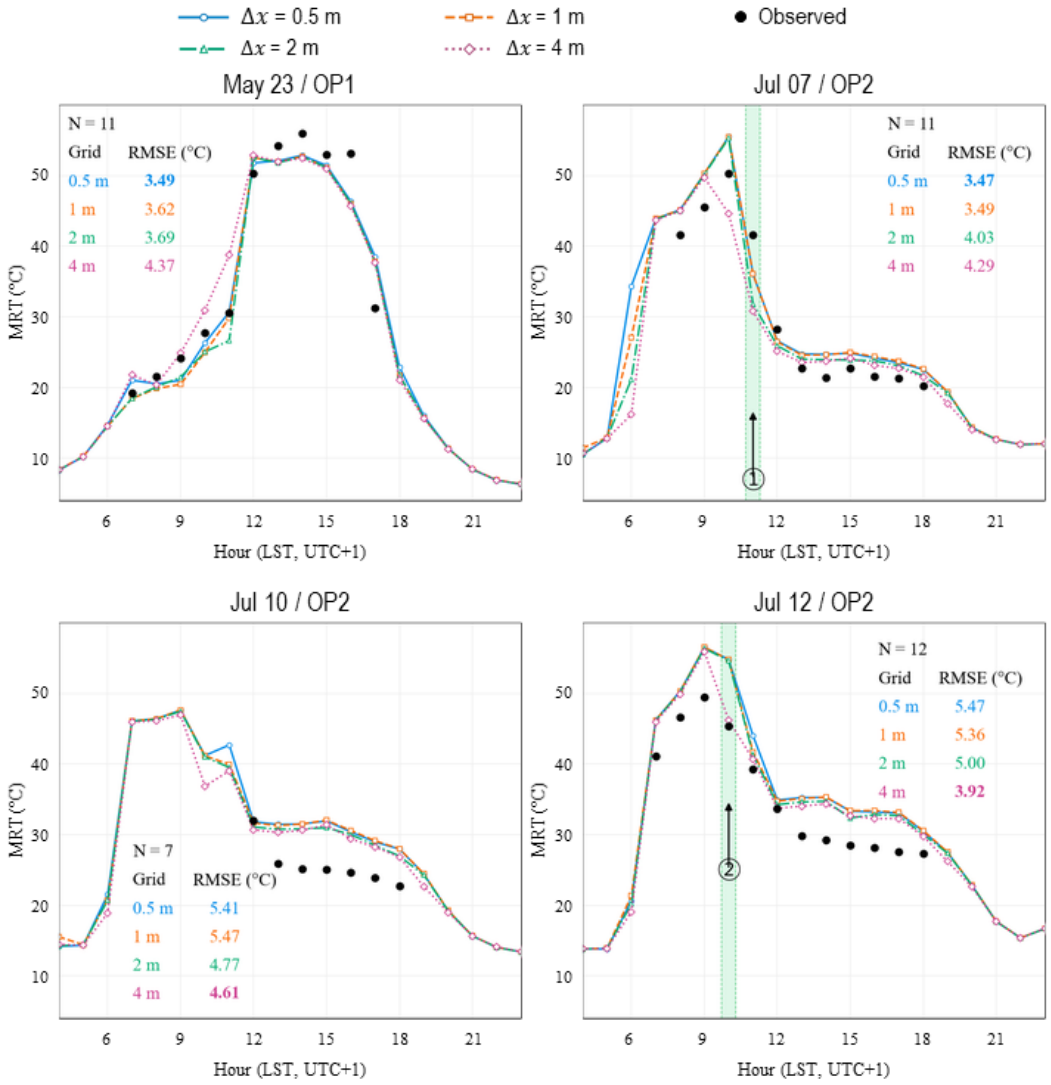

Figure R11. Observed MRT time series and corresponding simulations at the sampling locations selected for each horizontal grid resolution. The upper panels show OP1 on 23 May and OP2 on 7 July, and the lower panels show OP2 on 10 and 12 July. Lines show results for the 0.5, 1.0, 2.0, and 4.0 m grids, and black circles indicate observations.

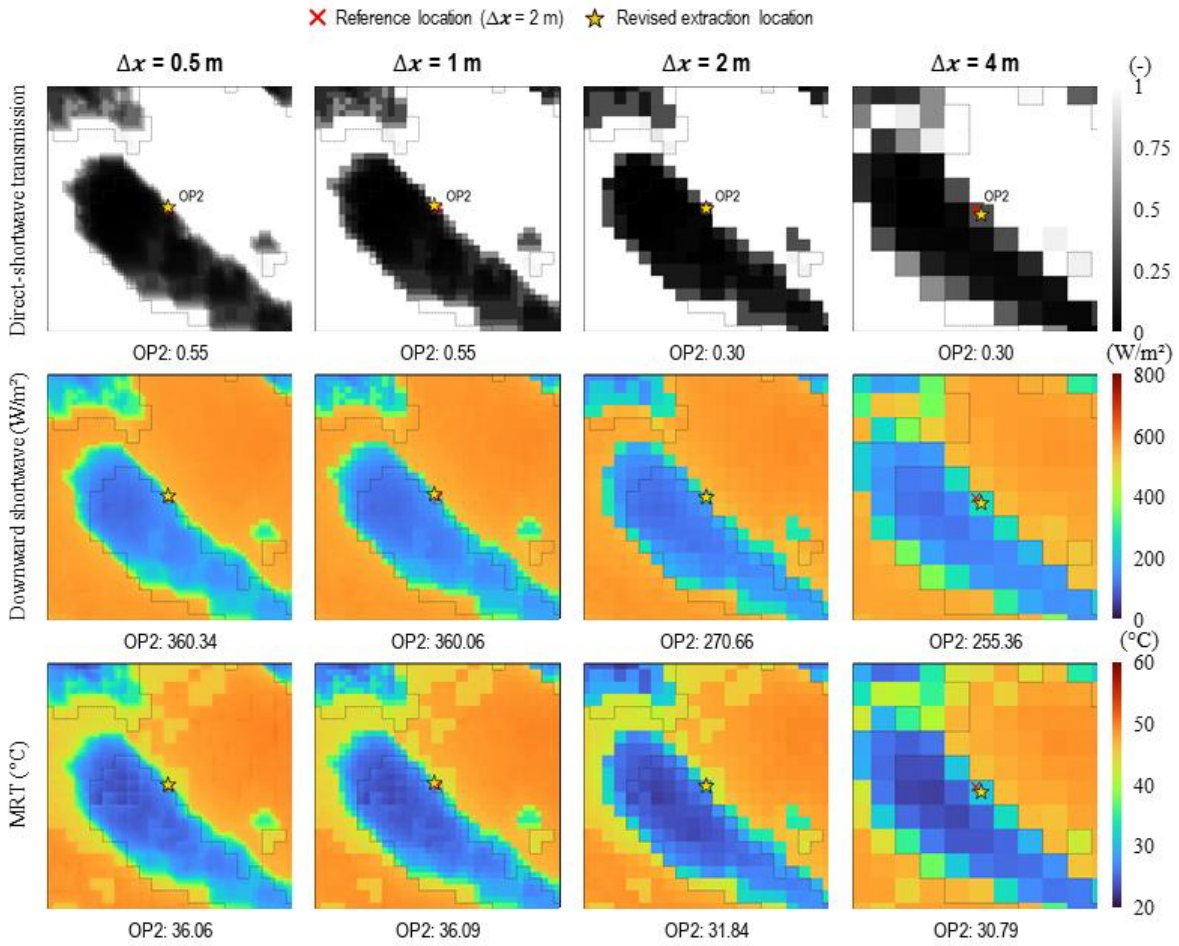

Figure R12. Results of the horizontal grid sensitivity experiments around OP2 at 11:00 LST on 7 July (① in Fig. R11). Columns show the 0.5, 1.0, 2.0, and 4.0 m grids from left to right. Rows show direct shortwave transmissivity, downward shortwave radiation, and MRT from top to bottom. Black outlines indicate canopy boundaries, the red cross marks the original OP2 location on the 2.0 m grid, and stars indicate the sampling locations selected at each resolution.

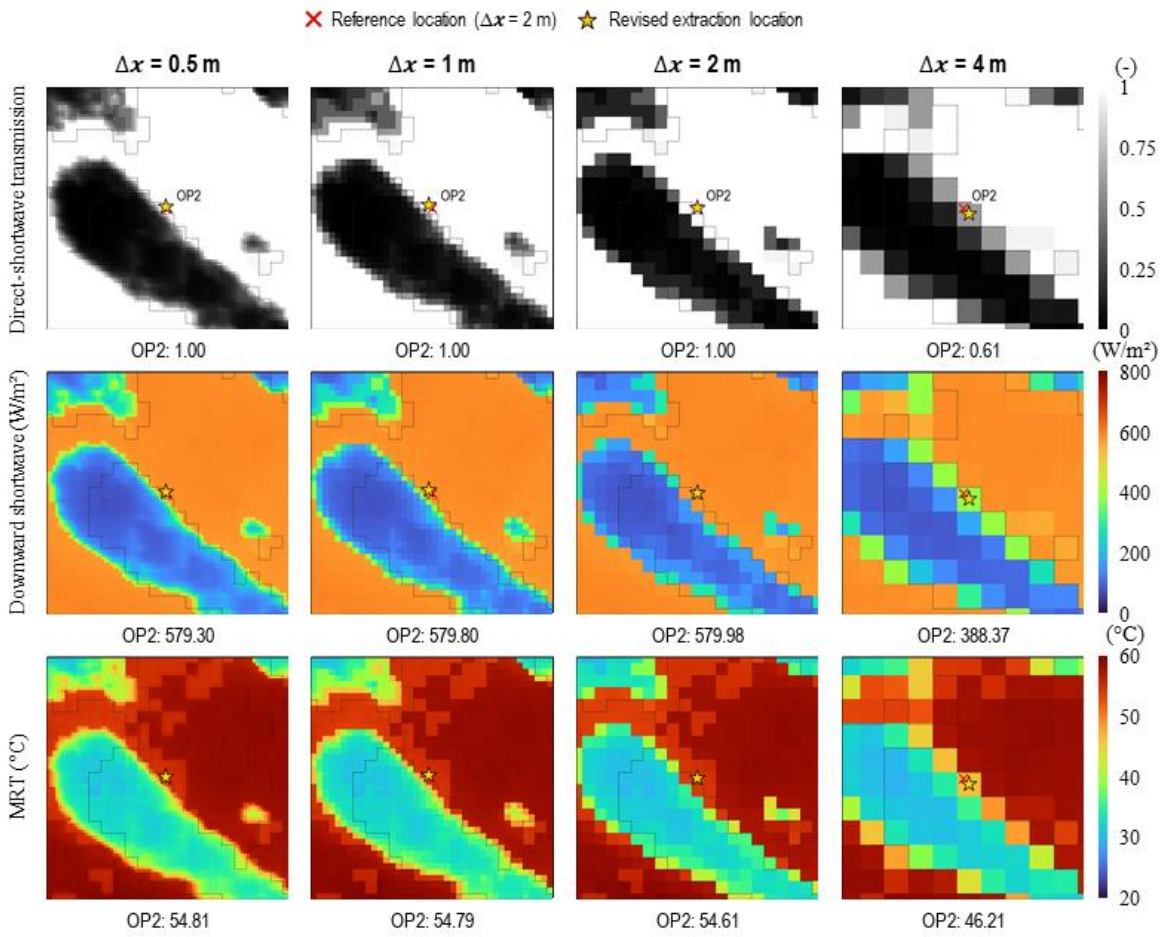

Figure R13. Results of the horizontal grid sensitivity experiments around OP2 at 10:00 LST on 12 July (② in Fig. R11). Columns show the 0.5, 1.0, 2.0, and 4.0 m grids from left to right. Rows show direct shortwave transmissivity, downward shortwave radiation, and MRT from top to bottom. Black outlines indicate canopy boundaries, the red cross marks the original OP2 location on the 2.0 m grid, and stars indicate the sampling locations selected at each resolution.

4. Sensitivity to fixed canopy transmissivity in Legacy SOLWEIG

→ To evaluate the effect of fixed canopy transmissivity in Legacy SOLWEIG, we used the full Göteborg domain from Table 5 and prescribed transmissivities of 3 %, 5 %, 10 %, 20 %, 30 %, and 40 %, while keeping all other inputs and the observation-point locations unchanged. Higher transmissivity resulted in higher MRT during periods of canopy shading. The transmissivity that gave the closest agreement with observations differed between the two sites (Fig. R14; Fig. C3d in Appendix C). At OP1, the lowest RMSE was 2.98 °C at a transmissivity of 0.10, whereas at OP2 it was 5.07 °C at a transmissivity of 0.03. Across all 41 observation–model pairs, the pooled RMSE ranged from 4.76 °C at a transmissivity of 0.03 to 10.06 °C at 0.40.

→ At OP1, increasing transmissivity from 0.03 to 0.40 raised downward shortwave radiation from 125.55 to 351.69 W m^{-2} and MRT from 25.78 to 40.26 °C at 10:00 LST on 23 May (Fig. R15). At OP2, downward shortwave radiation also increased from 116.30 to 334.50

W m^{-2} and MRT from 24.45 to 36.08 °C at 14:00 LST on 7 July (Fig. R16). These results show that, even with the same canopy geometry, the choice of fixed transmissivity can substantially affect solar radiation and MRT beneath the canopy.

→ Adjusting the fixed transmissivity reduced MRT errors at particular times and observation points, but no single transmissivity consistently performed best across all times and points. Across the 41 observation–model pairs, the pooled MRT RMSE of the full LEB configuration was 4.38 °C, lower than that of Legacy SOLWEIG at all fixed transmissivities tested (4.76–10.06 °C). These results suggest that a single fixed transmissivity cannot fully represent the variation in solar attenuation with solar position and the radiative path through the canopy, and that accounting for path-dependent transmissivity may be useful for predicting MRT.

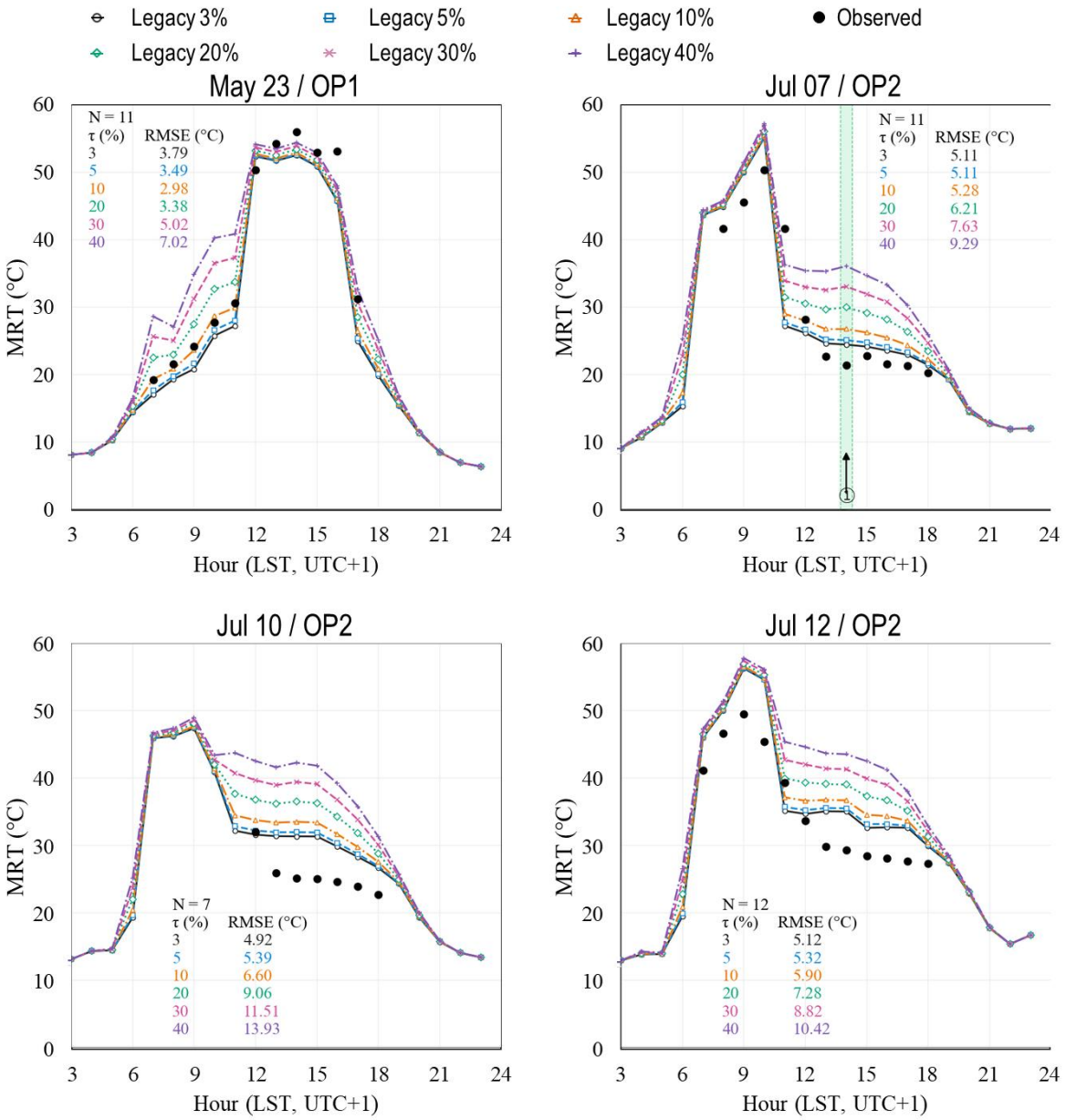

Figure R14. MRT time series for the fixed canopy transmissivity experiments in Legacy SOLWEIG. The upper panels show OP1 on 23 May and OP2 on 7 July, and the lower panels show OP2 on 10 and 12 July. Lines show results for transmissivities of 3 %, 5 %, 10 %, 20 %, 30 %, and 40 %, and black circles indicate observations.

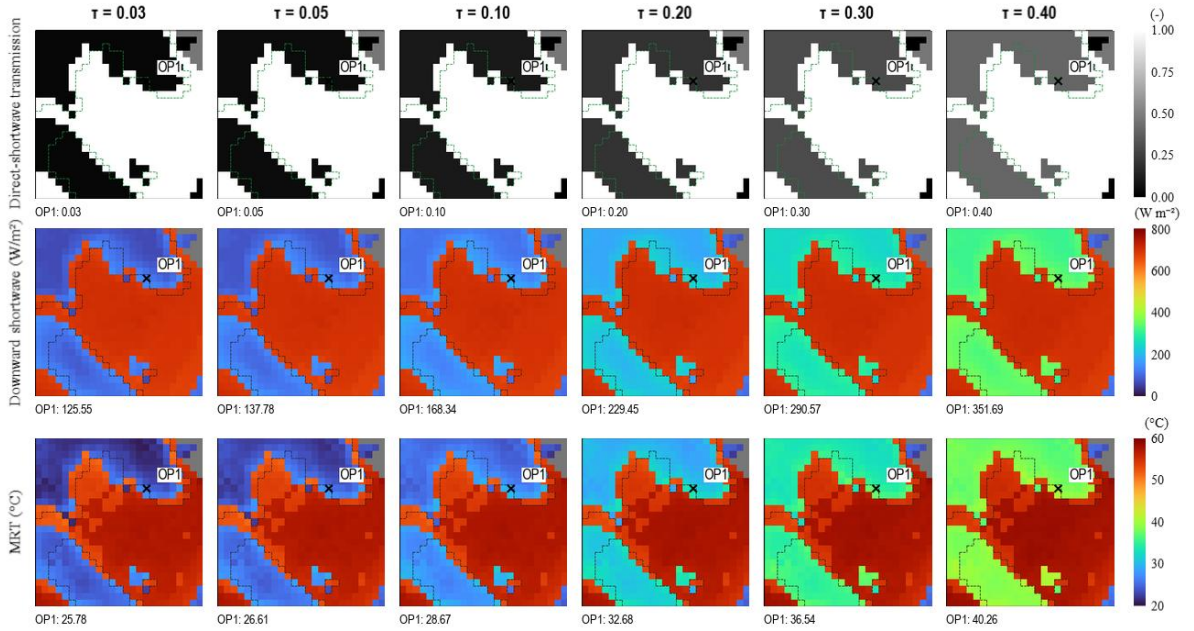

Figure R15. Spatial distributions around OP1 for the fixed canopy transmissivity experiments in Legacy SOLWEIG at 10:00 LST on 23 May. Columns show transmissivities of 3 %, 5 %, 10 %, 20 %, 30 %, and 40 % from left to right. Rows show direct shortwave transmissivity, downward shortwave radiation, and MRT from top to bottom. The canopy boundaries and the fixed sampling location at OP1 are shown. Numbers below the panels give the values at OP1.

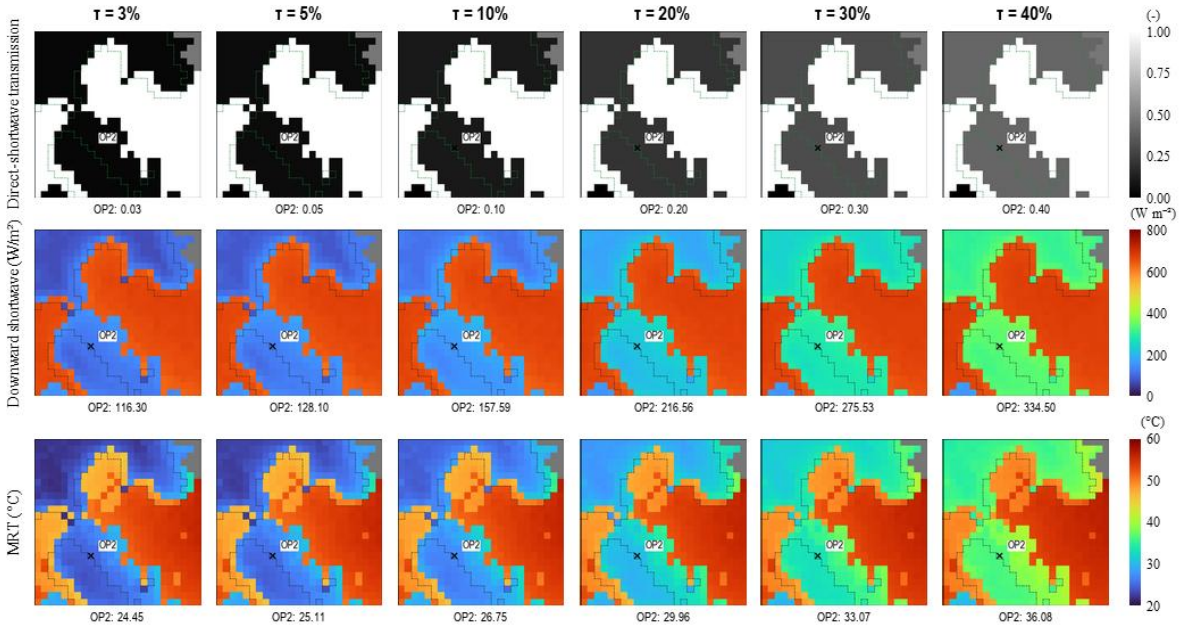

Figure R16. Spatial distributions around OP2 for the fixed canopy transmissivity experiments in Legacy SOLWEIG at 14:00 LST on 7 July. Columns show transmissivities of 3 %, 5 %, 10 %, 20 %, 30 %, and 40 % from left to right. Rows show direct shortwave transmissivity, downward shortwave radiation, and MRT from top to bottom. The canopy boundaries and the fixed sampling location at OP2 are shown. Numbers below the panels give the values at OP2.

References

Raabe, K., Pisek, J., Sonnentag, O., & Annuk, K. (2015). Variations of leaf inclination angle distribution with height over the growing season and light exposure for eight broadleaf tree species. Agricultural and Forest Meteorology, 214, 2-11.

Zeng, Y., Li, J., Liu, Q., Hu, R., Mu, X., Fan, W., ... & Wu, S. (2015). Extracting leaf area index by sunlit foliage component from downward-looking digital photography under clear-sky conditions. Remote Sensing, 7(10), 13410-13435.

Now, it reads:

Page 48:

… Third, the numerical representation of canopy structure involves several simplifying assumptions. The current version assumes a spherical leaf angle distribution with a leaf projection function of G_{proj} = 0.5, and LAD is assumed to be uniformly distributed within the canopy envelope when high-resolution observed LAD profiles are unavailable. However, actual LAD, leaf inclination and azimuth distributions, foliage clumping, and branch structure may vary with species, growth stage, canopy height, and position within the canopy. Consequently, G_{proj} may also vary with solar position and leaf orientation distribution. The sensitivity analysis in Appendix C showed that variations in G_{proj} associated with different

leaf orientation distributions can affect direct shortwave transmissivity and local MRT. Therefore, future developments should incorporate measured three-dimensional canopy geometry, spatially resolved LAD and leaf orientation distributions, and foliage clumping and branch structures, using data derived from terrestrial laser scanning, hemispherical photography, or within-canopy radiation measurements. …

Page 49:

… In the transmissivity experiments in Göteborg (41 observation–simulation pairs), the reference full LEB configuration yielded a lower pooled MRT RMSE (4.38 °C) than any of the six fixed-transmissivity Legacy SOLWEIG configurations (4.76–10.06 °C; Appendix C).

Page 60–65:

Appendix C. Sensitivity of MRT to canopy and grid configurations in Göteborg

C1. Sensitivity experiment design

We compared changes in mean radiant temperature (MRT) associated with leaf area density (LAD), leaf orientation distribution, horizontal grid resolution, and fixed canopy transmissivity in Göteborg. Except for the changes specified in each experiment, all other model inputs were held constant.

(i) Leaf area density. To isolate the influence of leaf area per unit canopy volume on direct solar radiation attenuation, we held the canopy geometry and the spherical leaf orientation distribution ($G_{\mathrm{proj}} = 0.5$) constant and assigned uniform LAD values of 0.2, 0.4, 0.6, 0.8, and 1.0 $m^2\ m^{-3}$ within the canopy. MRT was extracted at the original OP1 and OP2 coordinates for each condition. Changes in direct shortwave transmissivity were also compared at OP1 at 10:00 LST on 23 May and at OP2 at 14:00 LST on 7 July, when canopy shading occurred.

(ii) Leaf orientation distribution. The leaf projection function G_{proj} is the mean projected leaf area per unit leaf area, with the projection taken onto a plane perpendicular to the direction of radiation (Zeng et al., 2015). LAD was held at 0.6 $m^2\ m^{-3}$, and four leaf orientation distributions were considered: spherical, horizontal, vertical, and 45° inclined (Fig. C1a–d). For the spherical distribution, $G_{\mathrm{proj}} = 0.5$ regardless of solar position. For the other three distributions, the leaf inclination angle was fixed, and leaf azimuths within each voxel were assumed to be uniformly distributed. The dependence of G_{proj} on solar elevation is expressed as follows:

$$G_{proj}(\eta, \gamma) = \frac{1}{2\pi}\int_0^{2\pi} |\sin\eta\cos\gamma + \cos\eta\sin\gamma\cos\varphi| d\varphi \qquad \text{(C1)}$$

Here, η is the solar elevation angle, γ is the leaf inclination angle relative to the horizontal, and φ is the azimuthal difference between the leaf normal and the direction towards the sun. Equation (C1) represents the azimuthal average of the absolute dot product between the unit leaf normal and the unit vector pointing towards the sun. As solar elevation increases, the projection coefficient increases for horizontal leaves but decreases for vertical leaves (Fig. C1e).

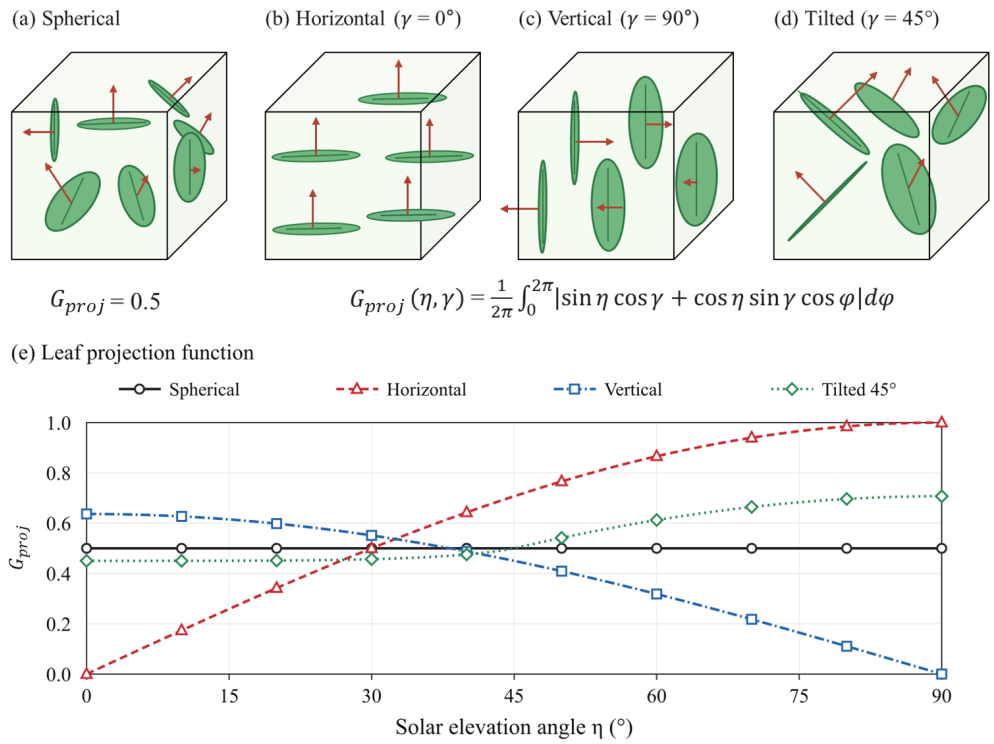

Figure C1. Leaf orientation distributions and the leaf projection function as a function of solar elevation. (a) Spherical, (b) horizontal, (c) vertical, and (d) 45° inclined leaf orientations, showing leaves and their normal vectors (red arrows). (e) Variation in G_{proj} with solar elevation angle η for the four distributions. Leaf azimuths were assumed to be uniformly distributed within each voxel for the vertical and 45° inclined distributions.

(iii) Horizontal grid resolution and sampling locations. To preserve the canopy geometry represented by the original 2 m grid as closely as possible, each original cell was subdivided into sixteen 0.5 m cells or four 1 m cells, while retaining the original canopy-top height, canopy-base height, and LAI. The 4 m grid was constructed by aggregating four adjacent 2 m cells. If any constituent cell contained canopy, the aggregated cell was classified as vegetated and assigned the maximum canopy-top height and minimum canopy-base height among the canopies it contained. LAI was calculated as an area-weighted mean including non-vegetated cells to conserve the total leaf area.

At each resolution, we examined the centres of non-building grid cells within a 3 m radius of the original OP1 and OP2 coordinates and extracted the MRT time series at the location yielding the lowest RMSE relative to observed MRT (Fig. C2).

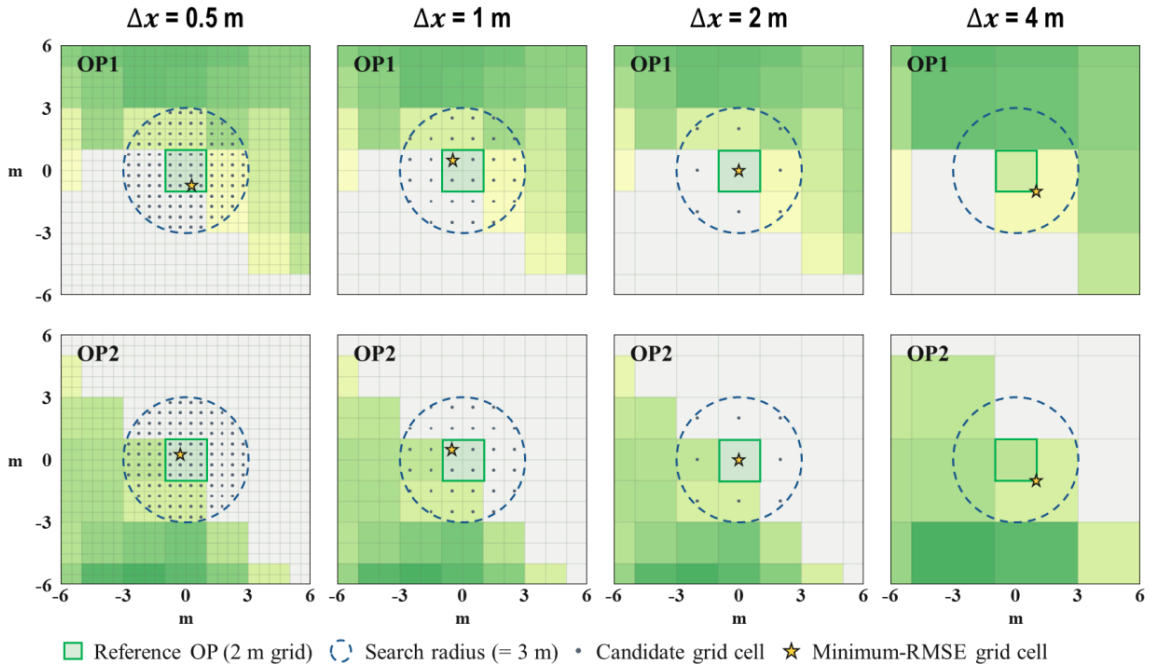

Figure C2. Canopy representation and candidate MRT sampling locations at OP1 (top) and OP2 (bottom) for horizontal grid resolutions of 0.5, 1.0, 2.0, and 4.0 m (left to right). Shades of green indicate canopy-top height, green squares mark the reference observation cells on the original 2.0 m grid, dashed circles show the 3 m search radius, dots indicate candidate sampling cells, and stars mark the minimum-RMSE cells.

(iv) Fixed canopy transmissivity in Legacy SOLWEIG. We compared the default fixed canopy transmissivity of 3 % in Legacy SOLWEIG with values of 5, 10, 20, 30, and 40 % for canopy-shaded locations. In each experiment, a single transmissivity value was applied uniformly to the entire canopy, while the meteorological inputs and canopy geometry were held constant.

C2. Sensitivity experiment results

Figure C3 compares MRT time series at OP1 on 23 May and at OP2 on 7, 10, and 12 July. The pooled RMSE was calculated from 41 paired observations and simulations across both sites (11 at OP1 and 30 at OP2).

(i) Leaf area density (Fig. C3a). Differences in MRT among LAD conditions occurred mainly from 06:00 to 11:00 LST at OP1 and during daytime hours other than 08:00–10:00 LST at OP2. During periods of canopy shading, lower LAD resulted in higher MRT, with particularly pronounced overestimation relative to observations at 0.2 m^2 m^{-3}. At OP1 at 10:00 LST on 23 May, increasing LAD from 0.2 to 0.6 m^2 m^{-3} reduced direct shortwave transmissivity from 0.357 to 0.045, downward shortwave radiation from 330.45 to 139.99 W m^{-2}, and MRT from 38.21 to 26.64 °C. At OP2 at 14:00 LST on 7 July, direct shortwave transmissivity likewise decreased from 0.151 to 0.003, and MRT decreased from 29.34 to 23.90 °C. At both times, most direct solar radiation was already attenuated at an LAD of 0.6 m^2 m^{-3}, so further increases in LAD produced only small changes in MRT. The pooled RMSEs at LAD values of 0.2, 0.4, 0.6, 0.8, and 1.0 m^2 m^{-3} were 8.01, 5.05, 4.40, 4.31, and

4.36 °C, respectively, with differences of less than 0.1 °C over the range 0.6–1.0 m^2 m^{-3}.

(ii) Leaf orientation distribution (Fig. C3b). The diurnal variations in MRT were generally similar among the four leaf orientation distributions, but substantial differences occurred when the canopy partially attenuated direct solar radiation or when conditions transitioned between sun and shade. These differences appeared around 07:00 and 11:00 LST at OP1 on 23 May and around 06:00 and 11:00 LST at OP2 on 7 July. At OP1 at 11:00 LST on 23 May, the leaf projection coefficient was higher for horizontal leaves (0.76) than for vertical leaves (0.42), while direct shortwave transmissivity was lower (0.18 versus 0.39). Downward shortwave radiation was 244.18 and 371.04 W m^{-2} for horizontal and vertical leaves, respectively, and the corresponding MRT values were 32.33 and 38.27 °C, a difference of approximately 5.9 °C. By contrast, differences among leaf orientations were small when direct solar radiation was almost unattenuated or largely blocked. The pooled RMSE ranged from 4.40 to 4.55 °C over the full observation period, and no leaf orientation distribution consistently yielded the lowest error at both sites.

(iii) Horizontal grid resolution and sampling locations (Fig. C3c). At each resolution, the grid-cell centre with the lowest RMSE was selected within a 3 m radius of the original observation point. At grid resolutions of 0.5, 1, 2, and 4 m, the RMSEs at OP1 were 3.49, 3.62, 3.69, and 4.37 °C, respectively, while those pooled over the three observation days at OP2 were 4.82, 4.79, 4.61, and 4.23 °C. At OP2, the resolution that gave the closest agreement with observations also varied with time. At 11:00 LST on 7 July, direct shortwave transmissivity was 0.55 on the 0.5 and 1 m grids and 0.30 on the 2 and 4 m grids. Simulated MRT was approximately 36 °C on the two finer grids and 31–32 °C on the two coarser grids; the finer-grid results were closer to the observed value of 41.61 °C. In contrast, at 10:00 LST on 12 July, direct solar radiation was unattenuated on the 0.5–2 m grids, yielding MRT values of 54.61–54.81 °C. On the 4 m grid, direct shortwave transmissivity was 0.61 and MRT was 46.21 °C, closer to the observed value of 45.36 °C.

(iv) Fixed canopy transmissivity in Legacy SOLWEIG (Fig. C3d). In Legacy SOLWEIG, higher fixed transmissivity resulted in higher MRT during periods of canopy shading. At OP1 at 10:00 LST on 23 May, increasing transmissivity from 3 % to 40 % raised downward shortwave radiation from 125.55 to 351.69 W m^{-2} and MRT from 25.78 to 40.26 °C. At OP2 at 14:00 LST on 7 July, MRT likewise increased from 24.45 to 36.08 °C. The fixed transmissivity yielding the closest agreement with observations differed between the sites: 10 % at OP1 (RMSE = 2.98 °C) and 3 % at OP2 (RMSE = 5.07 °C). Across the same 41 observation–simulation pairs, the pooled RMSE for the six fixed-transmissivity cases ranged from 4.76 to 10.06 °C, compared with 4.38 °C for the Full LEB configuration.

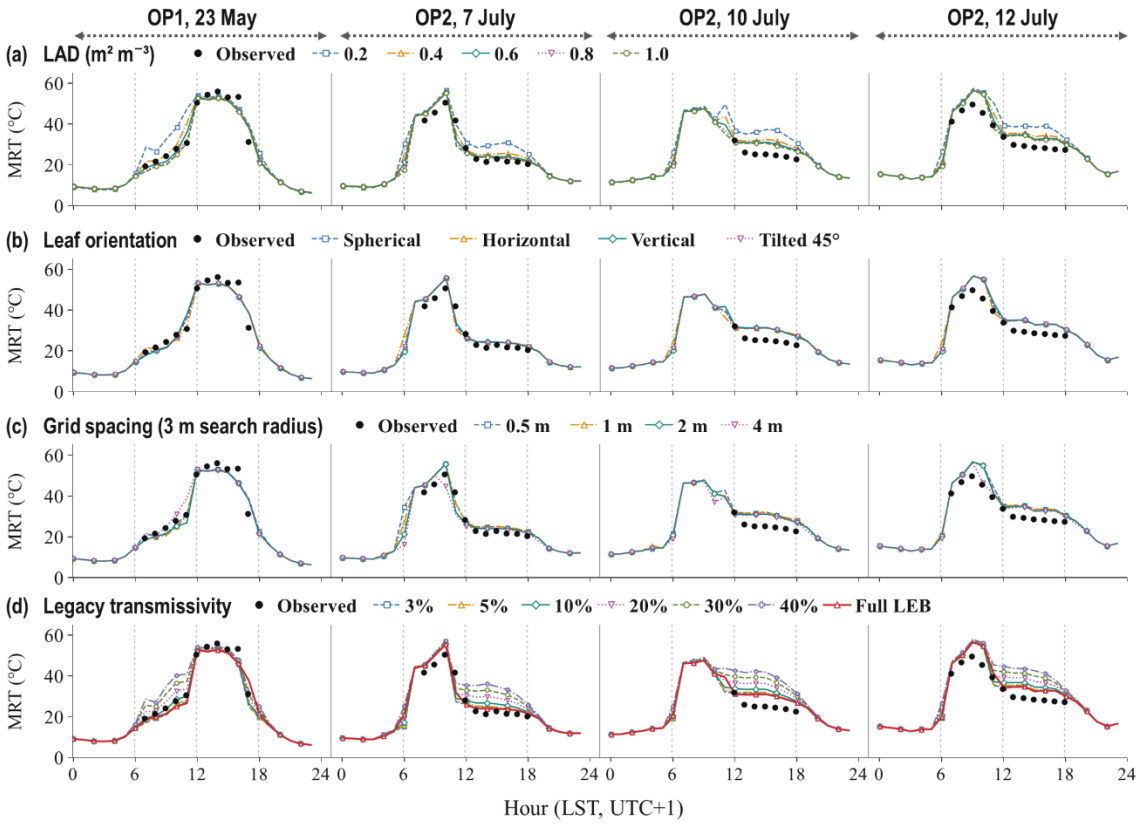

Figure C3. MRT time series for four observation days in Göteborg. From left to right, the columns show OP1 on 23 May and OP2 on 7, 10, and 12 July; black circles indicate observations. (a) Uniform LAD, (b) leaf orientation distribution, (c) horizontal grid resolution, and (d) fixed canopy transmissivity in Legacy SOLWEIG and the reference Full LEB simulation. Panel (c) uses sampling locations reselected within a 3 m radius, whereas panels (a), (b), and (d) use the original OP coordinates. All times are local standard time (LST, UTC+1).

C3. Implications, limitations, and future work

When evaluating radiative shielding by tree canopies, errors averaged over the full observation period should be distinguished from differences occurring when direct solar radiation partially penetrates the canopy. At the two representative times, direct shortwave transmissivity was already 0.05 or lower at an LAD of 0.6 m^2 m^{-3}, and further increases in LAD therefore produced little change in MRT. In contrast, during transitions between sun and shade, MRT varied with leaf orientation even at the same LAD. Furthermore, the fixed transmissivity that best matched observations at one site did not necessarily perform best at the other. This indicates that a single transmissivity value cannot readily represent the shading conditions at both sites and highlights the importance of distinguishing attenuation according to solar position and the radiative path through the canopy.

This comparison was limited to four observation days at two sites, and neither LAD nor leaf orientation distributions were measured directly for the individual canopies. The 0.5 and 1 m grids were generated by subdividing the original 2 m data and therefore did not incorporate additional fine-scale detail of the actual canopy boundaries. Moreover, because the same observations were used both to select sampling locations and to evaluate errors, the

RMSEs obtained after reselection cannot by themselves establish the superiority of a particular grid resolution. Future evaluations should use measured high-resolution three-dimensional canopy geometry together with observations of within-canopy leaf density and orientation, keep the sampling locations fixed, and compare the timing of sun–shade transitions and MRT using independent observation days.

Comment 5
The literature review and presentation need improvement. **The introduction should more clearly distinguish findings from field measurements and numerical simulations. It should explain how existing studies represent canopy attenuation and leaf temperature, and identify the specific unresolved issue addressed by this implementation.** **The statement that leaf temperature can differ significantly from air temperature should be supported with quantitative examples and the conditions under which those differences occur. This would give readers a clearer basis for judging the importance of the LEB extension.**

→ We sincerely thank the reviewer for the thoughtful and constructive comments, which have helped us clarify the interpretation of previous studies and the motivation for developing the model. In response, we have revised the Introduction to more clearly distinguish findings from field measurements and numerical simulations. For example, we have distinguished the reduction in globe temperature observed under tree shade by Armson et al. (2012) from the approximately 23 °C reduction in MRT simulated for the sunlit area by Park et al. (2018) in response to changes in LAD under specific street-canyon conditions. We have thus clarified the methods and conditions under which these findings were obtained.

→ We have also expanded the description of how existing urban microclimate models represent canopy radiative attenuation and leaf temperature. ENVI-met calculates leaf temperature through a leaf energy balance, whereas RTM 3.0 in the PALM model system 6.0 calculates canopy radiative attenuation using three-dimensional LAD while assuming that leaf temperature equals the surrounding air temperature when calculating vegetation longwave emission. Through this comparison with existing models, we have clarified that the contribution of the present study is not to introduce new physical principles, but rather to integrate path-dependent canopy attenuation and a voxel-scale leaf energy balance into the existing SOLWEIG framework under prescribed meteorological forcing, and to evaluate the resulting model.

→ Finally, to strengthen the discussion of differences between leaf and air temperatures, we have added quantitative findings from field observations together with the conditions under which they were obtained. Leuzinger and Körner (2007) reported that, under clear-sky conditions with sufficient soil moisture and an air temperature of approximately 25 °C, mean leaf temperatures in dense broadleaved canopies were about 4.5–5.0 °C higher than air temperature, with within-canopy leaf-temperature ranges of 10–12 °C. Miller et al. (2021) also reported that sunlit leaves in the upper canopy of a wet tropical forest were up to approximately 5 °C warmer than the surrounding air under strong solar radiation, whereas shaded leaves remained close to air temperature. These observational findings help demonstrate that leaf–air temperature differences depend on environmental conditions, including solar exposure and position within the canopy, and provide a clearer physical motivation for explicitly calculating leaf temperature using the LEB module. However, we have also clarified that differences between leaf and air temperatures do not necessarily translate into changes of the same magnitude in pedestrian MRT. Therefore, the contribution

of the LEB module should be evaluated not only in terms of MRT prediction but also in terms of its ability to diagnose leaf temperature and sensible–latent heat partitioning within the canopy.

Now, it reads:

Page 2–5:

…… Under clear-sky conditions with strong solar forcing, MRT can vary substantially over short distances depending on direct solar exposure, surface reflectance, surface temperature, and sky view factor. Differences in MRT between sunlit and shaded urban spaces can be substantial; for instance, Lau et al. (2015) reported variations of up to approximately 30 °C within urban environments in a numerical modelling study of three European cities. Direct measurement of such three-dimensional radiative environments requires observations of shortwave and longwave radiation fluxes in six directions, which is often constrained by instrumentation, installation logistics, observation duration, and spatial representativeness (Thorsson et al., 2007; Johansson et al., 2014). ……

The spatial heterogeneity of urban radiative environments is controlled not only by building morphology but also significantly by green infrastructure. Urban trees are a widely implemented nature-based solution for mitigating pedestrian heat stress. They actively modify the local thermal environment through transpirational cooling, while tree crowns intercept direct shortwave radiation and alter the magnitude and directionality of radiation reaching pedestrians through scattering, transmission, and reflection. Among these processes, the most immediate effect of trees on daytime MRT reduction is the physical interception of direct shortwave radiation. Field measurements provide direct evidence of these shading effects. Armson et al. (2012) measured reductions in globe temperature of up to 5–7 °C under tree shade during summer in Manchester, UK. Similarly, the field studies of Kántor et al. (2018) and Middel et al. (2016) demonstrated the benefits of shading for pedestrian radiative exposure and outdoor thermal comfort.

The radiative efficacy of trees depends on canopy architecture, species characteristics, and the distribution of leaf area density (LAD). LAD, describing the one-sided leaf area per unit canopy volume, is a key parameter for shortwave attenuation because it determines the cumulative leaf area and optical depth along any discrete radiative trajectory. Konarska et al. (2014) measured solar-radiation transmissivity through single urban trees in Göteborg, Sweden, and showed that direct shortwave transmissivity through foliated tree crowns was only approximately 1.3–5.3 %. Complementing these observations, numerical sensitivity experiments allow the effects of individual canopy properties to be examined under controlled model conditions. Using a multilayer radiation model, Park et al. (2018) simulated a reduction in pedestrian MRT of approximately 23 °C in the sunlit area at 13:00 LST when LAD increased from 0 to 1 m^2 m^{-3} in the specific street-canyon scenario examined. This reduction represents a simulated response to changes in LAD rather than an observed cooling effect. Other modelling studies have examined how LAD, crown dimensions, and tree planting configurations influence urban radiative exchange and thermal conditions (Krayenhoff et al., 2014; Ryu et al., 2016; Morakinyo and Lam, 2016; Park et al., 2019). Together, field observations and numerical experiments provide complementary evidence for representing canopy structure and path-dependent attenuation when assessing the

radiative effects of urban trees.

…… These models simplify urban morphology, radiative transfer, surface temperature, and vegetation effects to varying degrees depending on their intended applications and computational constraints.

Their treatments of canopy attenuation and leaf temperature also differ. ENVI-met represents solar interception using plant geometry and LAD and calculates leaf temperature from a leaf-surface energy balance that accounts for radiative exchange, sensible heat transfer, and transpiration (Bruse and Fleer, 1998; Simon et al., 2018). In contrast, the Radiative Transfer Model 3.0 integrated into PALM model system 6.0 calculates canopy attenuation by tracing radiation through a three-dimensional LAD field but assumes leaf temperature to be equal to the surrounding air temperature when calculating vegetation thermal emission (Maronga et al., 2020; Krč et al., 2021).

Among these models, SOLWEIG (SOlar and LongWave Environmental Irradiance Geometry) is a widely utilized 2.5-dimensional radiation model designed to calculate the spatial distribution of shortwave and longwave radiation fluxes and MRT across complex urban settings with high computational efficiency (Lindberg et al., 2008). ……

Recent developments in SOLWEIG have progressively shifted from purely empirical or air-temperature-based surface thermal boundary conditions toward an explicit treatment of surface thermal state based on radiative balance and material properties. Wallenberg et al. (2026) introduced a step-heating parameterization for wall surface temperatures in SOLWEIG using wall thermophysical properties, facet radiation balance, and ambient air temperature. They showed that resolving wall surface temperatures explicitly can lead to differences in MRT of up to approximately 2.5 °C compared with the previous version of SOLWEIG, demonstrating that SOLWEIG can be extended to represent the thermal state of urban surfaces more explicitly. However, while wall surfaces are treated as thermally dynamic facets, the legacy vegetation module in SOLWEIG still relies on a single representative transmissivity and an isothermal assumption. The specific gap addressed here is therefore the absence, in the Legacy SOLWEIG configuration considered in this study, of a coupled treatment linking path-dependent canopy attenuation to voxel-scale leaf temperature and vegetation longwave emission. The challenge is to integrate these processes within SOLWEIG's pedestrian-radiation framework while retaining its use of prescribed meteorological forcing, rather than introducing a prognostic atmospheric model.

The Legacy SOLWEIG vegetation module thus contains two fundamental simplifications. First, shortwave transmissivity through the canopy is prescribed as a static, bulk representative value for a given vegetation class. While computationally efficient, this treatment cannot explicitly account for the three-dimensional LAD distribution within a canopy, solar path length, canopy-edge partial transmission, or spatial differences between sunlit and shaded foliage. In real tree canopies, shortwave attenuation varies with the cumulative LAD and optical depth along the incoming solar beam; consequently, transmissivity differs substantially between the dense canopy core, crown edges, and internal gaps even within the same tree. Second, the Legacy SOLWEIG assumes the vegetation surface temperature, or leaf temperature, to be equal to ambient air temperature. Although this assumption provides a practical simplification for MRT estimation, the legacy vegetation treatment does not explicitly calculate the intra-canopy temperature variations or the sensible and latent heat exchanges that determine leaf temperature (Lindberg and Grimmond, 2011).

Field measurements show that the magnitude of leaf–air temperature differences depends on canopy structure and radiative exposure. Using infrared thermography in a mature temperate forest, Leuzinger and Körner (2007) found that, under clear skies and ample soil moisture, dense broad-leaved crowns had mean leaf temperatures approximately 4.5–5.0 °C above an air temperature of 25 °C, with within-crown temperature ranges of 10–12 °C. In a wet tropical forest, Miller et al. (2021) observed upper-canopy sunlit leaves up to approximately 5 °C warmer than the air at the highest radiation intensity, whereas shaded leaves in the middle canopy and understory remained close to air temperature. Herpin et al. (2024) also conducted field measurements in a reduced-scale street canyon in Angers, France, recording leaf temperatures at different positions within the canopies of well-watered ornamental apple trees. These measurements provide valuable observational data for examining spatial variations in leaf temperature within urban tree canopies.

These findings motivate the explicit calculation of leaf temperature and vegetation longwave emission from the local leaf energy balance. However, a large leaf–air temperature difference does not necessarily translate into a similarly large change in pedestrian MRT, because the resulting radiative exposure also depends on canopy visibility and radiation from other surrounding sources. The value of an LEB extension should therefore be assessed in terms of both its contribution to pedestrian radiation estimates and its ability to diagnose leaf thermal states and sensible–latent heat partitioning.

To overcome these limitations, this study develops SOLWEIG-LEB (Leaf Energy Balance) v1.0, hereafter referred to as SOLWEIG-LEB, an extension that integrates LAD-based path-dependent canopy attenuation and a voxel-scale leaf energy balance into the existing SOLWEIG framework. Its contribution lies in the integration and evaluation of these processes within SOLWEIG, rather than in introducing canopy attenuation or leaf energy balance as new physical concepts. By integrating voxel-resolved LAD information into the 2.5D SOLWEIG framework, the model captures fine-scale canopy attenuation physics while retaining the underlying building and ground geometry of the original radiation model. The objectives of this study are fourfold. First, we develop an LAD-based attenuation scheme that uses the leaf projection function and cumulative leaf area along radiative paths to represent spatial and temporal variations in canopy shortwave transmissivity. Second, we integrate a voxel-scale leaf energy balance that accounts for absorbed radiation, leaf thermal emission, sensible heat exchange, and transpiration to diagnose leaf temperature, vegetation longwave emission, and sensible and latent heat fluxes. Third, we evaluate leaf temperature, photosynthetically active radiation (PAR), transpiration, and MRT against observations in Angers, France, with additional leaf-temperature validation in Mainz, Germany, and we evaluate the integrated pedestrian-level radiative environment against six-directional radiation fluxes and MRT observations in Göteborg, Sweden. Finally, we distinguish the contributions of LAD-based attenuation and leaf-energy-balance-driven vegetation emission to pedestrian-level radiation and MRT, and examine the additional information provided by voxel-scale leaf temperature and energy-partitioning diagnostics. The remainder of this paper is organized as follows. Section 2 describes the mathematical formulation and computational framework of SOLWEIG-LEB v1.0, including the LAD-based canopy attenuation scheme, directional radiation modifications, and the leaf energy balance module. Section 3 presents the observational datasets and numerical experimental designs for the Angers and Göteborg sites. Section 4 presents the model evaluation results, comparative performance against Legacy SOLWEIG, and voxel-scale spatial diagnostics. Section 5 discusses the physical interpretations, computational scope, limitations, and future

development, and Section 6 summarizes the main conclusions.

Development of SOLWEIG-LEB v1.0: An urban radiation model integrating LAD-based canopy shortwave attenuation and leaf energy balance

Geon Kang[a], Fredrik Lindberg[b], Eliott Bridoux[c], Nils Wallenberg[b], Jae-Jin Kim[d*]

[a]*Institute of Sustainable Earth and Environmental Dynamics (SEED), Pukyong National University, Busan, Republic of Korea*
[b]*Department of Earth Sciences, University of Gothenburg, Gothenburg, Medicinaregatan 7B, 413 90 Göteborg, Sweden*
[c]*DER Génie Civil et Environnement, ENS Paris-Saclay, Université Paris-Saclay, Gif-sur-Yvette, 91190, France.*
[d]*Division of Earth and Environmental System Sciences, Pukyong National University, Busan, Korea*

*Corresponding Author: Prof. Jae–Jin Kim, Department of Environmental Atmospheric Sciences, Pukyong National University, 45, Yongso–ro, Nam–Gu, Busan 48513, Korea.
Phone: +82–51–629–6645
Fax: +82–51–629–6638
E–mail: jjkim@pknu.ac.kr

Abstract

Urban trees are widely used to mitigate pedestrian heat stress by providing shade and modifying the surrounding radiative environment. Accurately representing these effects is important for evaluating urban greening strategies, yet simplified treatments of canopy transmission and vegetation temperature can limit pedestrian-level radiation and mean radiant temperature (MRT) estimates. SOLWEIG is a widely used urban radiation model for spatially resolving pedestrian radiative environments, but its conventional vegetation scheme applies a fixed canopy transmissivity and assumes vegetation temperature equals air temperature. To address these limitations, we developed SOLWEIG-LEB v1.0, which combines path-dependent shortwave attenuation based on leaf area density (LAD), the leaf projection function, and radiative path length with a voxel-scale leaf energy balance that diagnoses leaf temperature, vegetation longwave emission, and sensible and latent heat fluxes. The model was evaluated using three field datasets. Against leaf-temperature observations in Angers, France, Pearson correlation coefficients (r) were 0.97 in both regions A and B, and root mean square errors (RMSEs) were 1.72 and 1.61 °C, respectively. Angers observations were also used to evaluate canopy photosynthetically active radiation, transpiration, and MRT, while Mainz, Germany, provided additional leaf-temperature validation. Against six-directional radiation and MRT observations in Göteborg, Sweden, SOLWEIG-LEB reduced RMSEs for total shortwave radiation from 231.74 to 203.66 W m^{-2}, total longwave radiation from 83.42 to 78.93 W m^{-2}, and MRT from 4.76 to 4.38 °C relative to Legacy SOLWEIG. Differences were greatest near canopy edges and partially obstructed locations, highlighting the importance of spatially variable canopy transmission. SOLWEIG-LEB provides a more physically explicit framework for assessing urban-tree radiative effects and pedestrian thermal environments.

Keywords: urban microclimate; SOLWEIG-LEB; leaf energy balance; canopy radiative transfer; mean radiant temperature

1. Introduction

Pedestrian thermal comfort in urban areas is strongly influenced not only by air temperature, humidity, and wind speed, but also by shortwave and longwave radiation received from surrounding buildings, ground surfaces, vegetation, and the sky. Mean radiant temperature (MRT) integrates the three-dimensional radiative exposure experienced by a human body in outdoor environments and is therefore a key input to outdoor thermal comfort indices such as the Physiological Equivalent Temperature (PET) and the Universal Thermal Climate Index (UTCI) (Mayer and Höppe, 1987; Höppe, 1999; Błażejczyk et al., 2010). Under clear-sky conditions with strong solar forcing, MRT can vary substantially over short distances depending on direct solar exposure, surface reflectance, surface temperature, and sky view factor. Differences in MRT between sunlit and shaded urban spaces can be substantial; for instance, Lau et al. (2015) reported variations of up to approximately 30 °C within urban environments in a numerical modelling study of three European cities. Direct measurement of such three-dimensional radiative environments requires observations of shortwave and longwave radiation fluxes in six directions, which is often constrained by instrumentation, installation logistics, observation duration, and spatial representativeness (Thorsson et al., 2007; Johansson et al., 2014). Therefore, radiation models that can spatially estimate pedestrian-level radiative environments and MRT across complex urban geometries are essential for climate-resilient urban design and thermal-environment assessment.

The spatial heterogeneity of urban radiative environments is controlled not only by building morphology but also significantly by green infrastructure. Urban trees are a widely implemented nature-based solution for mitigating pedestrian heat stress. They actively modify the local thermal environment through transpirational cooling, while tree crowns intercept direct shortwave radiation and alter the magnitude and directionality of radiation reaching pedestrians through scattering, transmission, and reflection. Among these processes, the most immediate effect of trees on daytime MRT reduction is the physical interception of direct shortwave radiation. Field measurements provide direct evidence of these shading effects. Armson et al. (2012) measured reductions in globe temperature of up to 5–7 °C under tree shade during summer in Manchester, UK. Similarly, the field studies of Kántor et al. (2018) and Middel et al. (2016) demonstrated the benefits of shading for pedestrian radiative exposure and outdoor thermal comfort.

The radiative efficacy of trees depends on canopy architecture, species characteristics, and the distribution of leaf area density (LAD). LAD, describing the one-sided leaf area per unit canopy volume, is a key parameter for shortwave attenuation because it determines the cumulative leaf area and optical depth along any discrete radiative trajectory. Konarska et al. (2014) measured solar-radiation transmissivity through single urban trees in Göteborg, Sweden, and showed that direct shortwave transmissivity through foliated tree crowns was only approximately 1.3–5.3 %. Complementing these observations, numerical sensitivity experiments allow the effects of individual canopy properties to be examined under controlled model conditions. Using a multilayer radiation model, Park et al. (2018) simulated a reduction in pedestrian MRT of approximately 23 °C in the sunlit area at 13:00 LST when LAD increased from 0 to 1 $m^2 m^{-3}$ in the specific street-canyon scenario examined.

This reduction represents a simulated response to changes in LAD rather than an observed cooling effect. Other modelling studies have examined how LAD, crown dimensions, and tree planting configurations influence urban radiative exchange and thermal conditions (Krayenhoff et al., 2014; Ryu et al., 2016; Morakinyo and Lam, 2016; Park et al., 2019). Together, field observations and numerical experiments provide complementary evidence for representing canopy structure and path-dependent attenuation when assessing the radiative effects of urban trees.

Various urban microclimate and radiation models have been developed to calculate outdoor MRT and pedestrian-level radiative fields. ENVI-met and PALM/PALM-4U are high-resolution, three-dimensional prognostic microclimate or urban climate modelling systems that represent complex interactions among urban surfaces, vegetation, and the atmospheric boundary layer, resolving airflow, turbulence, surface energy balance, heat and moisture transport, thermal comfort, and air-quality-related processes (Bruse and Fleer, 1998; Maronga et al., 2020). In contrast, models such as RayMan, SkyHelios, CityComfort+, VTUF-3D, and SOLWEIG are more focused on computationally efficient estimation of pedestrian-level radiation fluxes and MRT (Matzarakis et al., 2007, 2010; Fröhlich and Matzarakis, 2018; Huang et al., 2014; Nice et al., 2018; Lindberg et al., 2008). These models simplify urban morphology, radiative transfer, surface temperature, and vegetation effects to varying degrees depending on their intended applications and computational constraints.

Their treatments of canopy attenuation and leaf temperature also differ. ENVI-met represents solar interception using plant geometry and LAD and calculates leaf temperature from a leaf-surface energy balance that accounts for radiative exchange, sensible heat transfer, and transpiration (Bruse and Fleer, 1998; Simon et al., 2018). In contrast, the Radiative Transfer Model 3.0 integrated into PALM model system 6.0 calculates canopy attenuation by tracing radiation through a three-dimensional LAD field but assumes leaf temperature to be equal to the surrounding air temperature when calculating vegetation thermal emission (Maronga et al., 2020; Krč et al., 2021).

Among these models, SOLWEIG (SOlar and LongWave Environmental Irradiance Geometry) is a widely utilized 2.5-dimensional radiation model designed to calculate the spatial distribution of shortwave and longwave radiation fluxes and MRT across complex urban settings with high computational efficiency (Lindberg et al., 2008). In SOLWEIG, high-resolution Digital Surface Models (DSMs) of terrain, buildings, and vegetation, combined with standard meteorological forcing, are used to calculate shadow patterns, sky view factors, ground view factors, and reflected shortwave radiation, ultimately resolving directional pedestrian-level radiative loads. Lindberg and Grimmond (2011) extended SOLWEIG by introducing a vegetation scheme that distinguishes between canopy top height and trunk-zone height, enabling the model to represent shadow patterns cast by urban trees and shrubs. This approach provides a practical framework for evaluating spatial variations in vegetation shading and MRT using relatively simple spatial data.

Recent developments in SOLWEIG have progressively shifted from purely empirical or air-temperature-based surface thermal boundary conditions toward an explicit treatment of surface thermal state based on radiative balance and material properties. Wallenberg et al. (2026) introduced a step-heating parameterization for wall surface temperatures in SOLWEIG using wall thermophysical properties, facet radiation balance, and ambient air temperature. They showed that

resolving wall surface temperatures explicitly can lead to differences in MRT of up to approximately 2.5 °C compared with the previous version of SOLWEIG, demonstrating that SOLWEIG can be extended to represent the thermal state of urban surfaces more explicitly. However, while wall surfaces are treated as thermally dynamic facets, the legacy vegetation module in SOLWEIG still relies on a single representative transmissivity and an isothermal assumption. The specific gap addressed here is therefore the absence, in the Legacy SOLWEIG configuration considered in this study, of a coupled treatment linking path-dependent canopy attenuation to voxel-scale leaf temperature and vegetation longwave emission. The challenge is to integrate these processes within SOLWEIG's pedestrian-radiation framework while retaining its use of prescribed meteorological forcing, rather than introducing a prognostic atmospheric model.

The Legacy SOLWEIG vegetation module thus contains two fundamental simplifications. First, shortwave transmissivity through the canopy is prescribed as a static, bulk representative value for a given vegetation class. While computationally efficient, this treatment cannot explicitly account for the three-dimensional LAD distribution within a canopy, solar path length, canopy-edge partial transmission, or spatial differences between sunlit and shaded foliage. In real tree canopies, shortwave attenuation varies with the cumulative LAD and optical depth along the incoming solar beam; consequently, transmissivity differs substantially between the dense canopy core, crown edges, and internal gaps even within the same tree. Second, the Legacy SOLWEIG assumes the vegetation surface temperature, or leaf temperature, to be equal to ambient air temperature. Although this assumption provides a practical simplification for MRT estimation, the legacy vegetation treatment does not explicitly calculate the intra-canopy temperature variations or the sensible and latent heat exchanges that determine leaf temperature (Lindberg and Grimmond, 2011).

Field measurements show that the magnitude of leaf–air temperature differences depends on canopy structure and radiative exposure. Using infrared thermography in a mature temperate forest, Leuzinger and Körner (2007) found that, under clear skies and ample soil moisture, dense broad-leaved crowns had mean leaf temperatures approximately 4.5–5.0 °C above an air temperature of 25 °C, with within-crown temperature ranges of 10–12 °C. In a wet tropical forest, Miller et al. (2021) observed upper-canopy sunlit leaves up to approximately 5 °C warmer than the air at the highest radiation intensity, whereas shaded leaves in the middle canopy and understory remained close to air temperature. Herpin et al. (2024) also conducted field measurements in a reduced-scale street canyon in Angers, France, recording leaf temperatures at different positions within the canopies of well-watered ornamental apple trees. These measurements provide valuable observational data for examining spatial variations in leaf temperature within urban tree canopies.

These findings motivate the explicit calculation of leaf temperature and vegetation longwave emission from the local leaf energy balance. However, a large leaf–air temperature difference does not necessarily translate into a similarly large change in pedestrian MRT, because the resulting radiative exposure also depends on canopy visibility and radiation from other surrounding sources. The value of an LEB extension should therefore be assessed in terms of both its contribution to pedestrian radiation estimates and its ability to diagnose leaf thermal states and sensible–latent heat partitioning.

To overcome these limitations, this study develops SOLWEIG-LEB (Leaf Energy Balance) v1.0, hereafter referred to as SOLWEIG-LEB, an extension that integrates LAD-based path-dependent canopy attenuation and a voxel-scale leaf energy balance into the existing SOLWEIG framework. Its contribution lies in the integration and evaluation of these processes within SOLWEIG, rather than in introducing canopy attenuation or leaf energy balance as new physical concepts. By integrating voxel-resolved LAD information into the 2.5D SOLWEIG framework, the model captures fine-scale canopy attenuation physics while retaining the underlying building and ground geometry of the original radiation model. The objectives of this study are fourfold. First, we develop an LAD-based attenuation scheme that uses the leaf projection function and cumulative leaf area along radiative paths to represent spatial and temporal variations in canopy shortwave transmissivity. Second, we integrate a voxel-scale leaf energy balance that accounts for absorbed radiation, leaf thermal emission, sensible heat exchange, and transpiration to diagnose leaf temperature, vegetation longwave emission, and sensible and latent heat fluxes. Third, we evaluate leaf temperature, photosynthetically active radiation (PAR), transpiration, and MRT against observations in Angers, France, with additional leaf-temperature validation in Mainz, Germany, and we evaluate the integrated pedestrian-level radiative environment against six-directional radiation fluxes and MRT observations in Göteborg, Sweden. Finally, we distinguish the contributions of LAD-based attenuation and leaf-energy-balance-driven vegetation emission to pedestrian-level radiation and MRT, and examine the additional information provided by voxel-scale leaf temperature and energy-partitioning diagnostics. The remainder of this paper is organized as follows. Section 2 describes the mathematical formulation and computational framework of SOLWEIG-LEB v1.0, including the LAD-based canopy attenuation scheme, directional radiation modifications, and the leaf energy balance module. Section 3 presents the observational datasets and numerical experimental designs for the Angers and Göteborg sites. Section 4 presents the model evaluation results, comparative performance against Legacy SOLWEIG, and voxel-scale spatial diagnostics. Section 5 discusses the physical interpretations, computational scope, limitations, and future development, and Section 6 summarizes the main conclusions.

2. Model description

This section describes the mathematical formulation, computational framework, and implementation of SOLWEIG-LEB. Figure 1 illustrates the overall computational framework. The model extends the radiation-geometry framework of Legacy SOLWEIG and comprises input data processing, shadow and view-factor calculations, shortwave and longwave radiation-field calculations, a leaf energy balance module, and the final MRT calculation.

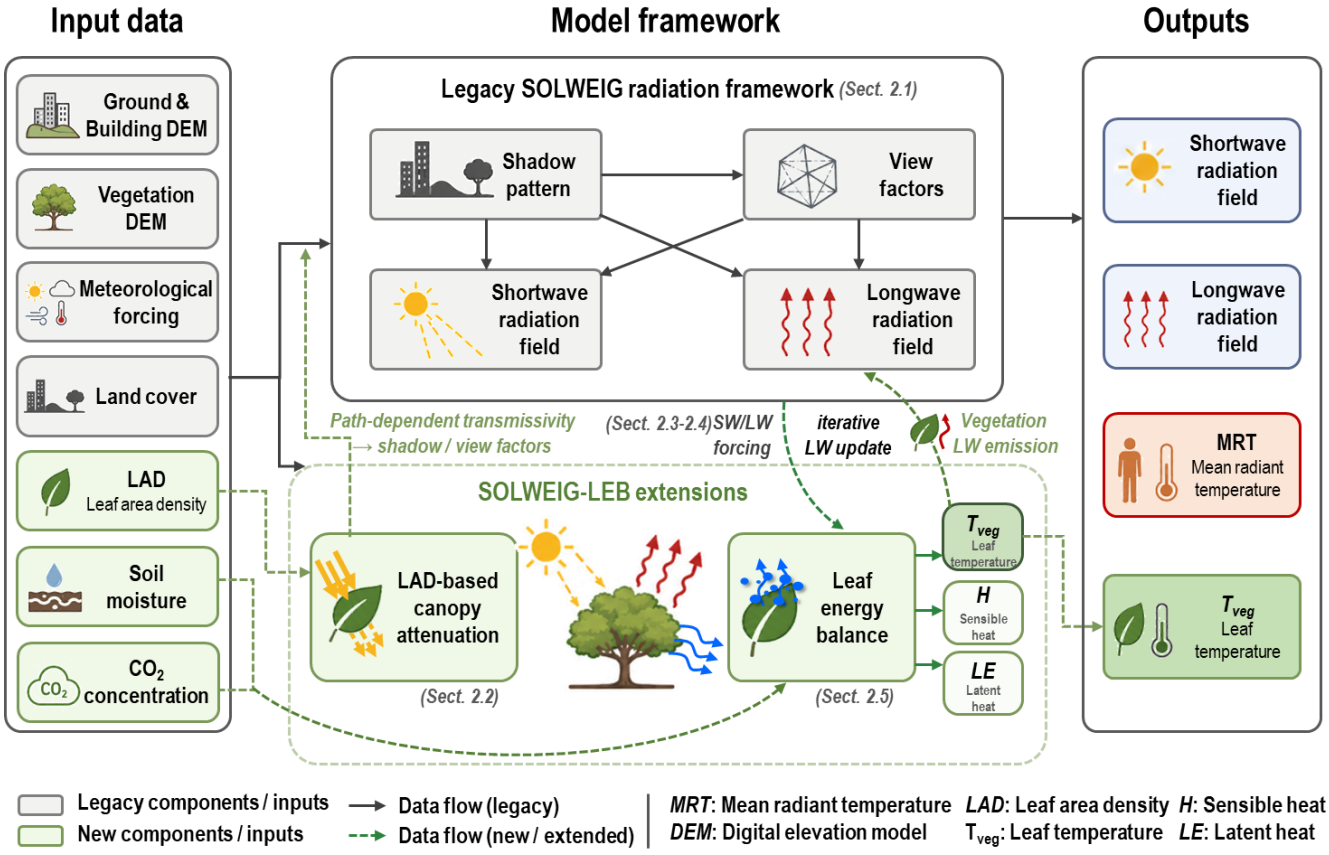

Figure 1. Schematic workflow of SOLWEIG-LEB v1.0. Grey components represent the Legacy SOLWEIG radiation framework, while green components indicate the newly introduced LAD-based canopy attenuation and leaf energy balance modules.

2.1. Legacy SOLWEIG radiation framework and MRT calculation

Throughout this study, Legacy SOLWEIG refers to the QGIS-based SOLWEIG v2025a. It calculates the six-directional radiative environment using terrain, building, and vegetation height data, land-cover information, and meteorological forcing. Specifically, SOLWEIG calculates shadow patterns produced by buildings and vegetation, sky view factors (SVF), ground view factors (GVF), reflected shortwave radiation, and longwave radiation at the pedestrian level. The final target variable of SOLWEIG, mean radiant temperature (MRT), is derived from the mean radiant flux density, which integrates the shortwave and longwave radiation fluxes received by a pedestrian from six orthogonal directions (upward, downward, east, south, west, and north). The mean radiant flux density (R) is defined as follows:

$$R = a_k \sum_{i=1}^{6} K_i F_i + \varepsilon_p \sum_{i=1}^{6} L_i F_i, \quad (1)$$

where i indexes these six directions, and K_i and L_i are the shortwave and longwave radiation fluxes incident on the human body from direction i, respectively. F_i represents the angular factor between the human body and the surrounding environment. For a standing or walking person, Legacy SOLWEIG uses an angular factor of 0.22 for each of the four horizontal directions and 0.06 for the upward and downward directions, following Lindberg and Grimmond (2011). a_k and ε_p are the shortwave absorption coefficient and longwave emissivity of the human body, set to 0.70 and 0.95, respectively, in this study (Table 1). MRT (T_{mrt}) is then calculated using the Stefan–Boltzmann law as

$$T_{mrt} = \sqrt[4]{\frac{R}{\varepsilon_p \sigma}} - 273.15, \quad (2)$$

where σ is the Stefan–Boltzmann constant (=5.67×10^{-8} W m^{-2} K^{-4}). Eqs. (1) and (2) are retained in SOLWEIG-LEB. Thus, the objective of this study is not to modify the MRT formulation itself, but to provide a more physically based and spatially explicit calculation of the vegetation-related K_i and L_i terms used in Eq. (1).

Table 1. Model configuration and vegetation treatment in Legacy SOLWEIG and SOLWEIG-LEB.

Model setting	Legacy SOLWEIG (v2025a)	SOLWEIG-LEB
Canopy transmissivity	Fixed transmissivity: τ = 3 % (Göteborg); τ = 30 % (A region) and 40 % (B region) (Angers)	Path-dependent transmissivity calculated from LAD, radiative path length, and the leaf projection function
Leaf projection function	Not explicitly represented	Spherical leaf angle distribution (G_{proj} = 0.5)
Vegetation temperature	$T_{veg} = T_{air}$	Calculated for each vegetation voxel using the leaf energy balance
Vegetation longwave emission	Calculated using $T_{veg} = T_{air}$	Calculated using vegetation-voxel T_{veg}
Sensible and latent heat fluxes	Not calculated	Calculated diagnostically for each vegetation voxel
Human-body representation	Six-directional box representation*	
Human posture	Standing	
MRT calculation height	1.1 m (Göteborg); 0.4 m (Angers)	
Human shortwave absorptivity	0.70	
Human longwave emissivity	0.95	
Diffuse shortwave sky model	Anisotropic (Wallenberg et al., 2020)	
Longwave radiation model	Anisotropic directional parameterization (Wallenberg et al., 2023)	

Model setting	Legacy SOLWEIG (v2025a)	SOLWEIG-LEB
Wall surface-temperature scheme	Göteborg: simple step-heating approach (Wallenberg et al., 2026); Angers: site-fitted daytime/nighttime empirical temperatures (Lindberg et al., 2008)	
Land-cover scheme	Enabled (Lindberg et al., 2016)	

* The six-directional box representation was used to match the radiation observations in Göteborg.

The vegetation module in Legacy SOLWEIG represents the three-dimensional structure of trees and shrubs by distinguishing between canopy top height and trunk-zone height. This structure distinguishes between the canopy region that casts shadows and the non-vegetated space below the canopy through which solar radiation can pass. However, in the legacy vegetation module, shortwave attenuation by vegetation is not calculated directly from the leaf area distribution within the canopy or from radiative path length. Instead, vegetation shadows are first calculated as a Boolean shadow field that represents only whether a pixel is sunlit (= 1) or shaded (= 0), and a single bulk representative transmissivity (τ), prescribed for specific vegetation types (typically set to 0.03 for dense summer crowns), is then uniformly applied during the shortwave radiation calculation. While computationally efficient, this approach cannot explicitly represent path-dependent shortwave attenuation that varies within the same tree canopy according to the canopy core, canopy edge, canopy gaps, and the direction of incoming solar radiation. Legacy SOLWEIG also simplifies the thermal state of vegetation in the longwave radiation calculation. In the legacy vegetation module, vegetation surface temperature (or leaf temperature) is assumed to be equal to ambient air temperature, and longwave radiation emitted from vegetation is calculated based on this isothermal air-temperature assumption. This approach can be a practical simplification for efficient MRT-oriented radiation modelling, but it does not directly resolve temporal variations in leaf temperature, temperature differences between sunlit and shaded foliage within the canopy, transpirational cooling, stomatal responses to microclimatic stress, or sensible and latent heat fluxes between vegetation and the atmosphere.

SOLWEIG-LEB retains the efficient radiation-geometry framework of Legacy SOLWEIG, while extending the vegetation-related radiation terms in two ways. First, instead of using a fixed representative transmissivity (τ), SOLWEIG-LEB computes the shortwave radiation fluxes (K_i) reaching a pedestrian or vegetation voxel using a path-dependent transmissivity determined from the canopy LAD and the radiative path length. Second, for the vegetation-related longwave radiation fluxes (L_i), the vegetation emission is explicitly driven by the leaf temperature (T_{veg}) calculated from the leaf energy balance module, thereby replacing the conventional air-temperature-based assumption.

2.2. LAD-based canopy attenuation

In Legacy SOLWEIG, shortwave radiation fluxes are divided into direct, diffuse, and reflected shortwave components. Because direct shortwave radiation has a single direction determined by the solar position, its obstruction is calculated using building and vegetation shadow factors. In contrast, diffuse shortwave radiation originates from the sky hemisphere and is therefore controlled by SVF, whereas reflected shortwave radiation is calculated using view factors of surrounding surfaces, such as the ground, walls, and vegetation, together with the wall sunlit/shaded fraction. Thus, in SOLWEIG, the effect of vegetation is represented through the shadow factor (S) for the direct component, and through geometry fields such as the sky view factor (Ψ_{sky}), ground view factor (Ψ_g), and directional angular weighting factor (w_{wall}) for the diffuse and reflected components.

SOLWEIG-LEB retains this existing structure but modifies the vegetation-related geometry fields to incorporate LAD-based transmissivity. Instead of applying a fixed representative vegetation transmissivity (τ) a posteriori, SOLWEIG-LEB calculates the optical depth along each directional ray during the shadow-casting or view-factor calculation and directly integrates the resulting path-dependent transmissivity into the geometry fields. Leaf area density (LAD), defined as the one-sided leaf area per unit canopy volume ($m^2\ m^{-3}$), determines the cumulative leaf area and optical depth along a radiative path through the canopy. When voxel-scale or vertically resolved LAD data are available, they can be used directly. When only leaf area index (LAI) is available, LAD is estimated by assuming a uniform vertical distribution of leaf area within the canopy layer:

$$LAD = \frac{LAI}{z_{top} - z_{base}}. \quad (3)$$

Here, LAI is the leaf area per unit ground area ($m^2\ m^{-2}$), and z_{top} and z_{base} denote the canopy-top height and crown-base (trunk-zone) height, respectively. Species-specific or observation-based LAD profiles can therefore be prescribed when available instead of applying the uniform-distribution assumption in Eq. (3). For a specific radiative path p passing through the canopy, the optical depth Ω_p accumulated along the path is calculated as:

$$\Omega_p = \int G_{proj} \cdot LAD(s)\ ds, \quad (4)$$

where $LAD(s)$ is the leaf area density ($m^2\ m^{-3}$) at position s along the radiative path. G_{proj} is the leaf projection function for the corresponding radiation direction and represents the fraction of leaf area projected onto a plane perpendicular to the incident ray. G_{proj} depends on the leaf angle distribution and the incident direction (Ross, 2012; Campbell, 1986). When the leaf angle distribution of the canopy is not explicitly known, a spherical leaf angle distribution can be assumed, for which $G_{proj} \approx 0.5$ (de Wit, 1965; Campbell and Norman, 2000). In the default configuration of this study, a spherical leaf angle distribution is assumed for all vegetation voxels, and $G_{proj} = 0.5$ is used.

The transmissivity τ_p of shortwave radiation along path p is then calculated using the Beer–Lambert law:

$$\tau_p = \exp(-\Omega_p). \quad (5)$$

Thus, τ_p varies with the accumulated optical depth along each radiative path, producing lower transmissivity through dense canopy cores and higher transmissivity near crown edges or canopy gaps. The Boolean vegetation shadow factor used in Legacy SOLWEIG is therefore replaced by a transmissivity-weighted vegetation shadow factor, S^*_{veg}:

$$S^*_{veg} = \begin{cases} 1, & \text{if the ray is blocked by buildings or intersects no vegetation} \\ \tau_p, & \text{if the ray intersects vegetation without being blocked by buildings} \end{cases}. \quad (6)$$

Here, S^*_{veg} is a continuous, attenuation-weighted vegetation shadow factor ranging between 0 and 1. Buildings are treated as opaque obstacles; therefore, the building shadow factor (S_{bd}) remains a Boolean variable as in Legacy SOLWEIG. The same integration concept is also applied to the calculation of SVF, GVF, and angular weighting factors. In this study, view-factor terms (Ψ^*) and directional angular weighting factors (w^*) with a superscript asterisk (*) do not indicate that a fixed transmissivity is multiplied a posteriori. Instead, they indicate that LAD-based canopy attenuation has already been dynamically incorporated during the shadow-casting or view-factor ray-tracing process. For example, $\Psi^*_{sky,veg}$, $\Psi^*_{g,sunlit}$, and w^*_{veg} denote the LAD-transmissivity-weighted quantities for canopy sky obstruction, sunlit-ground visibility, and directional vegetation contribution, respectively.

2.3. Modified shortwave radiation fluxes

In SOLWEIG, shortwave radiation fluxes consist of direct, diffuse, and reflected shortwave components (Lindberg et al., 2008; Lindberg and Grimmond, 2011). Direct shortwave radiation, I, is the direct solar irradiance on a plane perpendicular to the solar beam; diffuse shortwave radiation, D, is the sky diffuse component; and G is global shortwave radiation. In SOLWEIG, I is estimated from G and D as:

$$I = \frac{(G-D)}{\sin\eta}, \quad (7)$$

where η is the solar elevation angle.

SOLWEIG-LEB retains the shortwave radiation calculation structure of Legacy SOLWEIG but uses the transmissivity-weighted vegetation geometry terms defined in Section 2.2. Specifically, S^*_{veg} is applied to the direct component, whereas LAD-attenuation-weighted view factors, such as $\Psi^*_{sky,veg}$, are used for the diffuse and reflected components. The modified downward shortwave radiation, $K_\downarrow$, is expressed as:

$$\begin{aligned} K_\downarrow = \; & I \cdot [S_{bd} - (1 - S^*_{veg})] \sin\eta \\ & + D \cdot [\Psi_{sky,bd} - (1 - \Psi^*_{sky,veg})] \\ & + G \cdot \alpha_s \cdot (1 - f_s)[1 - \{\Psi_{sky,bd} - (1 - \Psi^*_{sky,veg})\}] \end{aligned}. \quad (8)$$

Here, S_{bd} is the direct-beam shadow factor for buildings, which is 0 when the point is shaded by buildings and 1 when it is not. S^*_{veg} is the transmissivity-weighted vegetation shadow factor defined in Eq. (6). $\Psi_{sky,bd}$ is the SVF considering building obstruction only, and $\Psi^*_{sky,veg}$ is the vegetation-related SVF including LAD-based canopy attenuation. α_s is the local surface albedo prescribed according to the surface category, and f_s is the fraction of wall surface that is shaded. The first, second, and third terms on the right-hand side of Eq. (8) represent the direct, diffuse, and reflected components, respectively.

The upward shortwave radiation, $K_{\uparrow}$, is calculated as shortwave radiation reflected from the ground surface and reaching a pedestrian or vegetation voxel:

$$K_{\uparrow} = \alpha_s \begin{bmatrix} I \cdot \Psi^*_{g,sunlit} \sin\eta \\ +D \cdot \{\Psi_{sky,bd} - (1 - \Psi^*_{sky,veg})\} \\ +G \cdot \alpha_s \cdot (1 - f_s)[1 - \{\Psi_{sky,bd} - (1 - \Psi^*_{sky,veg})\}] \end{bmatrix}. \quad (9)$$

Here, $\Psi^*_{g,sunlit}$ denotes the attenuation-weighted view factor of sunlit ground surfaces visible from the height of interest. In Legacy SOLWEIG, $K_{\uparrow}$ at pedestrian level is estimated by searching for sunlit areas around the pedestrian height of 1.1 m, with the horizontal search distance limited to 20 times the height of interest for computational efficiency (Lindberg and Grimmond, 2011). In SOLWEIG-LEB, the same principle is extended from pedestrian locations to all individual vegetation voxels. Thus, for each receiver height, the horizontal area corresponding to 20 times that specific height is searched to estimate the sunlit ground contribution, ensuring vertical profiling of reflected shortwave exposure.

The sideward shortwave radiation, $K_{\rightarrow,j}$, represents shortwave radiation incident from the four cardinal directions: east, south, west, and north, where $j \in \{E, S, W, N\}$. Each directional component is calculated separately depending on whether direct solar radiation contributes to that specific vertical plane. When direct solar radiation contributes to direction j, the sideward shortwave radiation is calculated as:

$$K_{\rightarrow,j} = \begin{array}{l} I \cdot \left[S_{bd} - \left(1 - S^*_{veg}\right)\right] \cos\eta \sin\theta_j \\ +D \cdot [1 - (w_{wall,j} + w^*_{veg,j})] \\ +G \cdot \alpha_s \cdot (1 - f_s)[w_{wall,j} + w^*_{veg,j}] \end{array}, \quad (10)$$

where θ_j is the solar azimuth angle relative to direction j. When direct solar radiation does not contribute to direction j, the direct component is excluded, and only the diffuse and reflected components are considered:

$$K_{\rightarrow,j} = \begin{array}{l} D \cdot [1 - (w_{wall,j} + w^*_{veg,j})] \\ +G \cdot \alpha_s \cdot (1 - f_s)[w_{wall,j} + w^*_{veg,j}] \end{array}. \quad (11)$$

Here, $w_{wall,j}$ and $w^*_{veg,j}$ are the attenuation-weighted angular weighting factors for building walls and vegetation visible from direction j, respectively. These weighting factors are utilized to quantify the contribution of shortwave radiation originating from direction j, encompassing secondary reflections from walls, vegetation, sky, and surrounding ground facets. Eqs. (8)–(11) are implemented not only for pedestrian-level MRT calculations but also as boundary conditions for the leaf

energy balance calculation in vegetation voxels. However, as described in Section 2.5, the shortwave radiation input to the leaf energy balance is not obtained by simply summing the entire six-directional shortwave radiation field into a single value. Instead, the direct, diffuse, and reflected components are partitioned and converted into absorbed radiation on an explicit leaf-area basis.

2.4. Modified longwave radiation fluxes and vegetation longwave emission

In SOLWEIG, longwave radiation fluxes (L) are calculated as the sum of longwave radiation emitted and reflected from the sky, buildings, surfaces, and vegetation. This calculation uses the SVF considering building obstruction only, $\Psi_{sky,bd}$, the vegetation-related SVF representing the obstruction of open sky by vegetation, $\Psi_{sky,veg}$, and an auxiliary view-factor term, $\Psi_{sky,veg-bd}$, used to isolate the vegetation layers located directly in front of building walls. In Legacy SOLWEIG, the vegetation surface temperature is assumed to be equal to air temperature, and the longwave contributions from vegetation and walls are calculated in a simplified manner (Lindberg and Grimmond, 2011). SOLWEIG-LEB retains the fundamental longwave radiation framework of the legacy model but dynamically updates the longwave radiation emitted from vegetation based on the diagnostic equilibrium leaf temperature, T_{veg}, calculated by the leaf energy balance module described in Section 2.5. The downward longwave radiation received by vegetation voxels in SOLWEIG-LEB, $L_{\downarrow}$, is formulated as:

$$\begin{aligned} L_{\downarrow} = \; & \{\Psi_{sky,bd} - \left(1 - \Psi^{*}_{sky,veg}\right)\} \cdot \varepsilon_{sky} \cdot \sigma \cdot T_{air}^{4} \\ & + \{\left(1 - \Psi^{*}_{sky,veg}\right) + \left(1 - \Psi^{*}_{sky,veg-bd}\right)\} \cdot \varepsilon_{veg} \cdot \sigma \cdot T_{veg}^{4} \\ & + \{(1 - \Psi_{sky,bd}) - \left(1 - \Psi^{*}_{sky,veg-bd}\right)\} \cdot \varepsilon_{wall} \cdot \sigma \cdot T_{wall}^{4} \\ & + [\{\left(1 - \Psi^{*}_{sky,veg}\right) + \left(1 - \Psi^{*}_{sky,veg-bd}\right)\}(1 - \varepsilon_{veg}) \\ & + \{(1 - \Psi_{sky,bd}) - \left(1 - \Psi^{*}_{sky,veg-bd}\right)\}(1 - \varepsilon_{wall})] \cdot \varepsilon_{sky} \cdot \sigma \cdot T_{air}^{4} \end{aligned} \quad . \qquad (12)$$

Here, ε_{sky}, ε_{veg}, and ε_{wall} are the emissivities of the sky, vegetation, and wall surfaces, respectively, in the vegetation-voxel radiation calculation. ε_{sky} is estimated empirically from air temperature and humidity, while ε_{veg} and ε_{wall} are prescribed as 0.98 and 0.90, respectively (Oke, 2002; Lindberg et al., 2008; Jones et al., 2003). T_{air}, T_{veg}, and T_{wall} represent the air temperature, leaf temperature, and building wall temperature, respectively, with all temperatures expressed in Kelvin (K). The first term on the right-hand side of Eq. (12) represents direct longwave radiation from the sky, the second term denotes the explicit vegetation longwave emission, the third term accounts for the longwave radiation emitted from wall surfaces not obscured by vegetation, and the fourth term captures the reflected sky longwave radiation from both vegetation and wall facets.

The upward longwave radiation received by a vegetation voxel, $L_{\uparrow}$, includes the longwave radiation emitted from the ground surface and the longwave radiation emitted from vegetation visible in the downward direction from the receiver height:

$$L_{\uparrow} = \begin{matrix} \left(1 - \Psi^{*}_{g,veg}\right) \varepsilon_g \cdot \sigma \cdot \{T_{air} + \Psi^{*}_{g,sunlit} \cdot (T_{sur} - T_{air})\}^4 \\ + \Psi^{*}_{g,veg} \cdot \varepsilon_{veg} \cdot \sigma \cdot T^4_{veg} \end{matrix} . \quad (13)$$

Here, ε_g is the ground emissivity prescribed for each land-cover category (Table 2). T_{sur} represents the surface temperature of sunlit ground, while shaded ground pixels are assumed to have the same temperature as T_{air}, as in Legacy SOLWEIG. $\Psi^{*}_{g,veg}$ is the view factor of vegetation canopy visible in the downward direction from the receiver. The sideward longwave radiation, $L_{\rightarrow,j}$, incident from the four cardinal directions (east, south, west, and north; $j \in \{\mathrm{E}, \mathrm{S}, \mathrm{W}, \mathrm{N}\}$), follows the multi-layered structure of Legacy SOLWEIG. At vegetation voxels, the vegetation-originating longwave radiation terms are explicitly driven by the diagnosed T_{veg} rather than the ambient air temperature, and the vegetation-related view-factors utilize the updated canopy geometry representation defined in Section 2.2. For these voxel-level radiation fields, the numerical integration follows Lindberg and Grimmond (2011), with the vegetation longwave source temperature updated from T_{air} to T_{veg}.

Table 2. Surface radiative properties used in the Göteborg simulations.

Surface category	Albedo	Emissivity
Dark asphalt	0.18	0.95
Roofs	0.18	0.95
Unmanaged grass	0.16	0.94
Walls	0.20	0.90
Bare soil	0.25	0.94

2.5. Leaf energy balance module

In SOLWEIG-LEB, leaf temperature (T_{veg}) is calculated by solving a steady-state energy balance for each vegetation voxel. The module adopts the CANOAK leaf energy balance framework (Baldocchi, 1992, 1994; Baldocchi and Harley, 1995). Absorbed radiation is partitioned into longwave emission, sensible heat flux, and latent heat flux. All terms are expressed per unit one-sided leaf area. Longwave emission and sensible heat exchange include both leaf surfaces, whereas transpiration occurs from one surface under the hypostomatous broadleaf assumption. The leaf energy balance is expressed as:

$$\begin{aligned} R_{net} &= Q_{rad,in} - L_{emit} \\ &= K_{abs} + L_{abs} - 2\varepsilon_{veg}\sigma T^4_{veg}. \\ &= H + LE \end{aligned} \quad (14)$$

Here, $Q_{rad,in}$ is the total radiative energy absorbed by the leaf ($Q_{rad,in} = K_{abs} + L_{abs}$), where K_{abs} and L_{abs} represent the absorbed shortwave and longwave radiation, respectively. L_{emit} ($= 2\varepsilon_{veg}\sigma T^4_{veg}$) accounts for the longwave radiation emitted

from both sides of the leaf. H is the sensible heat flux between the leaf and the surrounding air, and LE is the latent heat flux governed by transpirational cooling. The shortwave radiation input to the leaf energy balance is derived from the shortwave radiation fields calculated in Section 2.3. The leaf projection function G_{proj}, defined in Section 2.2, is applied strictly to the direct shortwave component. Thus, the shortwave radiation absorbed by leaves within a vegetation voxel (K_{abs}) is calculated as:

$$K_{abs} = \quad (G_{proj} \cdot K_{dir} + K_{dif} + K_{ref}) \cdot (\alpha_{PAR} \cdot f_{PAR} + \alpha_{NIR} \cdot f_{NIR}). \tag{15}$$

Here, K_{dir} is the direct shortwave radiation component reaching the vegetation voxel, and $G_{proj}K_{dir}$ represents the amount of direct solar beam incident on a unit leaf area. K_{dif} and K_{ref} are the diffuse and reflected shortwave radiation components reaching the vegetation voxel, respectively; these components are not scaled by G_{proj} because they lack a single beam direction. In Eq. (15), α_{PAR} and α_{NIR} are the leaf absorptivities for photosynthetically active radiation (PAR, 400–700 nm) and near-infrared radiation (NIR), respectively, while f_{PAR} and f_{NIR} represent the respective spectral fractions of broadband shortwave radiation. PAR is directly utilized for photosynthesis, whereas NIR contributes primarily to the leaf thermal load. Following the CANOAK configuration, α_{PAR}, α_{NIR}, f_{PAR}, and f_{NIR} are prescribed as 0.795, 0.31, 0.45, and 0.55, respectively. The longwave radiation absorbed by leaves is calculated using the total incoming longwave radiation for the vegetation voxel, L_{total}, calculated in Section 2.4:

$$L_{abs} = \quad \alpha_{LW} \cdot L_{total}, \tag{16}$$

where α_{LW} is the longwave absorptivity of the leaf. Assuming leaves to be gray bodies in the thermal infrared region and applying Kirchhoff's law, the longwave absorptivity can be considered equal to the longwave emissivity. Therefore, for leaf absorption and emission, $\alpha_{LW} = \varepsilon_{veg} = 0.98$ is used.

The sensible heat flux from leaves, H, is treated as heat exchange from both leaf sides:

$$H = 2\rho_{air} c_p \frac{T_{veg} - T_{air}}{r_{b,heat}}. \tag{17}$$

Here, ρ_{air} is air density, c_p is the specific heat capacity of air at constant pressure, and $r_{b,heat}$ is the leaf boundary-layer resistance for heat transfer. The factor of 2 represents the two-sided leaf assumption for sensible heat exchange.

The latent heat flux, LE, is treated as one-sided transpiration under the broadleaf hypostomatous assumption:

$$LE = \frac{0.622 \cdot \rho_{air} \cdot \lambda_{vap}}{P \cdot (r_{b,vap} + r_{stom})} \cdot \{e_s(T_{veg}) - e_{air}\}. \tag{18}$$

Here, λ_{vap} is the latent heat of vaporization, P is atmospheric pressure, and $r_{b,vap}$ is the leaf boundary-layer resistance for water-vapor transfer, and r_{stom} is the stomatal resistance to water-vapor diffusion. $e_s(T_{veg})$ is the saturation vapor pressure at leaf temperature, and e_{air} is the vapor pressure of the surrounding air. The leaf boundary-layer resistance for water-vapor

transfer ($r_{b,vap}$) is calculated from wind speed, leaf characteristic length, air viscosity, and the leaf–air temperature difference, accounting for both forced and free convection. In contrast, the stomatal resistance (r_{stom}) represents physiological regulation driven by coupled photosynthesis, leaf-surface humidity and CO_2 diffusion; increasing PAR generally promotes stomatal opening such that r_{stom} decreases, whereas under very low radiation conditions, the stomata approach a closed state and r_{stom} becomes large. The boundary-layer resistances ($r_{b,heat}, r_{b,vap}$) in Eqs. (17) and (18) are expressed as

$$r_{b,heat} = \frac{\ell}{D_h N_u}, \tag{19}$$

$$r_{b,vap} = \frac{\ell}{D_v S_h}, \tag{20}$$

where ℓ is the characteristic leaf dimension (set to 0.1 m), and D_h and D_v are the thermal and water-vapor diffusivities, respectively. The dimensionless Nusselt (N_u) and Sherwood (S_h) numbers characterize convective heat and water-vapor transfers across the leaf boundary layer. Leaves are approximated as flat plates, with boundary-layer resistances calculated using forced- and free-convection correlations implemented in CANOAK (Schuepp, 1993; Baldocchi and Bowling, 2003). The stomatal resistance in Eq. (18) is obtained from the water-vapour stomatal conductance:

$$r_{stom} = \frac{1}{g_{s,w} V_m}, \tag{21}$$

Here, $g_{s,w}$ is stomatal conductance to water vapor (mol m^{-2} s^{-1}), and V_m is the molar volume of air (m^3 mol^{-1}) at leaf temperature and ambient pressure, giving r_{stom} in s m^{-1}. For positive assimilation, $g_{s,w}$ follows the Ball–Berry relation used by Baldocchi (1994):

$$g_{s,w} = g_0 + m_{eff} \frac{A\, h_s}{C_s}, \tag{22}$$

where g_0 is residual conductance, m_{eff} is the effective conductance slope, A is net CO_2 assimilation rate (μmol m^{-2} s^{-1}), h_s is leaf-surface relative humidity (0–1), and C_s is leaf-surface CO_2 mole fraction (μmol mol^{-1}). Assimilation and stomatal conductance are coupled through the CANOAK C3 photosynthesis formulation (Farquhar et al., 1980; Baldocchi, 1994). The physiological parameters and photosynthesis equations are presented in Appendix A. Soil-water limitation is represented by scaling the Ball–Berry slope following Baldocchi (1997):

$$m_{eff} = m_0 f_w, \tag{23}$$

where m_0 is the slope under non-limiting soil-water conditions and f_w is a water-availability factor. We calculate f_w from relative extractable water (*REW*) by adapting the linear soil-water response of Granier et al. (1999):

$$f_w = min(1, \frac{REW}{REW_{crit}}), \tag{24}$$

where REW_{crit} = 0.4. REW is prescribed directly or calculated as $REW = \min[1, \max(0, \frac{\theta - \theta_{wilt}}{\theta_{fc} - \theta_{wilt}})]$, where θ, θ_{wilt}, and θ_{fc} are the root-zone volumetric soil water content, wilting-point water content, and field capacity ($m^3\ m^{-3}$), respectively.

Solving Eq. (14) yields T_{veg}, H, and LE for each vegetation voxel. The diagnosed leaf temperature is used to update vegetation longwave emission and the surrounding longwave radiation field. Leaf temperature and radiation are updated iteratively using a temperature-change criterion of 0.05 K.

3. Evaluation data and experimental design

Three observational datasets were used for complementary evaluations of SOLWEIG-LEB. Leaf-temperature (T_{veg}), PAR, transpiration, and MRT observations from Angers, France, were used to evaluate the leaf energy balance module and canopy radiation scheme and their ability to reproduce temporal variations, whereas six-directional radiation and MRT observations from Göteborg, Sweden, were used to evaluate the integrated pedestrian-level radiation framework, including LAD-based canopy attenuation and leaf-temperature-based vegetation longwave emission. Additional leaf-temperature observations from Mainz, Germany, were used for validation under contrasting sky conditions (Appendix B). In addition, a computational benchmark was conducted to quantify the additional computational cost associated with the newly introduced model components (Section 3.3).

3.1. Vegetation and radiative-environment evaluation dataset in Angers

Observations from a reduced-scale street-canyon experiment in Angers, France (Herpin et al., 2024), were used to evaluate within-canopy radiation attenuation, leaf temperature, transpiration, and MRT. The experimental site consisted of a north–south-oriented street canyon and building models on both sides, with a building height, building width, and canyon width of 2 m each (Fig. 2). Ornamental apple trees were present in regions A and B, whereas region C contained no trees (Fig. 2a). Following pruning, the canopy-top height was 1.70 m in both vegetated regions, and the canopy-base heights were 0.60 and 0.69 m in regions A and B, respectively. The corresponding LAI values were 2.49 and 1.91 $m^2\ m^{-2}$. LAD was assumed to be vertically uniform within the canopy (Figs. 2b and c).

MRT was estimated from globe temperatures measured at 0.4 m above ground in the centre of regions A, B, and C. Leaf temperatures were measured at western, central, and eastern positions within the canopies of regions A and B at 1.5 m above ground (Fig. 2d). PAR was measured within the canopy at heights of 1.1 and 1.5 m and above the canopy at 2.0 m (Fig. 2d). Leaf temperatures were measured using thermocouples attached to the undersides of leaves, and PAR was measured using Solems PAR/LE sensors. MRT was derived by applying a convective correction to temperatures measured using Pt100 sensors installed inside black globes with a diameter of 15 cm (Herpin et al., 2024).

Meteorological forcing consisted of air temperature, relative humidity, downward shortwave and longwave radiation, and wind speed. Radiation, air temperature, and relative humidity were observed in the non-vegetated region C, whereas wind speed was measured between regions B and C at 2 m above ground (Figs. 2e and f). Air temperature and relative humidity were measured using Vaisala HMP sensors, wind speed using an LCJ CV7 ultrasonic anemometer, and radiation using a Kipp & Zonen CNR radiometer (Herpin et al., 2024). Air temperature and wind speed observations at 2 m above ground were used, and direct and diffuse shortwave radiation were partitioned internally from the input global shortwave radiation. Air temperature, relative humidity, and wind speed were applied uniformly across the domain. The evaluation covered seven days from 29 July to 4 August 2020, with simulations performed at 30 min intervals (Fig. 3). Time is expressed in local standard time (LST, UTC+1).

The Legacy reference configuration retained the common non-vegetation settings while applying a fixed canopy transmissivity and prescribing vegetation temperature as $T_{\mathrm{veg}} = T_{\mathrm{air}}$. Representative transmissivity along a vertical path was calculated using the Beer–Lambert law as follows:

$$\tau = \exp(-G_{proj}\, LAI). \quad (25)$$

Applying $G_{\mathrm{proj}} = 0.5$ to the LAI values of regions A and B yielded vertical-path transmissivities of approximately 29 % and 38 %, respectively. Separate Legacy simulations were conducted using fixed transmissivities of 30 % and 40 %, which approximated these values. Results for regions A were compared with the 30 % simulation, whereas results for regions B and C were compared with the 40 % simulation. SOLWEIG-LEB used a spherical leaf angle distribution ($G_{\mathrm{proj}} = 0.5$) and LAD-based shortwave attenuation, and calculated the leaf energy balance using the CANOAK photosynthesis–stomatal coupling. The characteristic leaf dimension was set to 0.05 m, and the background CO_2 concentration was set to 420 ppm. The horizontal grid spacing was 0.2 m, and the vertical spacing of vegetation voxels was 0.1 m. The leaf energy balance was calculated during both daytime and nighttime, with leaf temperature and vegetation longwave emission updated iteratively. Solid-surface temperatures were calculated using daytime and nighttime empirical equations calibrated against site observations. Wall albedo and emissivity were set to 0.40 and 0.87, respectively, and the corresponding ground values were 0.25 and 0.94. PAR was calculated by applying the model's PAR energy fraction f_{PAR} (= 0.45) to the downward shortwave radiation ($K_{\downarrow}$) at the receiver (Baldocchi, 1994; Harley and Baldocchi, 1995).

Transpiration was evaluated for two trees in region A (G and E) and one tree in region B (H). Herpin et al. (2024) used covers and mulch on the tree containers to minimize rainfall infiltration and soil evaporation, and estimated daily transpiration from soil-water depletion during periods without irrigation or drainage. Changes in soil water content were calculated from volumetric water content measured using two Decagon EC-5 sensors in each container, with a soil volume of 44.5 L per tree. Observed transpiration was estimated for the period from 06:00 to 20:30 LST. Modelled transpiration per tree (V_{tr}) was calculated by weighting voxel-scale latent heat fluxes by leaf area and integrating over the observation period.

Cumulative transpiration per tree (V_{tr}, L tree^{-1}) was calculated as the product of total leaf area per tree (A_{leaf}, m^2 tree^{-1}) and cumulative transpiration per unit leaf area (E_{leaf}, L m^{-2}).

$$\begin{aligned} V_{tr} &= A_{leaf} \cdot E_{leaf} \\ &= A_{leaf} \cdot \frac{10^3}{\rho_w} \int_{t_1}^{t_2} \frac{\overline{LE}(t)}{\lambda_{vap}(t)}\, dt \\ &= A_{leaf} \cdot \frac{10^3}{\rho_w} \int_{t_1}^{t_2} \frac{\sum LE_v(t) LAD_v V_v}{\lambda_{vap}(t) \sum LAD_v V_v}\, dt \end{aligned} \quad . \qquad (26)$$

Here, A_{leaf} was 2.59 and 2.02 m^2 in regions A and B, respectively (Herpin et al., 2024). The mean latent heat flux ($\overline{LE}$) was calculated as the leaf-area-weighted average of the latent heat flux per unit leaf area in each voxel (LE_v), using the total leaf area of the corresponding voxel ($= LAD_v \cdot V_v$) as the weight. LE_v, LAD_v, and V_v denote the latent heat flux per unit one-sided leaf area (W m^{-2}), leaf area density (m^2 m^{-3}), and volume (m^3) of voxel v, respectively. λ_{vap} is the latent heat of vaporization (J kg^{-1}), ρ_w is water density (kg m^{-3}), and 10^3 converts water volume from m^3 to L. The integration interval t_1–t_2 was 06:00–20:30 LST.

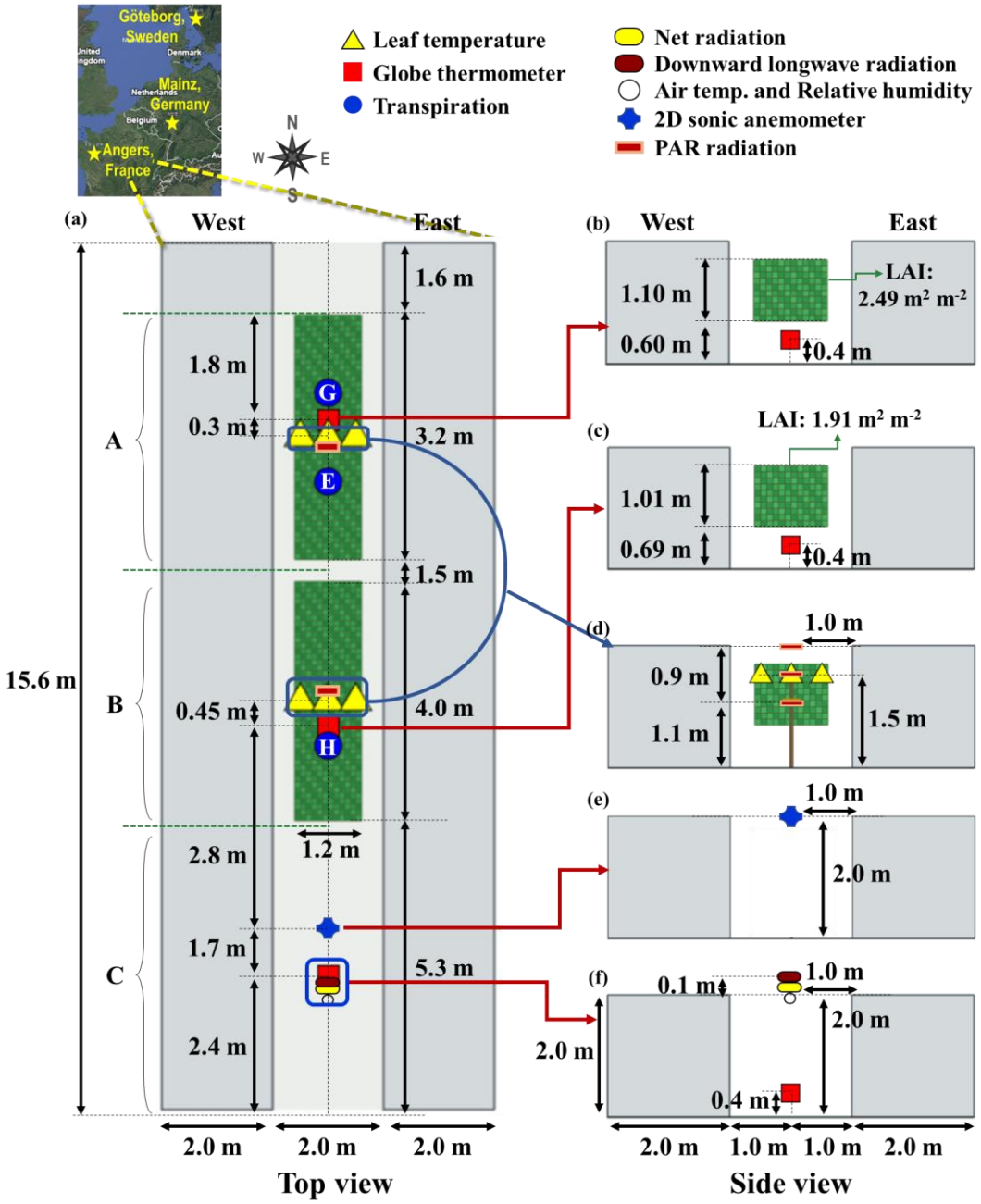

460 **Figure 2. Geometry and instrument layout of the reduced-scale street-canyon experiment in Angers, France, reconstructed based on Herpin et al. (2024). (a) Plan view of the experimental site and measurement locations. (b, c) Canopy geometry, leaf area index (LAI), and MRT measurement locations in regions A and B, respectively. (d) Leaf-temperature and photosynthetically active radiation (PAR) measurement locations in regions A and B. (e) Wind-speed measurement location. (f) Measurement locations for global shortwave radiation, downward longwave radiation, air temperature, relative humidity, and MRT.**

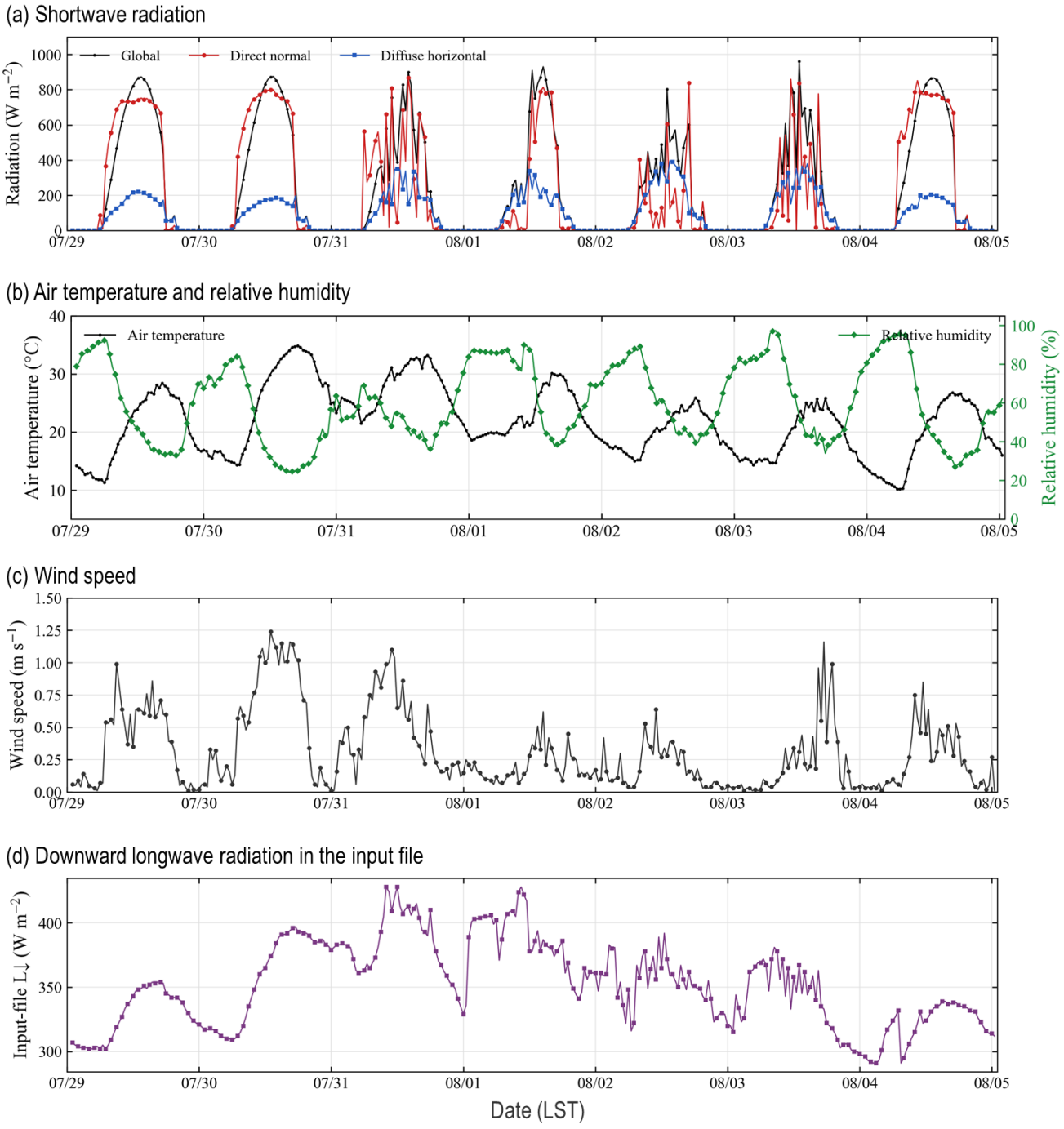

Figure 3. Meteorological forcing at 30 min intervals during the Angers evaluation period from 29 July to 4 August 2020. (a) Global shortwave radiation and its direct and diffuse components, (b) air temperature and relative humidity, (c) wind speed, and (d) downward longwave radiation.

3.2. Pedestrian-level radiation and MRT evaluation dataset in Sweden

The pedestrian-level radiative environment and MRT calculated by SOLWEIG-LEB were evaluated using six-directional radiation observations from Göteborg, Sweden (57°41'22.0"N, 11°58'01.0"E) (Lindberg and Grimmond, 2011; Konarska et al., 2014). The study site is a public square surrounded by two- to three-storey buildings, with a park containing deciduous trees and shrubs to the northwest (Fig. 4a). Shortwave and longwave radiation fluxes were measured in six directions—upward, downward, east, south, west, and north—using CNR1 net radiometers (Kipp & Zonen). For the present study, the two measurement locations were denoted OP1 and OP2 (Fig. 4b). OP1 was located beneath an approximately 13.5-m-high *Aesculus hippocastanum* canopy, whereas OP2 was located north of a row of *Tilia cordata* trees approximately 16.6 m in height. Both locations were therefore strongly influenced by tree-canopy shading. Measurements were available for 23 May 2010 at OP1 and for 7, 10, and 12 July 2010 at OP2.

The model domain was configured to include the observation points and the surrounding buildings and vegetation, with horizontal and vertical spatial resolutions of 2 m and 1 m, respectively. In SOLWEIG-LEB, vegetation LAD or LAI values must be specified to execute the LAD-based canopy attenuation scheme. The LAD values reported in previous literature are approximately 0.6 $m^2\ m^{-3}$ for *Tilia cordata* (Scholz et al., 2018; Moser et al., 2015; Helletsgruber et al., 2020). In contrast, *Aesculus hippocastanum* has been reported to exhibit a broader range of approximately 0.2–0.7 $m^2\ m^{-3}$ (Lv et al., 2024; Moser-Reischl et al., 2025). Konarska et al. (2014) reported that the direct shortwave transmissivity beneath the foliated canopy of *Aesculus hippocastanum* at the study site was approximately 1.7 %. Using G_{proj} = 0.5, corresponding to a spherical leaf angle distribution, and the Beer-Lambert formulation in Eq. (25), the effective LAI (LAI_{eff}) corresponding to $\tau = 0.017$ is estimated as approximately 8.1 $m^2\ m^{-2}$. LAI_{eff} represents effective leaf area along the radiation path. Guided by the reported literature values, LAD was set to 0.6 $m^2\ m^{-3}$ at both OP1 and OP2, and the spatial LAI input was calculated accordingly (Fig. 4c).

In the evaluation using the Swedish dataset, the observed six-directional shortwave and longwave radiation fluxes and MRT were compared with the corresponding outputs from Legacy SOLWEIG v2025a and SOLWEIG-LEB. In both model configurations, a six-directional standing box at 1.1 m above ground was used to match the six-directional radiation observations (Lindberg et al., 2008). The cylindrical human-body representation is also available in SOLWEIG-LEB but was not used in the present evaluation because the observational dataset provides radiation fluxes in six orthogonal directions. An anisotropic diffuse shortwave sky model was applied following Wallenberg et al. (2020), while directional longwave radiation from the sky, vegetation, and sunlit and shaded building surfaces was calculated using the anisotropic longwave parameterization of Wallenberg et al. (2023). Wall surface temperatures were calculated using the simple step-heating approach proposed by Wallenberg et al. (2026). The common radiation-model settings and the differences in vegetation treatment between the two configurations are summarized in Table 1.

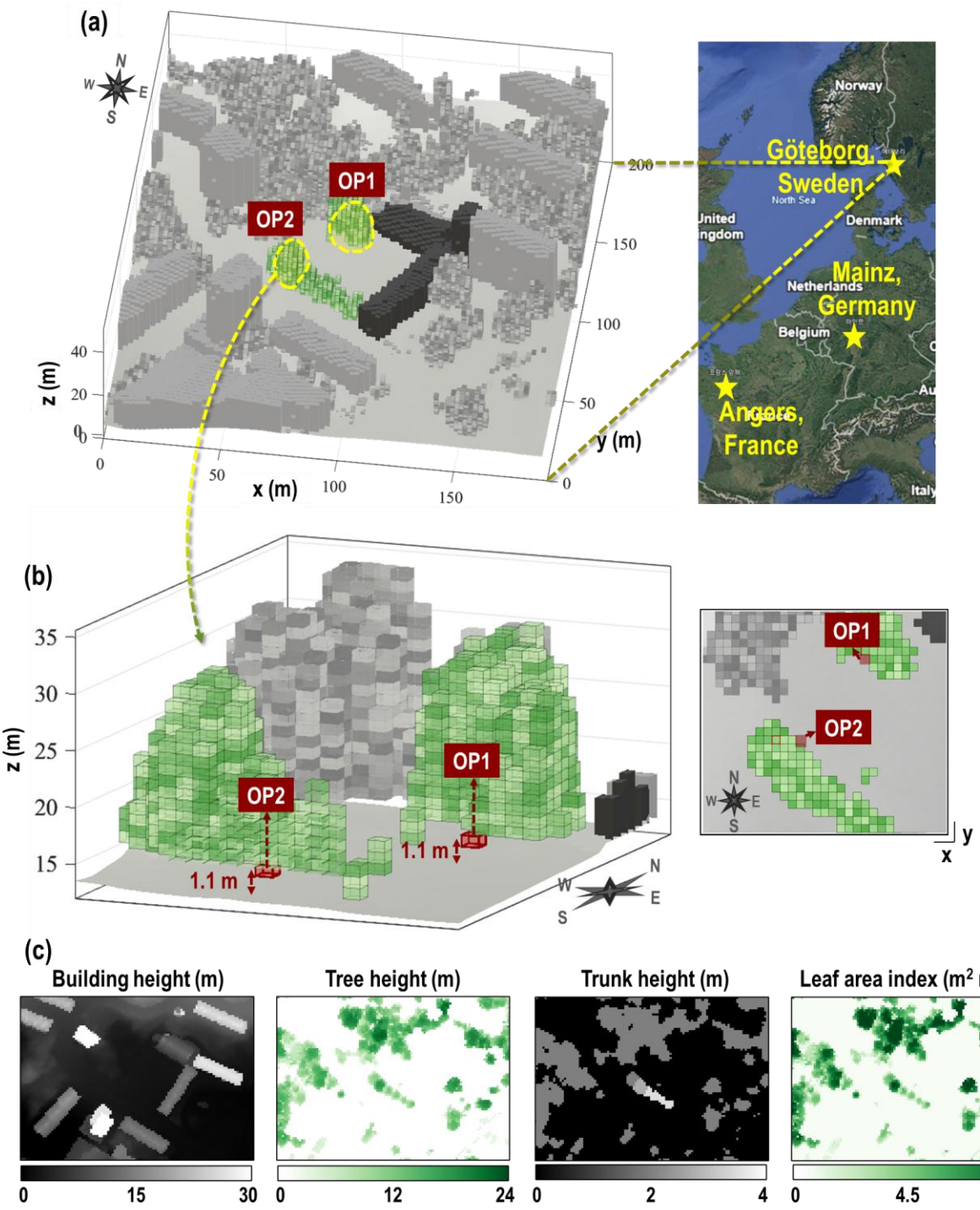

Figure 4. Göteborg site and model domain used for pedestrian-level radiation and MRT evaluation. (a) Site location and three-dimensional model domain, (b) locations and surrounding canopy geometry of OP1 and OP2, and (c) building height, tree height, trunk-zone height, and leaf area index used as model inputs.

To evaluate the combined effect of the newly introduced vegetation schemes, the two simulations differed only in canopy shortwave attenuation and vegetation thermal treatment. Legacy SOLWEIG used a fixed canopy transmissivity of 0.03 and assumed $T_{veg} = T_{air}$, whereas SOLWEIG-LEB used LAD-based path-dependent transmissivity and solved the leaf energy balance for each vegetation voxel to diagnose T_{veg} and vegetation longwave emission. The same site geometry, meteorological forcing (Fig. 5), and prescribed surface properties were used; the configuration files document the settings of the SOLWEIG-LEB runs. Ground-cover surface-temperature parameterization and radiative properties followed Lindberg et al. (2016), and the surface albedo and emissivity values are listed in Table 2. Non-limiting soil-water conditions (REW = 1 and f_w = 1) and a background CO2 concentration of 420 ppm were prescribed, as in the Mainz simulations.

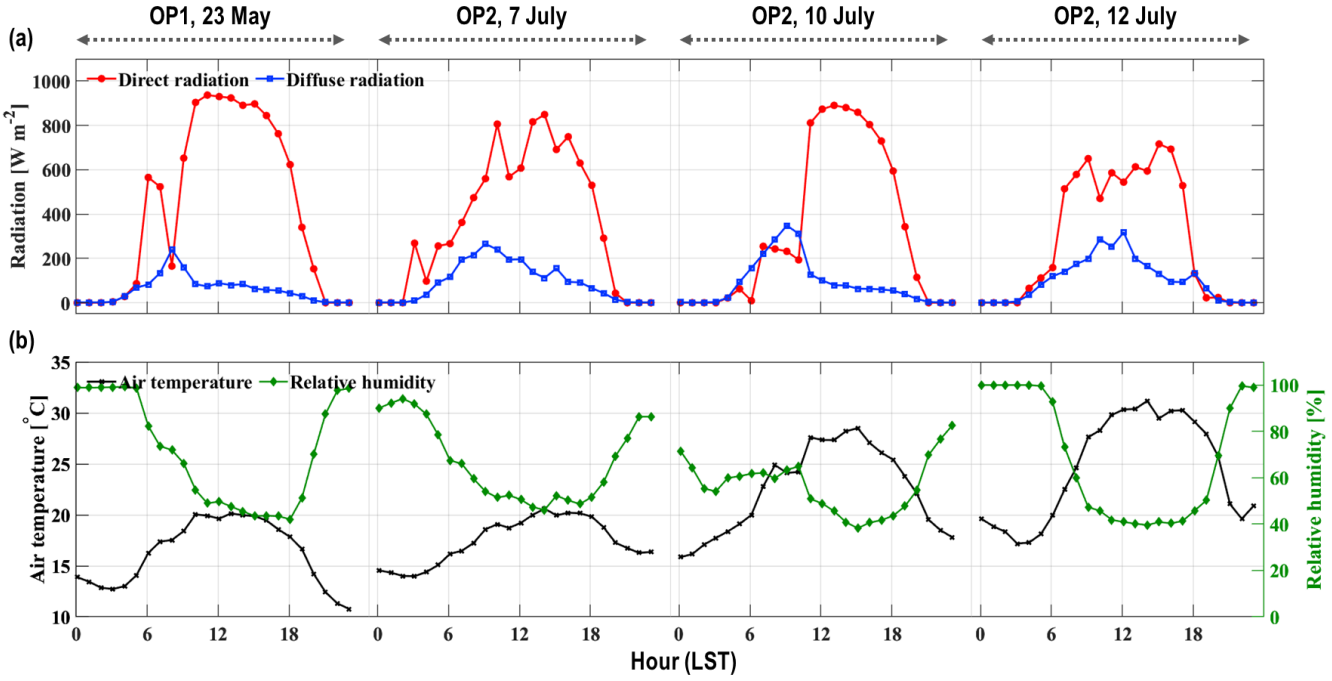

Figure 5. Meteorological forcing used for the Göteborg simulations at OP1 on 23 May 2010 and OP2 on 7, 10, and 12 July 2010. (a) Direct and diffuse shortwave radiation and (b) air temperature and relative humidity.

3.3. Computational benchmark setup

A key advantage of Legacy SOLWEIG is its high computational efficiency and relatively low runtime. SOLWEIG-LEB, however, introduces additional three-dimensional vegetation-voxel calculations for LAD-based canopy attenuation and an iterative leaf energy balance. The benchmark was therefore designed to quantify the computational overhead introduced by these new components and to assess how effectively a GPU-accelerated implementation offsets this additional cost. The benchmark domains were generated based on the spatial data used for the Göteborg evaluation. The horizontal resolution was fixed at 2 m, and the horizontal grid dimensions were systematically scaled from 50 × 50 to 100 × 100, 200 × 200, 300 × 300,

400 × 400, 500 × 500, and 600 × 600 grid cells. The larger domains were synthetic domains generated by spatially repeating the same urban morphology and therefore do not represent different real urban areas. The numbers of active vegetation voxels and wall-surface voxels were also quantified for each domain to characterize the scaling of the three-dimensional computational workload.

Four distinct numerical configurations (T1–T4) were compared to isolate and distinguish the computational costs associated with different model components. T1 represents the CPU-based QGIS implementation of Legacy SOLWEIG (v2025a). T2 performs the legacy-equivalent calculation of T1 re-implemented within the GPU framework. T3 activates LAD-based shortwave attenuation within the GPU framework, while T4 represents the full SOLWEIG-LEB configuration with both LAD-based attenuation and the vegetation-voxel leaf energy balance activated. Accordingly, the comparison between T1 and T2 represents the speedup achieved by the GPU-based legacy-equivalent implementation, the comparison between T2 and T3 quantifies the additional overhead of 3D ray-tracing and LAD-based attenuation, and the comparison between T3 and T4 quantifies the additional cost of the iterative leaf energy balance module. Identical terrain, building, vegetation, meteorological inputs, and output settings were enforced across all configurations.

Preprocessing time and per-timestep SOLWEIG runtime were measured separately. Preprocessing included the SVF calculation and wall preprocessing required for the wall-temperature scheme; for the LAD-enabled configurations (T3 and T4), the LAD-weighted vegetation SVF calculation was additionally included. The per-timestep runtime included input-data loading, radiation and thermal-environment calculations, and disk write-out of the common model outputs. The T1–T4 timestep simulations were repeated three times for each domain size, and the mean runtime and standard deviation were evaluated. For the GPU configurations, peak device-memory usage during model execution was also recorded. GPU runtimes were measured after a warm-up execution to eliminate CUDA context initialization overheads.

All benchmarks were performed on a Lenovo ThinkPad P16 Gen 3 equipped with an Intel Core Ultra 9 275HX CPU, 80 GB DDR5 RAM, and an NVIDIA RTX PRO 3000 Blackwell Generation Laptop GPU with 12,227 MiB of device memory. The GPU environment consisted of Python 3.12.9, CuPy 13.3.0, CUDA runtime 12.6, and 64-bit Windows 11.

3.4. Statistical metrics

Model performance was evaluated using the Pearson correlation coefficient (r), root mean square error (RMSE), range-normalized root mean square error (NRMSE), and mean bias error (MBE). These metrics quantify temporal agreement, error magnitude, relative error, and systematic bias, respectively. The Pearson correlation coefficient (r) was calculated as:

$$r = \frac{\sum_{i=1}^{N}(M_i-\bar{M})(O_i-\bar{O})}{\sqrt{\sum_{i=1}^{N}(M_i-\bar{M})^2}\sqrt{\sum_{i=1}^{N}(O_i-\bar{O})^2}}. \quad (27)$$

Here, M_i and O_i are the modelled and observed values for data point *i*, respectively, while $\bar{M}$ and $\bar{O}$ represent their corresponding mean values, and *N* is the total number of data points. The absolute magnitude of simulation error is quantified by RMSE, while NRMSE provides a relative error scale normalized by the range of observations:

$$RMSE = \sqrt{\frac{1}{N}\sum_{i=1}^{N}(M_i - O_i)^2}, \quad (28)$$

$$NRMSE = \frac{RMSE}{O_{max} - O_{min}}, \quad (29)$$

where O_{max} and O_{min} denote the maximum and minimum values for the observations, respectively. MBE was calculated as:

$$MBE = \frac{1}{N}\sum_{i=1}^{N}(M_i - O_i). \quad (30)$$

Positive and negative MBE values indicate model overestimation and underestimation, respectively. The same metrics were applied to leaf temperature, shortwave radiation, longwave radiation, MRT, PAR, and transpiration. MAE was calculated as the mean absolute difference between paired modelled and observed values.

4. Results

4.1. Model evaluation using observations from Angers

Observations from Angers were used to evaluate leaf temperature, transpiration, PAR, and MRT calculated by SOLWEIG-LEB. Figure 6 presents observed and simulated leaf temperatures at 1.5 m above ground in regions A and B. Observed leaf temperatures followed diurnal variations similar to those of the background air temperature but occasionally exceeded air temperature by more than 10 °C during daytime. These high leaf temperatures were particularly evident at the western observation point in region B. SOLWEIG-LEB reproduced the overall leaf-temperature variations associated with daytime heating and nighttime cooling and, unlike Legacy SOLWEIG, which assumes leaf temperature equals air temperature, calculated leaf temperatures above air temperature during daytime. However, its leaf-temperature performance varied among observation locations. High daytime leaf temperatures were underestimated at the eastern point in region A and the western point in region B, whereas overestimation occurred during some periods at the western point in region A. The correlation coefficient for temporal leaf-temperature variations increased relative to Legacy SOLWEIG at five observation points, with the central point in region A being the exception, whereas RMSE decreased at only three of the six points. These differences may also be associated with the different spatial scales represented by the observations and the model. The observations were obtained using thermocouples attached to individual leaves, whereas the model calculates a representative temperature for each vegetation voxel, limiting its ability to reproduce all temperature differences associated with the solar exposure and orientation of individual leaves.

When valid paired data from the three observation points were pooled within each region (Table 3), leaf-temperature RMSE decreased from 1.82 °C in Legacy SOLWEIG to 1.72 °C in SOLWEIG-LEB in region A, and from 2.19 to 1.61 °C in region B. The correlation coefficient (r) increased from 0.96 to 0.97 in region A and from 0.95 to 0.97 in region B. MBE also decreased from 0.36 to 0.09 °C and from 0.22 to −0.04 °C, respectively.

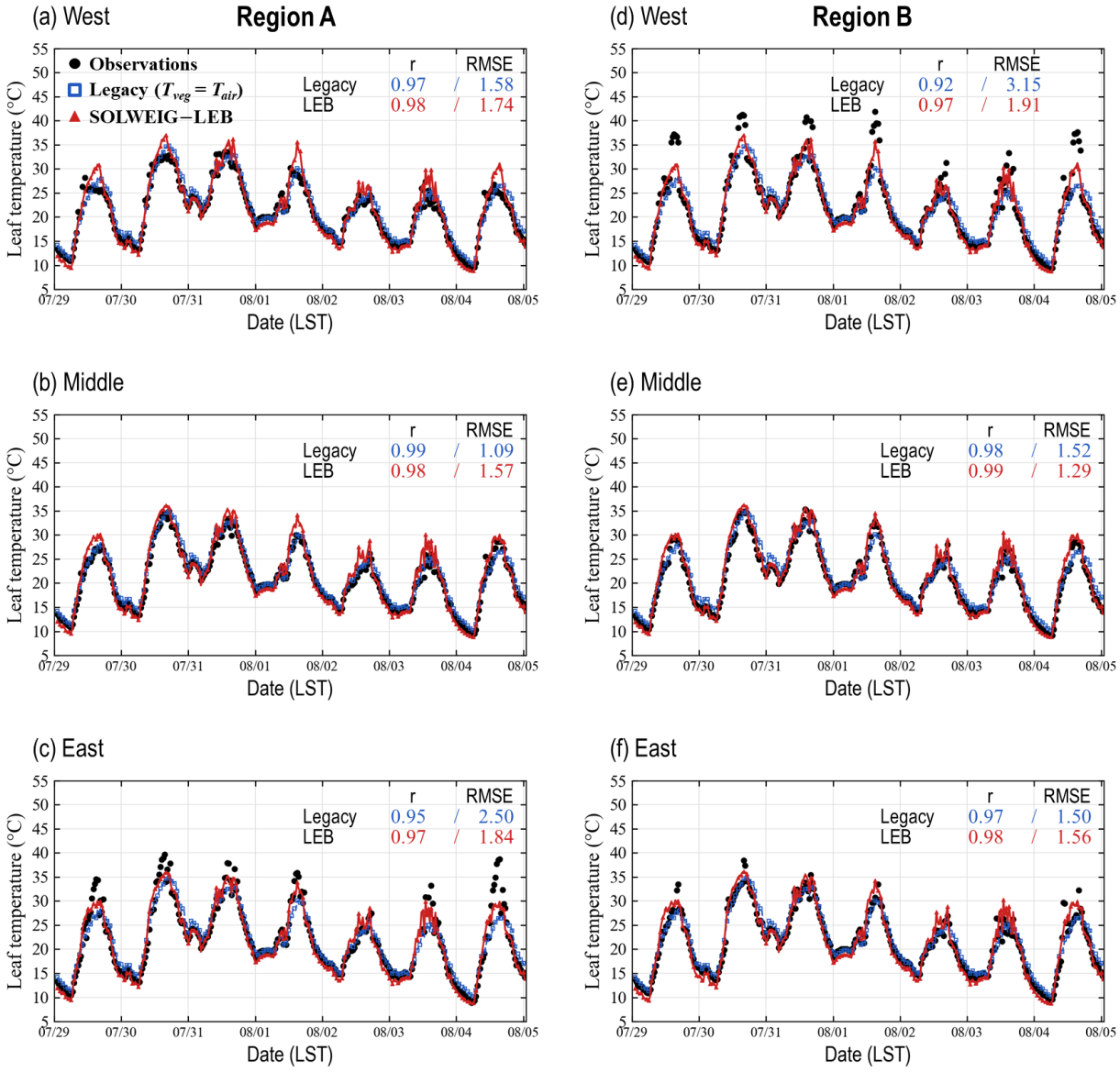

Figure 6. Comparison of observed and simulated leaf temperatures at 1.5 m above ground in vegetated regions A and B in Angers, France. The left column shows comparisons at the (a) western, (b) central, and (c) eastern observation points in region A, and the right column shows those at the (d) western, (e) central, and (f) eastern observation points in region B. Black circles indicate observations, blue open squares indicate Legacy SOLWEIG ($T_{veg} = T_{air}$), and red triangles indicate SOLWEIG-LEB.

Figure 7 compares MRT at 0.4 m above ground in vegetated regions A and B and non-vegetated region C. The MRT RMSEs of SOLWEIG-LEB were 2.32 and 2.20 °C in regions A and B, respectively, lower than the corresponding Legacy SOLWEIG values of 2.53 and 2.30 °C (Table 3). In region A, the mean bias also decreased from 0.77 to 0.39 °C. In region B, however, RMSE decreased slightly while MBE changed from -0.04 to -0.64 °C, indicating greater mean underestimation. Differences between the two models were particularly pronounced around noon, when the MRT overestimation in Legacy SOLWEIG was reduced in SOLWEIG-LEB. This is interpreted as a reduction in transmitted shortwave radiation resulting from the calculation of cumulative LAD-based attenuation along radiative paths in SOLWEIG-LEB, in contrast to the fixed canopy transmissivity used in Legacy SOLWEIG. In region C, where no trees were present, MRT differences between the two models were negligible.

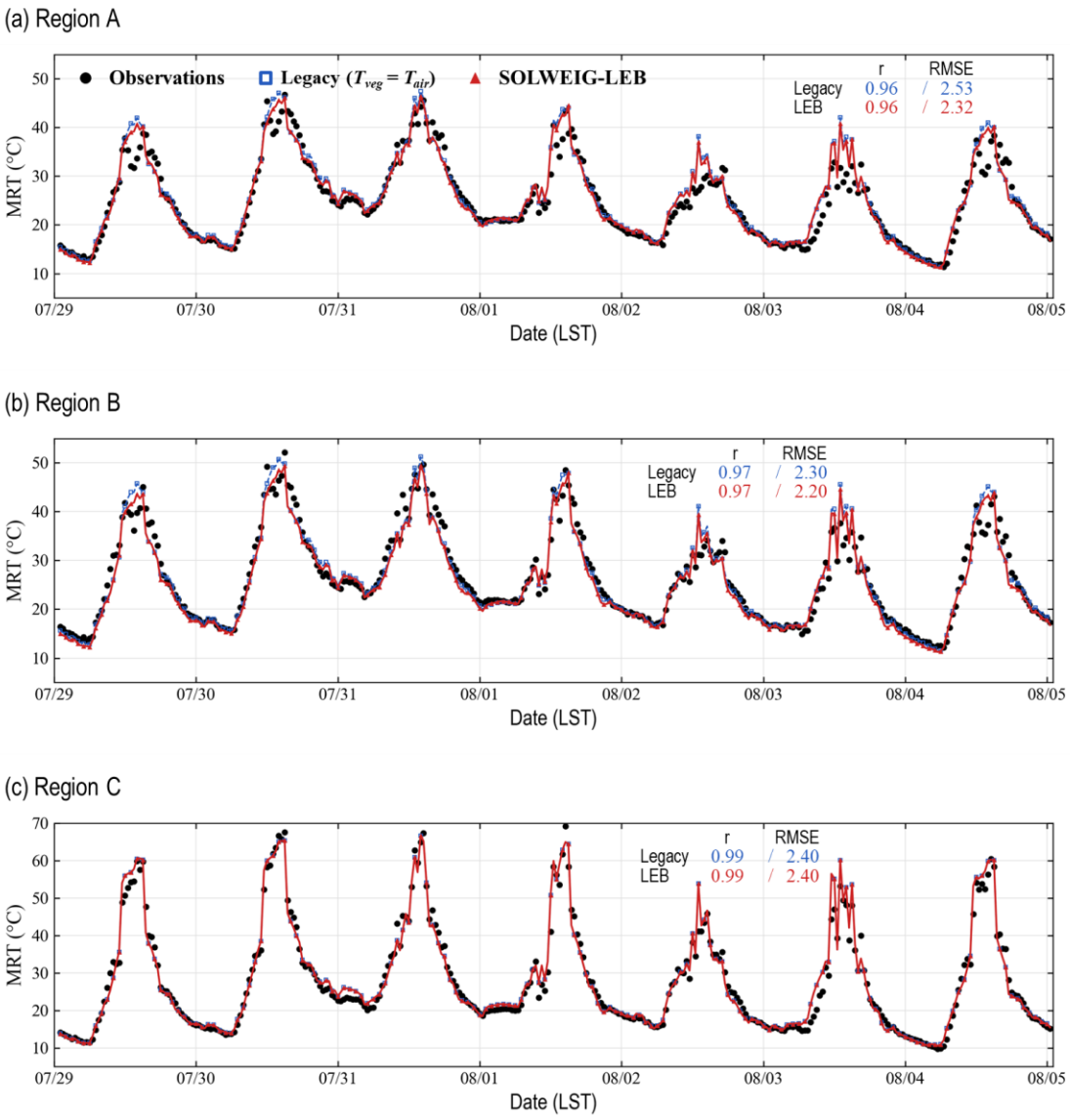

Figure 7. Comparison of observed and simulated mean radiant temperature (MRT) at 0.4 m above ground in vegetated regions A and B and non-vegetated region C in Angers, France. Panels show MRT time series for (a) region A, (b) region B, and (c) region C. Black circles indicate observations, blue open squares indicate Legacy SOLWEIG, and red triangles indicate SOLWEIG-LEB.

Table 3. Region-specific statistics for daytime and nighttime leaf temperature and MRT in Angers. Leaf-temperature statistics were calculated by pooling paired data from the three observation points within each region. RMSE and MBE are expressed in °C.

Region	Metric	Leaf temperature (°C)		MRT (°C)	
		Legacy	SOLWEIG-LEB	Legacy	SOLWEIG-LEB
A	*N*	1003	1003	336	336
	r	0.96	0.97	0.96	0.96

Region	Metric	Leaf temperature (°C)		MRT (°C)	
		Legacy	SOLWEIG-LEB	Legacy	SOLWEIG-LEB
	RMSE	1.82	1.72	2.53	2.32
	NRMSE	0.06	0.06	0.07	0.07
	MBE	0.36	0.09	0.77	0.39
B	*N*	1008	1008	336	336
	r	0.95	0.97	0.97	0.97
	RMSE	2.19	1.61	2.30	2.20
	NRMSE	0.07	0.05	0.06	0.06
	MBE	0.22	-0.04	-0.04	-0.64
C	*N*	–	–	336	336
	r	–	–	0.99	0.99
	RMSE	–	–	2.40	2.40
	NRMSE	–	–	0.04	0.04
	MBE	–	–	0.29	0.27

Figure 8 compares observed and simulated PAR at different heights in regions A and B in Angers. Observed PAR was high above the canopy and decreased toward lower levels within the canopy. SOLWEIG-LEB generally reproduced these diurnal variations and vertical attenuation. Correlation coefficients (r) at individual heights ranged from 0.81 to 0.99, and RMSEs ranged from 18.32 to 44.38 W m^{-2}. When valid paired data from the three heights were pooled within each region (Table 4), the correlation coefficients were 0.98 and 0.96 in regions A and B, respectively, and the corresponding RMSEs were 21.92 and 31.38 W m^{-2}. Errors were relatively larger in the lower canopy than at the upper levels. In particular, at 1.1 m in region B, the correlation coefficient decreased to 0.81 and RMSE was 44.38 W m^{-2}. These results indicate that SOLWEIG-LEB reproduced the overall PAR attenuation pattern, although relatively large errors remained in the local radiative environment of the lower canopy. These errors may be influenced by simplified model assumptions regarding actual canopy geometry, the spatial LAD distribution, and the leaf projection function (G_{proj}), as well as uncertainty in the leaf distribution around the measurement locations.

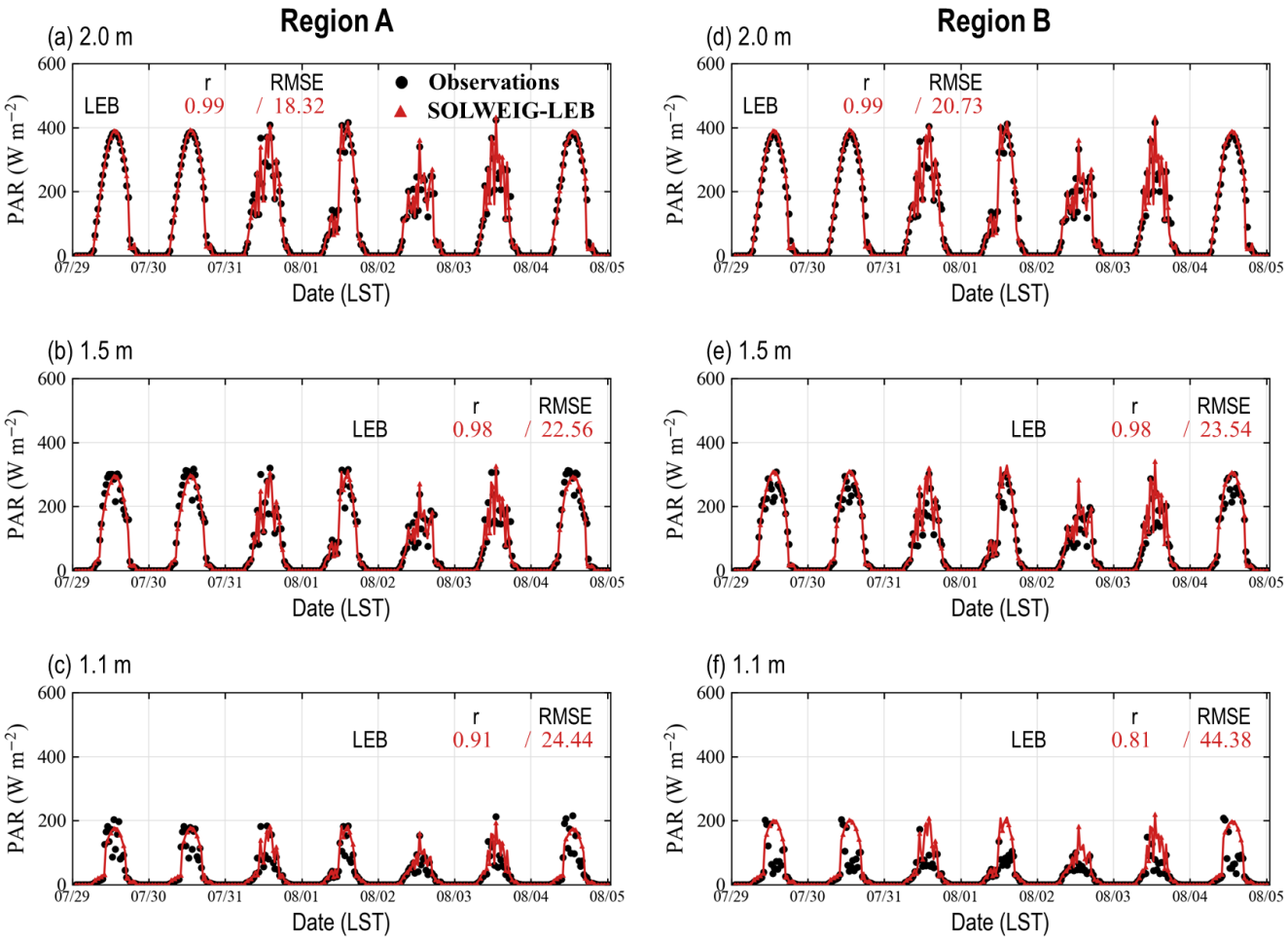

Figure 8. Comparison of observed photosynthetically active radiation (PAR) and SOLWEIG-LEB results at different heights in vegetated regions A and B in Angers, France. The left column shows PAR comparisons at heights of (a) 2.0 m, (b) 1.5 m, and (c) 1.1 m in region A, and the right column shows those at (d) 2.0 m, (e) 1.5 m, and (f) 1.1 m in region B. Black circles indicate observations, and red triangles indicate SOLWEIG-LEB.

Figure 9 compares observed daily transpiration and SOLWEIG-LEB results for two trees in region A (G and E) and one tree in region B (H) in Angers. SOLWEIG-LEB generally reproduced the overall magnitude and day-to-day variations in transpiration observed for the three trees. The correlation coefficients (r) for trees G, E, and H were 0.93, 0.94, and 0.71, respectively, and the corresponding RMSEs were 0.85, 0.28, and 0.26 L tree^{-1} (Table 4). In particular, simulated transpiration was relatively close to the observations for trees E and H, whereas transpiration for tree G was consistently overestimated despite reproducing its day-to-day variation.

Herpin et al. (2024) reported regional mean leaf areas rather than individual-tree leaf areas, with values of 2.59 ± 0.28 and 2.02 ± 0.31 m^2 tree^{-1} for regions A and B, respectively (mean ± standard error). Accordingly, transpiration was

calculated using the mean leaf area for each region, and the corresponding range of simulated transpiration based on the standard error of leaf area is also shown in Fig. 9. Overestimation persisted for tree G even when this range was considered, whereas observed and simulated transpiration were generally similar for trees E and H. These results indicate that SOLWEIG-LEB can generally reproduce the magnitude and day-to-day variations of tree transpiration, while highlighting the importance of leaf-area representativeness when evaluating transpiration for individual trees.

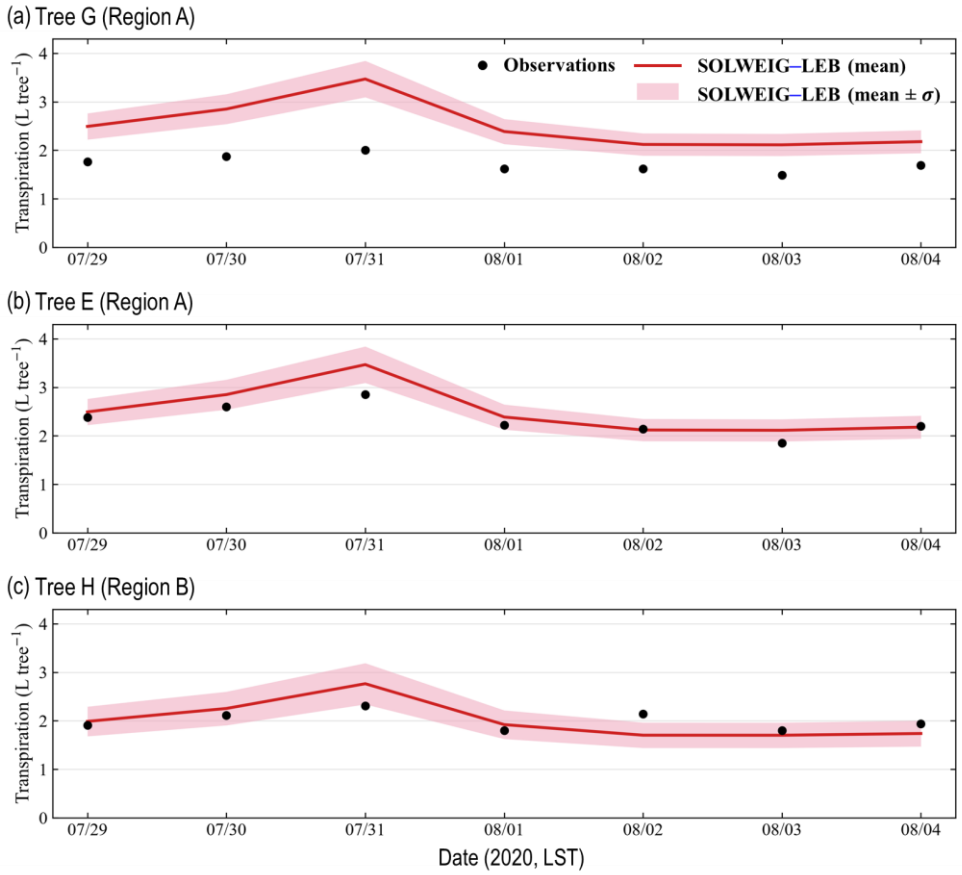

Figure 9. Comparison of observed daily transpiration per tree and SOLWEIG-LEB results in vegetated regions A and B in Angers, France. Panels show transpiration for (a) tree G in region A, (b) tree E in region A, and (c) tree H in region B. Black circles indicate observations, and red solid lines indicate SOLWEIG-LEB results calculated using the regional mean leaf area per tree. Pink shading indicates the transpiration range obtained by applying the mean leaf area ±1 standard error.

Table 4. Evaluation statistics for PAR and daily transpiration in Angers, France. Valid paired PAR data from three heights (1.1, 1.5, and 2.0 m) were pooled within regions A and B, while transpiration was evaluated separately for trees G and E in region A and tree H in region B. N denotes the number of valid observation–model pairs. RMSE and MBE are expressed in W m^{-2} for PAR and L $tree^{-1}$ for transpiration.

Metric	PAR (W m^{-2})		Transpiration (L $tree^{-1}$)		
	A	B	G	E	H
N	1007	1008	7	7	7
r	0.98	0.96	0.93	0.94	0.71
RMSE	21.92	31.38	0.85	0.28	0.26
NRMSE	0.05	0.08	1.68	0.28	0.52
MBE	0.83	8.08	0.79	0.20	0.01

Additional leaf-temperature evaluation was conducted using observations from Mainz, Germany, under four contrasting sky conditions (Appendix B). SOLWEIG-LEB reproduced the observed diurnal variations, with RMSEs ranging from 1.17 to 1.45 °C (Fig. B3 and Table B1). Compared with Legacy SOLWEIG ($T_{veg} = T_{air}$), RMSE decreased from 1.56 to 1.23 °C under clear-sky conditions and from 2.08 to 1.45 °C under slightly cloudy conditions. However, the improvement was limited under mostly cloudy conditions, while Legacy SOLWEIG yielded a lower RMSE under fully cloudy conditions. These results demonstrate that explicitly calculating leaf temperature using the LEB module can improve leaf-temperature predictions, particularly under conditions with stronger solar forcing.

4.2. Evaluation of pedestrian-level shortwave, longwave, and MRT

Figure 10 compares the total shortwave radiation (K_{tot}), total longwave radiation (L_{tot}), and MRT (T_{mrt}) observed at the pedestrian height (z = 1.1 m) at the Göteborg site with the simulation results from Legacy SOLWEIG and SOLWEIG-LEB. Here, K_{tot} and L_{tot} denote the sums of the six directional shortwave and longwave radiation fluxes, respectively. The comparison was conducted for OP1 on 23 May 2010 and for OP2 on 7, 10, and 12 July 2010. Overall, SOLWEIG-LEB reproduced the temporal variations in observed K_{tot}, L_{tot}, and T_{mrt} well. In particular, K_{tot} and T_{mrt} exhibit rapid increases and decreases associated with direct solar exposure and dynamic changes in tree shading; SOLWEIG-LEB successfully captured these temporal variations in most cases. While Legacy SOLWEIG and SOLWEIG-LEB showed similar overall temporal patterns, distinct differences appeared during specific periods. For example, around 17:00 LST on 23 May 2010 at OP1 and around 11:00 LST on 12 July at OP2, Legacy SOLWEIG tended to underestimate T_{mrt} compared with the observations, whereas SOLWEIG-LEB produced values closer to the observations. These specific periods correspond to microclimatic conditions in which canopy obstruction near the tree-shade boundary exerts a dominant influence. This suggests that the LAD-based path-dependent canopy attenuation scheme in SOLWEIG-LEB represents the actual canopy transmission and attenuation physics more flexibly and realistically than the representative-transmissivity approach utilized in Legacy SOLWEIG. A more detailed analysis of these periods is provided in Section 4.3.

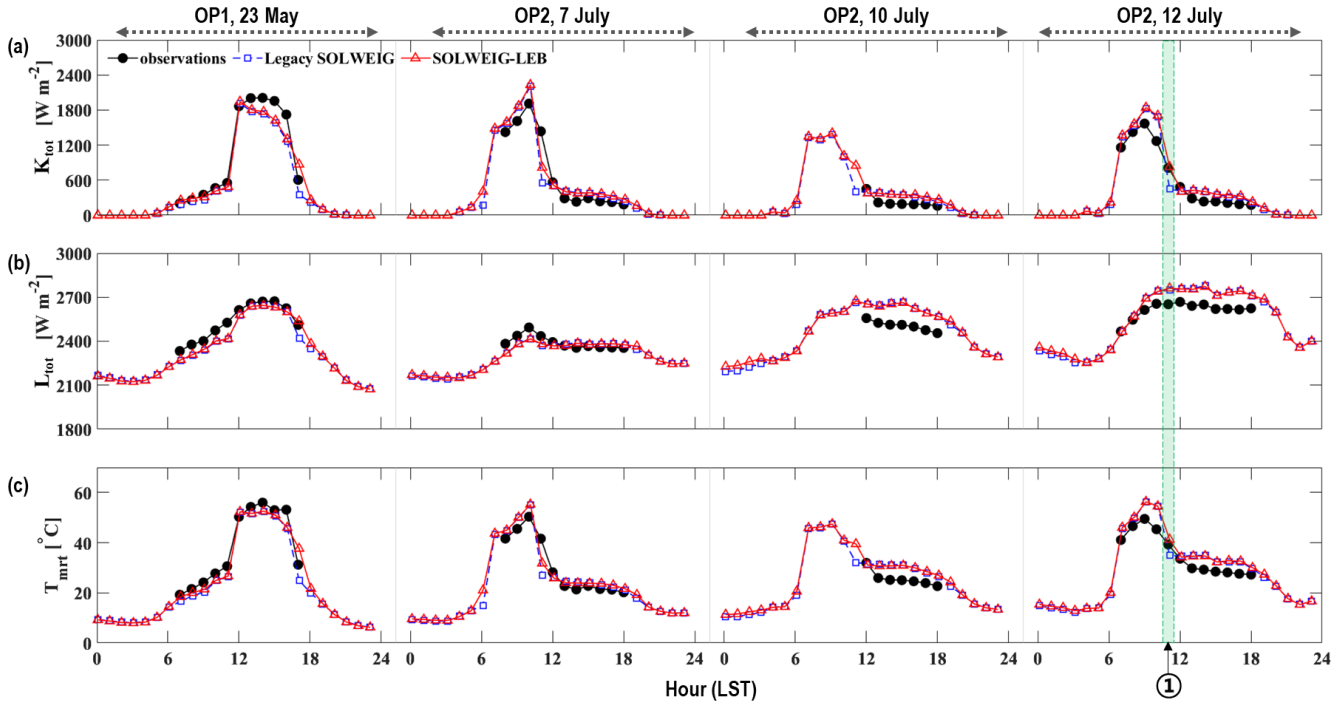

Figure 10. Observed and simulated pedestrian-level (a) total shortwave radiation, (b) total longwave radiation, and (c) MRT at the Göteborg site. Results from Legacy SOLWEIG and SOLWEIG-LEB are compared for the four evaluation periods. The interval marked ① identifies the OP2 case examined in Figs. 12 and 13.

Table 5 presents the quantitative evaluation metrics for K_{tot}, L_{tot}, and T_{mrt} during the observation periods at the Göteborg site. For K_{tot}, SOLWEIG-LEB yielded a higher correlation coefficient and a reduced error magnitude compared to Legacy SOLWEIG. Specifically, the correlation coefficient increased from 0.94 to 0.95, while the RMSE decreased from 231.74 to 203.66 W m^{-2}, and the NRMSE dropped from 0.13 to 0.11. These statistics indicate lower pooled shortwave RMSE for the combined extension in the evaluated sample. However, the MBE increased from 21.90 to 56.78 W m^{-2}, indicating increased mean overestimation of the six-directional shortwave sum. For L_{tot}, SOLWEIG-LEB also showed a slight improvement compared with Legacy SOLWEIG. The correlation coefficients were approximately 0.89 for both models, and the RMSE decreased slightly from 83.42 to 78.93 W m^{-2}. The NRMSE also decreased from 0.25 to 0.23. However, the magnitude of this improvement was smaller than that observed for shortwave radiation, and the MBE decreased from 28.78 to 25.25 W m^{-2}. For T_{mrt}, SOLWEIG-LEB demonstrated an improved predictive performance compared with Legacy SOLWEIG. The correlation coefficient increased from 0.92 to 0.94, the RMSE decreased from 4.76 to 4.38 °C, and the NRMSE decreased from 0.13 to 0.12. However, the MBE increased from 1.36 to 1.90 °C, indicating that SOLWEIG-LEB tended to slightly overestimate T_{mrt} on average across the simulation steps.

Table 5. Statistical evaluation of total shortwave radiation (K_{tot}), total longwave radiation (L_{tot}), and mean radiant temperature (MRT) at the Göteborg site.

Variable	Metric	Legacy SOLWEIG	SOLWEIG-LEB
K_{tot}	r	0.94	0.95
	RMSE [W m^{-2}]	231.74	203.66
	NRMSE	0.13	0.11
	MBE [W m^{-2}]	21.90	56.78
L_{tot}	r	0.89	0.89
	RMSE [W m^{-2}]	83.42	78.93
	NRMSE	0.25	0.23
	MBE [W m^{-2}]	28.78	25.25
MRT	r	0.92	0.94
	RMSE [°C]	4.76	4.38
	NRMSE	0.13	0.12
	MBE [°C]	1.36	1.90

Figure 11 compares observed and modelled radiation fluxes separately for each directional shortwave and longwave radiation component. For the shortwave components, the most pronounced improvements in SOLWEIG-LEB appeared in $K_{\downarrow}$ and $K_{\rightarrow,\mathrm{south}}$. The RMSE of $K_{\downarrow}$ decreased from 84.60 W m^{-2} in Legacy SOLWEIG to 69.60 W m^{-2} in SOLWEIG-LEB, corresponding to an error reduction of approximately 15.00 W m^{-2}. The RMSE of $K_{\rightarrow,\mathrm{south}}$ decreased from 66.00 to 56.00 W m^{-2}, representing an improvement of approximately 10.00 W m^{-2}. $K_{\rightarrow,\mathrm{west}}$ also improved, with its RMSE decreasing from 73.00 to 66.10 W m^{-2}. In contrast, the differences between the two models were negligibly small for $K_{\uparrow}$ and $K_{\rightarrow,\mathrm{north}}$. The largest shortwave RMSE reductions occurred in the downward, southward, and westward components, consistent with the vegetation concentrated to the south and west of OP2. Both observation points were affected by canopy edges and partial obstruction during parts of the day. For the directional longwave components, upward RMSE decreased from 22.20 to 20.30 W m^{-2} and downward RMSE from 33.60 to 31.40 W m^{-2}. Eastward, westward and northward RMSEs decreased by approximately 0.20–0.70 W m^{-2}, while southward RMSE increased from 10.80 to 11.10 W m^{-2}. Changes in directional longwave RMSE were limited to a few W m^{-2} and were smaller than the largest shortwave RMSE reductions. Section 4.3 separates the contributions of canopy attenuation and leaf energy balance to the radiation and MRT differences.

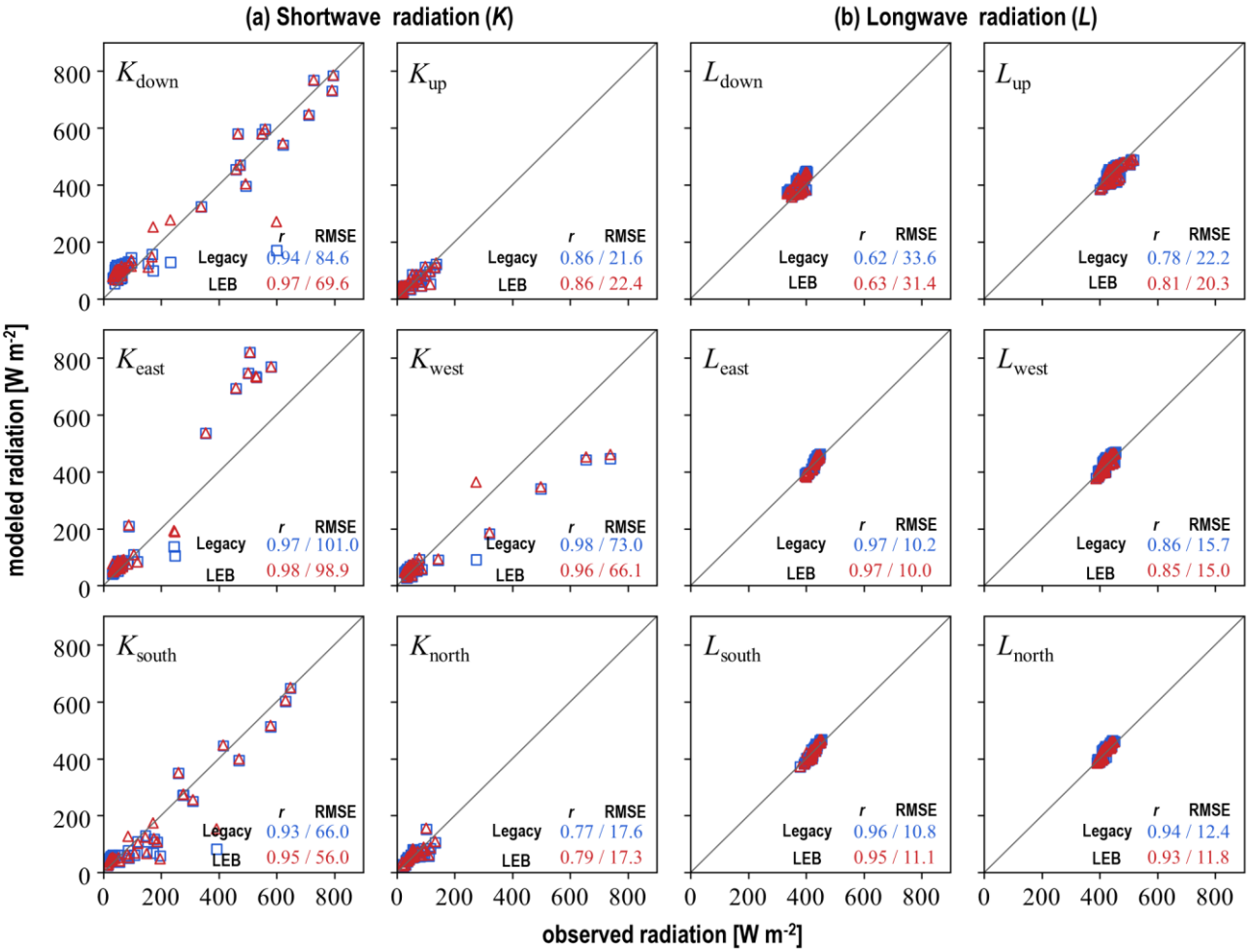

Figure 11. Comparison of observed and simulated six-directional (a) shortwave and (b) longwave radiation fluxes at the Göteborg site. Blue squares and red triangles denote Legacy SOLWEIG and SOLWEIG-LEB, respectively, and the diagonal line represents perfect agreement.

4.3. Contributions of LAD-based canopy attenuation and leaf energy balance

The comparison in Section 4.2 reflects the combined effects of modifications in canopy shortwave attenuation and vegetation surface temperature. To isolate and separate the individual contributions of these two processes, an additional LAD-only numerical experiment was performed in which the LAD-based canopy attenuation scheme was fully retained, but vegetation temperature was prescribed as $T_{veg} = T_{air}$, identical to the isothermal assumption in Legacy SOLWEIG. This sensitivity experiment is hereafter referred to as EXP1, whereas the full SOLWEIG-LEB experiment, incorporating both LAD-based attenuation and the voxel-scale leaf energy balance, is designated as EXP2. The same geometry, LAD distributions, meteorological forcing, and surface properties were applied across both EXP1 and EXP2. Consequently, the comparison between EXP1 and Legacy SOLWEIG isolates the structural and optical changes associated with the LAD-based canopy

representation, whereas the differential term EXP2 − EXP1 isolates the additional effect of the leaf energy balance within an identical LAD-based radiation framework.

Figure 12 illustrates the spatial patterns of canopy attenuation at 11:00 LST on 12 July 2010 (① in Fig. 10) using ground-level direct shortwave transmissivity (τ). Higher values of τ indicate greater penetration of direct solar radiation; τ = 0 when buildings completely block the radiative path, and τ = 1 when the optical path is entirely unobstructed. Legacy SOLWEIG applies a fixed transmissivity of 0.03 to all pixels shaded by vegetation, regardless of the path length through the canopy (Fig. 12a). In contrast, SOLWEIG-LEB resolves transmissivity from the cumulative LAD accumulated along each radiative path, capturing pronounced attenuation contrasts between the dense canopy core and permeable crown edges (Fig. 12b). At OP2, direct radiation traversed a relatively short path near the northern crown edge, resulting in a local transmissivity of approximately 0.3, which was an order of magnitude higher than the fixed value of 0.03 in Legacy SOLWEIG. Figure 12c displays the resulting spatial discrepancies. The identical LAD-based transmissivity field was applied in both EXP1 and EXP2.

Figure 13 compares the spatial distributions of SVF, six-directional total shortwave radiation (K_{tot}), total longwave radiation (L_{tot}), and MRT at 11:00 LST on 12 July 2010. The first column illustrates the baseline absolute fields simulated by Legacy SOLWEIG, while the remaining columns display the difference fields for EXP1 − Legacy SOLWEIG, EXP2 − Legacy SOLWEIG, and EXP2 − EXP1, respectively. Because EXP1 and EXP2 share the identical LAD-based attenuation scheme, they yield identical SVF and shortwave radiation distributions (Fig. 13a, b). At OP2, the observed Ktot was 810.30 W m^{-2}, whereas Legacy SOLWEIG substantially underestimated this radiative load at 450.70 W m^{-2}. This confirms that the conventional fixed-transmissivity scheme severely overestimates shortwave extinction along peripheral canopy trajectories. In contrast, both EXP1 and EXP2 simulated 826.41 W m^{-2}, achieving remarkable agreement with the in situ observation.

Spatial discrepancies associated with LAD-based attenuation were also pronounced across the broader domain outside OP2. Compared with Legacy SOLWEIG, SVF increased by more than 0.1 in boundary grid cells along crown perimeters, but decreased by approximately 0.01–0.02 within dense core canopies (Fig. 13a). At crown boundaries, K_{tot} increased locally by 300–400 W m^{-2} or more, whereas it decreased by several tens of W m^{-2} beneath dense canopy interiors where cumulative optical depth exceeded that implied by the fixed legacy transmissivity (Fig. 13b). These spatial differences show that the voxel-resolved calculation represents path-length differences between crown interiors and edges that cannot be resolved by bulk transmissivity models.

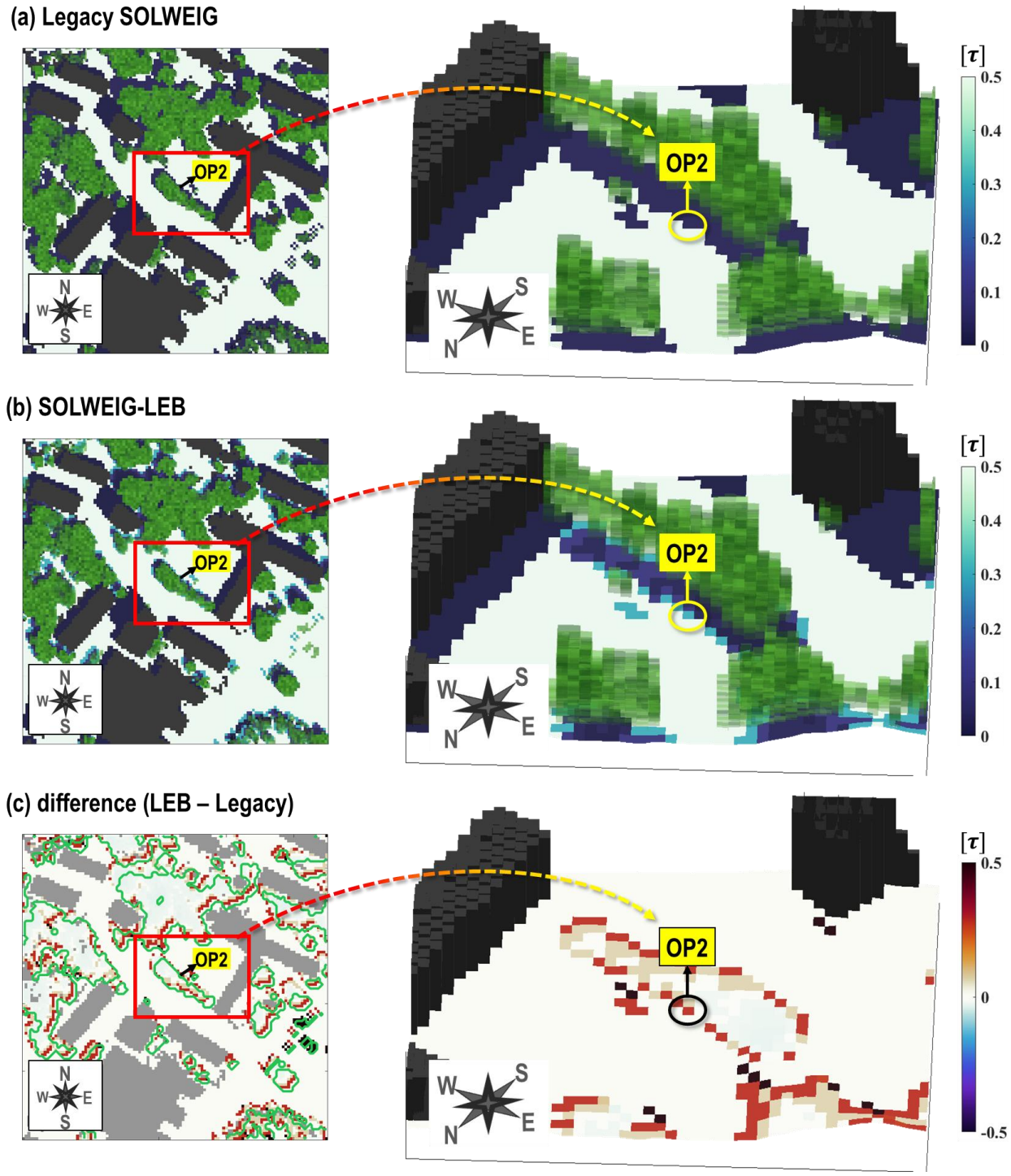

750 **Figure 12. Ground-level direct-shortwave transmissivity at 11:00 LST on 12 July 2010. (a) Legacy SOLWEIG, (b) SOLWEIG-LEB, and (c) their difference. The right panels enlarge the area around OP2.**

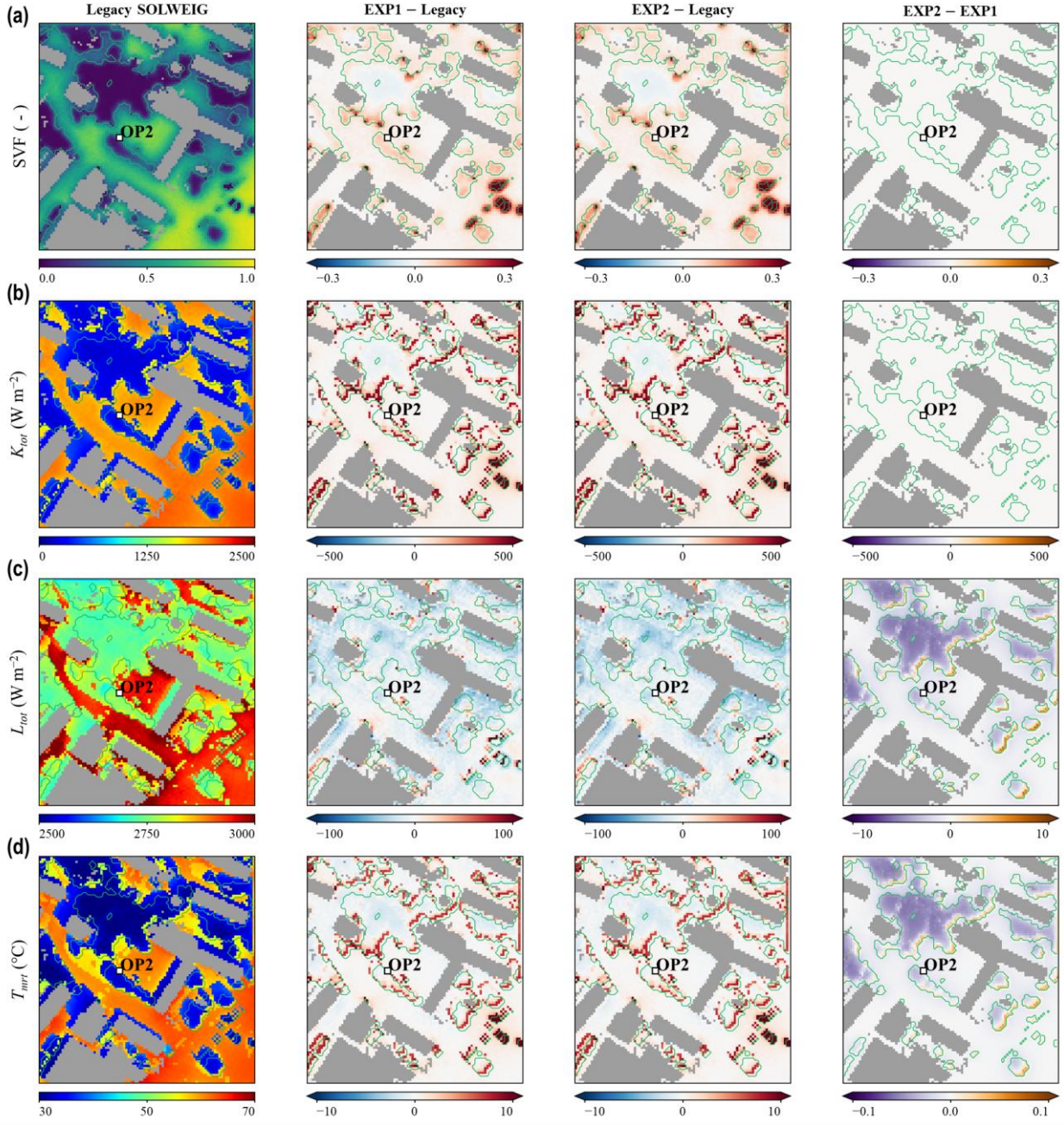

Figure 13. Spatial distributions of pedestrian-level (a) sky view factor (SVF), (b) six-directional shortwave radiation sum (K_{tot}), (c) six-directional longwave radiation sum (L_{tot}), and (d) mean radiant temperature (MRT) at 11:00 LST on 12 July 2010. EXP1 and EXP2 denote the LAD-only and full SOLWEIG-LEB configurations, respectively. The first column shows Legacy SOLWEIG, while the remaining columns show differences calculated as EXP1 − Legacy SOLWEIG, EXP2 − Legacy SOLWEIG, and EXP2 − EXP1, respectively.

L_{tot} in EXP1 was generally lower than in Legacy SOLWEIG, exhibiting local reductions of approximately 50–85 W m^{-2} (Fig. 13c). SOLWEIG calculates downwelling sky longwave radiation using an effective sky emissivity parameterized from air temperature and humidity (Wallenberg et al., 2023). At this specific time step, the effective sky emissivity was approximately 0.82, lower than the vegetation emissivity of 0.90 applied in EXP1. Consequently, even under the isothermal assumption, an increase in vegetation transmissivity (and effective SVF) increases the relative view-factor weighting of radiatively colder open sky while reducing the downward emission contribution from the warmer tree crown. This directional re-weighting explains the systematic decrease in L_{tot} observed in EXP1.

The difference fields for EXP2 − EXP1 (the final column of Fig. 13) were zero for SVF and shortwave radiation, while localized deviations emerged beneath the canopy for longwave radiation and MRT. L_{tot} decreased by approximately 2–6 W m^{-2} in areas beneath the canopy, with the reduction decaying toward the crown periphery. Conversely, it increased by up to 6.8 W m^{-2} in some areas beneath the canopy. This divergence stems from the thermodynamic behavior of the leaf energy balance: leaves cooler than the air emitted less longwave radiation, whereas leaves warmer than the ambient air emitted greater longwave flux. Reflecting these longwave shifts, MRT decreased by approximately 0.02–0.06 °C in areas with reduced longwave radiation, and increased by up to 0.05 °C in areas with increased longwave radiation. These LEB-induced longwave and MRT modifications were minor in magnitude compared to the primary differences driven by LAD-based shortwave attenuation. Across the complete Göteborg validation dataset, the overall MRT RMSEs were 4.76 °C for Legacy SOLWEIG, 4.39 °C for EXP1, and 4.38 °C for EXP2.

Figure 14 compares the temporal variations in shortwave radiation, longwave radiation, and MRT using the differences for EXP1 − Legacy SOLWEIG, EXP2 − Legacy SOLWEIG, and EXP2 − EXP1. The domain in Fig. 13 was partitioned into three mutually exclusive spatial subregions: under-canopy, tree-adjacent, and open zones. Under-canopy zones were defined as grid cells falling within the vertical canopy footprint. Tree-adjacent zones comprised non-canopy grid cells with centres no more than 4 m horizontally from the canopy boundary, while open zones comprised cells farther than 4 m from the boundary. Buildings were excluded from the analysis. Solid lines denote spatial area-mean differences, while shaded bands represent the spatial 10th–90th percentile (P10–P90) range of paired cellwise model differences at each time step. Both LAD-enabled simulations (EXP1 and EXP2) exhibited nearly identical diurnal trajectories relative to Legacy SOLWEIG (Figs. 14a and b). Daytime area-mean shortwave radiation differences were positive and were substantially amplified in under-canopy and tree-adjacent zones relative to open zones. The area-mean shortwave increases in under-canopy and tree-adjacent zones reached approximately 170 and 150 W m^{-2}, respectively, while the spatial 90th percentile (P90) exceeded 600 W m^{-2}. Conversely, the area-mean longwave radiation differences relative to Legacy SOLWEIG were predominantly negative during daytime across all three zones, although the spatial P90 reached approximately 20 W m^{-2} in tree-adjacent and open zones. Daytime MRT was also generally higher in EXP1 and EXP2 than in Legacy SOLWEIG. The area-mean MRT increases in EXP2 reached approximately 2.7, 2.5, and 1.1 °C in under-canopy, tree-adjacent, and open zones, respectively, with the spatial P90 exceeding 10 °C in under-canopy and tree-adjacent zones at some times. Overall, the spatial P10–P90 ranges of the

shortwave radiation and MRT differences were wider in under-canopy and tree-adjacent zones than in open zones, indicating greater spatial variability in the model differences associated with path-dependent canopy attenuation.

In contrast, the thermodynamic modifications introduced by the leaf energy balance solver (EXP2 − EXP1) remained minor (Fig. 14c). Because EXP2 and EXP1 shared identical shortwave ray-tracing, shortwave radiation differences were identically zero across all zones. The area-mean longwave radiation differences were positive or negative depending on the time and zone, generally confined within a few W m^{-2}. The resulting MRT differences were also small, with the P10–P90 range generally within approximately ±0.06 °C, even in under-canopy zones where spatial variability was greatest. This demonstrates that while calculating leaf temperature modifies vegetation longwave radiation, its additional effect on pedestrian-level MRT is quantitatively modest under the evaluated conditions. Consequently, the improvement in pedestrian-level MRT relative to Legacy SOLWEIG was primarily associated with LAD-based path-dependent canopy attenuation under the evaluated conditions.

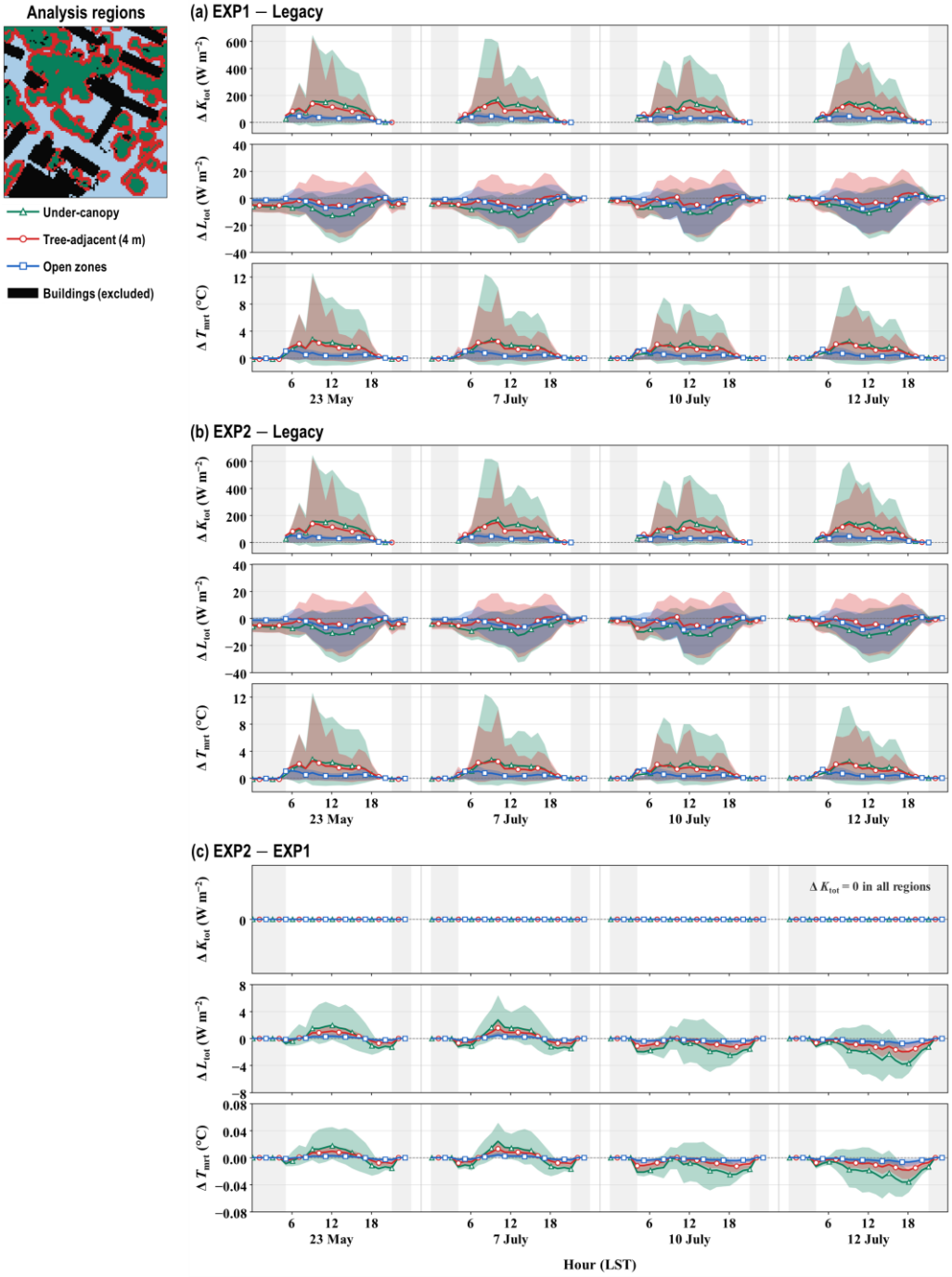

Figure 14. Differences in six-directional shortwave and longwave sums (ΔK_{tot} and ΔL_{tot}) and MRT (ΔT_{mrt}) for (a) EXP1 − Legacy SOLWEIG, (b) EXP2 − Legacy SOLWEIG, and (c) EXP2 − EXP1. EXP1 and EXP2 denote the LAD-only and full SOLWEIG-LEB configurations, respectively. Green, red, and blue indicate under-canopy, tree-adjacent (within 4 m), and open zones, respectively. Lines and shading show spatial means and 10th–90th percentile (P10–P90) ranges of paired cellwise differences at each time step. Black areas in the map indicate excluded buildings, and grey shading indicates nighttime.

4.4. Analysis of voxel-scale leaf energy balance processes

Pedestrian-level T_{mrt} describes human radiative exposure but does not resolve leaf thermal responses or canopy energy partitioning. This section examines the case at 11:00 LST on 12 July 2010 shown in Fig. 15. The spatial distributions of leaf net radiation (R_{net} in Eq. (14)), leaf temperature (T_{veg}), sensible heat flux (H), and latent heat flux (LE) in vegetation voxels are analysed to examine how energy within the canopy is partitioned between sensible heat exchange and transpiration. At this time, the background air temperature was 29.8 °C, relative humidity was 41.8 %, and global shortwave radiation input was 721.6 W m^{-2}. Background wind speed, air pressure, and CO_2 concentration were set to 3.0 m s^{-1}, 101.3 kPa, and 420 ppm, respectively. Under spatially uniform meteorological forcing, voxel-scale differences primarily reflected local radiative exposure associated with canopy geometry and the coupled responses of leaf temperature, leaf boundary-layer resistance, and stomatal resistance. As described in Section 2.5, SOLWEIG-LEB iteratively updates T_{veg}, vegetation longwave emission, H, and LE. Figure 15 shows the spatial distributions of R_{net}, T_{veg}, H, and LE. The left panel in each row shows the three-dimensional vegetation voxel distribution over the entire analysis domain, and the right panel shows an x–z cross-section at y = 125 m. The location of this cross-section is indicated by a red plane in the three-dimensional view. The three-dimensional distributions show overall differences among trees, whereas the cross-sections reveal horizontal and vertical heterogeneity within the canopy that is obscured by the outer voxels.

R_{net} ranged from 5.0 to 295.1 W m^{-2} (Fig. 15a). Net radiation was higher on sun-facing canopy surfaces and in areas with greater radiative exposure and was lower on shaded canopy surfaces facing away from the sun. In the x–z cross-section, R_{net} was also non-uniform within individual canopies and varied substantially with canopy height and the depth of voxels within the canopy. These patterns reflect the effects of three-dimensional canopy structure and shading by surrounding objects on voxel-scale net radiation.

T_{veg} ranged from 28.5 to 31.8 °C (Fig. 15b). Relative to the background air temperature of 29.8 °C, the calculated T_{veg} ranged from approximately 1.3 °C lower to 2.0 °C higher. Higher leaf temperatures occurred mainly at sun-facing canopy edges and in areas with greater radiative exposure, whereas lower temperatures occurred on shaded canopy surfaces facing away from the sun and deep within the canopy. This distribution of T_{veg} reflects the balance between radiative heating, sensible heat exchange, and transpiration in each voxel.

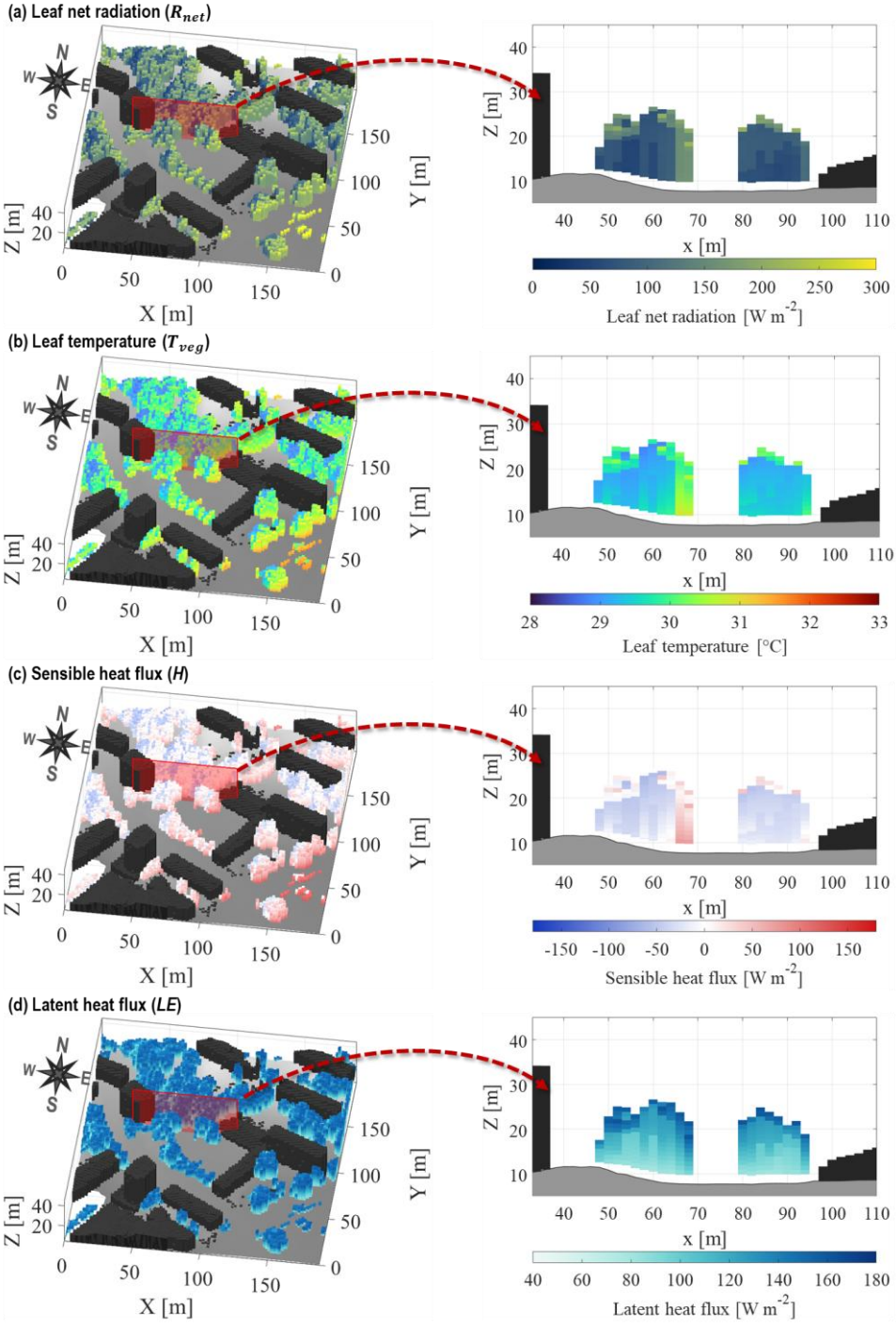

Figure 15. Voxel-scale distributions of (a) leaf net radiation, (b) leaf temperature, (c) sensible heat flux, and (d) latent heat flux calculated by SOLWEIG-LEB at 11:00 LST on 12 July 2010. Left panels show three-dimensional vegetation-voxel fields, and right panels show the corresponding x–z cross-sections at y = 125 m, indicated by the red planes in the three-dimensional views. Fluxes are per unit one-sided leaf area.

At the end of the calculation, R_{net} was approximately balanced by sensible heat exchange with the surrounding air, *H*, and latent heat flux associated with transpiration, LE (Figs. 15c and d). *H* per unit one-sided leaf area ranged from approximately −84.9 to 139.6 W m^{-2} (Fig. 15c) and was higher in canopy regions with higher leaf temperatures. LE varied over a narrower range of approximately 56.0–165.9 W m^{-2} (Fig. 15d). Positive *H* indicates heat transfer from the leaf to the atmosphere, whereas negative H indicates heat transfer from the atmosphere to the leaf. Thus, sensible heat exchange in both directions coexisted within the canopy. In voxels with negative *H*, sensible heat supplied by the atmosphere contributed, together with net radiation, to the energy required for transpiration. These voxel-scale fields distinguish the direction of leaf–air heat exchange and its contribution to transpiration, providing information beyond the pedestrian MRT response.

4.5. Computational performance and scalability

The benchmark evaluates preprocessing time, per-timestep runtime, and GPU memory demand for the configurations described in Section 3.3. This comparison quantifies the additional computational cost of LAD-based attenuation and leaf energy balance within the GPU framework. As the horizontal domain size increased from 50 × 50 to 600 × 600 grid cells, the numbers of active vegetation voxels and wall-surface voxels increased continuously (Fig. 16a). The largest 600 × 600 domain contained 360,000 horizontal grid cells, approximately 1.02 million active vegetation voxels, and 0.26 million wall-surface voxels. The increase in computational time with domain size was particularly pronounced during preprocessing in the CPU-based Legacy SOLWEIG (Fig. 16b). For the 600 × 600 domain, the SVF and wall-preprocessing time was 109.9 min for CPU-based Legacy SOLWEIG, whereas the corresponding GPU-based SOLWEIG-LEB preprocessing required 4.75 min. This corresponds to an approximately 23.1-fold speed-up, with the benefit of GPU parallelization becoming increasingly evident as the domain size increased.

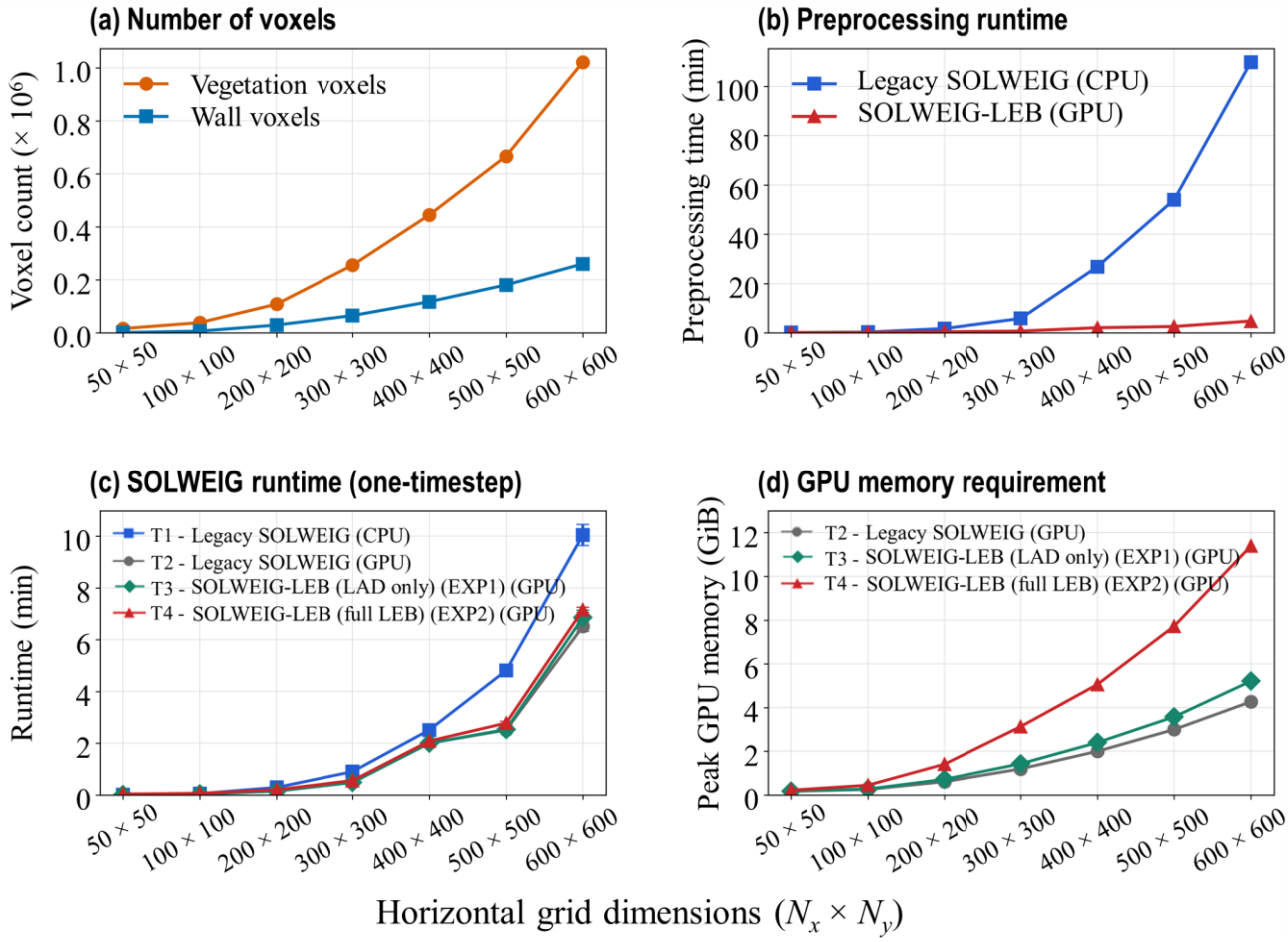

Figure 16. Computational workload and performance with increasing horizontal domain size. (a) Numbers of active vegetation and wall-surface voxels, (b) SVF and wall-preprocessing time for CPU-based Legacy SOLWEIG and GPU-based SOLWEIG-LEB, (c) single-timestep runtime for the four benchmark configurations, with error bars indicating the standard deviation of three repeated runs, and (d) peak device-memory usage for the GPU-based configurations.

The per-timestep runtime also increased systematically with domain size (Fig. 16c). For the same legacy-equivalent configuration at 600 × 600, the mean runtime of the CPU-based T1 configuration was 10.05 min, whereas the GPU-based T2 configuration required 6.51 min, corresponding to a 35.2 % reduction in runtime. Within the same GPU framework, the additional computational overhead of the newly introduced vegetation schemes remained relatively limited. The runtime of T3, in which only LAD-based shortwave attenuation was activated, was 6.85 min, representing a 5.2 % increase relative to T2. The full-LEB configuration, T4, required 7.15 min, corresponding to a further 4.4 % increase relative to T3. Consequently, activating both LAD-based attenuation and the full LEB increased the runtime by only approximately 9.8 % relative to the legacy-equivalent GPU configuration. These results indicate that the three-dimensional canopy ray-tracing and iterative leaf energy balance introduce additional computational workload, but the actual increase in timestep runtime remains minor under

GPU execution. Under the tested hardware and implementation conditions, T4 required 28.9 % less runtime than the CPU-based T1 configuration, despite including both vegetation modules.

In contrast, GPU memory usage increased more prominently with domain size and the number of active vegetation voxels (Fig. 16d). For the 600 × 600 domain, peak GPU memory allocation was 4.27, 5.21, and 11.39 GiB for T2, T3, and T4, respectively. The memory footprint of T3 was approximately 22.0 % greater than that of T2, indicating that LAD-based attenuation alone imposed a relatively limited additional memory demand during the per-timestep calculation. In contrast, the full LEB configuration required approximately 2.2 times more GPU memory than T3 because multiple three-dimensional diagnostic arrays related to leaf temperature, radiation balance, sensible and latent heat fluxes, and iterative calculations were allocated and stored for each active vegetation voxel. At 600 × 600 grid cells, T4 used approximately 95.4 % of the available GPU memory, suggesting that memory capacity may constrain full-LEB applications at larger domain sizes. In the tested configurations, LAD-only T3 incurred smaller runtime and memory increases than T4, making it a less resource-demanding option when vegetation-voxel energy-balance diagnostics are not required.

5. Discussion

5.1. Evaluation performance and interpretation

In Angers, SOLWEIG-LEB reproduced leaf-temperature variations, with lower leaf-temperature and MRT RMSEs than Legacy SOLWEIG in both vegetated regions. The PAR and transpiration comparisons evaluated canopy light attenuation and tree water loss. Additional leaf-temperature validation in Mainz covered contrasting sky conditions (Appendix B). In Göteborg, SOLWEIG-LEB reduced shortwave, longwave, and MRT RMSEs relative to Legacy SOLWEIG, although positive biases increased for total shortwave radiation and MRT. The largest shortwave improvements occurred in the downward and selected sideward components during periods affected by canopy edges and partial obstruction.

Previous studies have shown that prescribed canopy transmissivity strongly affects MRT estimates in tree shade. Lindberg and Grimmond (2011) demonstrated the sensitivity to fixed transmissivity, while Konarska et al. (2014) reported low mean direct transmissivity through dense, foliated crowns and greater variability near crown edges and gaps. Park et al. (2018) also showed that daytime MRT changes with LAD are primarily associated with shortwave attenuation.

The finding in Section 4.3 that EXP1 reproduced nearly all of the MRT RMSE reduction achieved by EXP2 (accounting for over 97 % of the total error reduction) demonstrates that, under the evaluated conditions in Göteborg, improvements in pedestrian-level MRT relative to Legacy SOLWEIG were overwhelmingly governed by LAD-based canopy radiative treatment. Furthermore, the pronounced spatial dispersion (evidenced by the broad spatial P10–P90 ranges) observed beneath and adjacent to the canopy underscores that local microclimatic extremes and fine-scale spatial heterogeneity must be considered alongside domain area-mean differences. The LAD-based scheme represents differences among paths through canopy cores, edges, and gaps rather than applying a single bulk transmissivity to all vegetation-shaded locations. Its

performance depends on the prescribed LAD, leaf-angle distribution, canopy geometry, and observation location. These factors are particularly relevant near canopy boundaries, where small geometric differences can alter direct solar exposure. The Angers evaluation complements the Göteborg analysis by assessing the vertical distribution of PAR, leaf temperature, and tree transpiration. PAR observations provide an additional assessment of canopy shortwave attenuation, whereas leaf-temperature and transpiration observations evaluate the thermal response and tree-level water loss calculated by the leaf energy balance module. Together, these comparisons extend the observational evaluation of SOLWEIG-LEB beyond its contribution to pedestrian-level MRT accuracy.

5.2. Added capabilities and intended scope of SOLWEIG-LEB

SOLWEIG-LEB integrates LAD-based canopy attenuation with a voxel-scale leaf energy balance, extending the vegetation representation in SOLWEIG to include intra-canopy thermal states and energy partitioning. This development is consistent with recent efforts to represent the thermal states of individual urban surfaces more explicitly within the SOLWEIG framework. Wallenberg et al. (2026) introduced a method for calculating wall surface temperature based on local radiative balance and material properties, and the present study advances this trajectory by establishing an explicit representation of vegetation thermal states within SOLWEIG. SOLWEIG-LEB is a diagnostic model that calculates the canopy radiative environment and leaf energy balance under prescribed meteorological forcing. Unlike prognostic microclimate models such as ENVI-met or PALM-4U, which resolve atmospheric flow and turbulent transport of heat and moisture interactively through time, SOLWEIG-LEB focuses on path-dependent radiative transfer associated with three-dimensional canopy structure and steady-state thermal response of vegetation. Although the leaf energy balance module provided only a small additional improvement in pedestrian-level MRT accuracy under the evaluated Göteborg conditions, its principal added value lies in diagnosing leaf temperature and sensible and latent heat exchange within the canopy. Specifically, the full LEB configuration enables analysis of the relationship between spatial variations in canopy radiation, leaf–air temperature differences, and the balance among net radiation, sensible heat exchange, and latent heat flux. Furthermore, the Angers evaluation demonstrates how voxel-scale latent heat fluxes can be converted into tree-level transpiration estimates using representative leaf area. This modular model structure allows the level of detail to be flexibly selected according to the intended application and available computational resources. Under conditions similar to those evaluated here, the LAD-only configuration (EXP1/T3) can be used when pedestrian radiative conditions and MRT are the primary variables of interest, whereas the full LEB configuration (EXP2/T4) is appropriate when leaf temperature and intra-canopy sensible and latent energy partitioning need to be explicitly resolved. In the benchmarks (Section 4.5), the full LEB required only a minor increase in runtime (approximately 4.4 % relative to T3) but substantially more peak GPU memory than the LAD-only configuration. Therefore, applications over large domains or at high spatial resolution should consider both the required diagnostic variables and the available GPU memory. The voxel-scale leaf temperature and sensible and latent heat fluxes calculated by the full LEB may also support future coupling with atmospheric models. When spatially aggregated using leaf-area density information, these fluxes could provide volumetric

source and sink terms representing vegetation heat and moisture exchange in computational fluid dynamics (CFD) or multi-layer urban canopy models. In addition, the three-dimensionally resolved intra-canopy light environment and leaf temperature can provide essential biophysical inputs for modelling biogenic volatile organic compound (BVOC) emissions.

5.3. Limitations and future development

The present evaluation has several limitations that should be addressed in future investigations. First, the supplementary Mainz evaluation covered a single tree species under four contrasting sky conditions (Appendix B). In Mainz, the precise location and spatial arrangement of the observed foliage within the reported sensor footprint were unavailable, so the estimated lower-canopy sampling area may not coincide with the infrared sensor's observation footprint. Air temperature and relative humidity obtained from a meteorological station approximately 3 km away may also differ from the conditions surrounding the observed leaves. These uncertainties may affect the agreement between simulated and observed leaf temperatures.

Second, the Göteborg evaluation covered only two distinct spatial locations across four days, restricted to foliated conditions in late spring and summer. These initial results are therefore insufficient to comprehensively establish model performance across different tree species, seasons, complex canopy geometries, and highly variable meteorological conditions. Further evaluation is warranted for leafless deciduous trees, evergreen trees, sparse canopies, and crown-edge conditions.

Third, the numerical representation of canopy structure involves several simplifying assumptions. The current version assumes a spherical leaf angle distribution with a leaf projection function of G_{proj} = 0.5, and LAD is assumed to be uniformly distributed within the canopy envelope when high-resolution observed LAD profiles are unavailable. However, actual LAD, leaf inclination and azimuth distributions, foliage clumping, and branch structure may vary with species, growth stage, canopy height, and position within the canopy. Consequently, G_{proj} may also vary with solar position and leaf orientation distribution. The sensitivity analysis in Appendix C showed that variations in G_{proj} associated with different leaf orientation distributions can affect direct shortwave transmissivity and local MRT. Therefore, future developments should incorporate measured three-dimensional canopy geometry, spatially resolved LAD and leaf orientation distributions, and foliage clumping and branch structures, using data derived from terrestrial laser scanning, hemispherical photography, or within-canopy radiation measurements.

Fourth, the leaf energy balance module solves a steady-state balance and consequently neglects internal leaf heat storage and thermal inertia effects. Stomatal resistance is obtained by coupling the CANOAK C3 biochemical photosynthesis model with Ball–Berry stomatal conductance (Appendix A). The physiological parameters and their applicability to different tree species require further evaluation. Furthermore, sub-surface soil moisture and atmospheric CO_2 are prescribed, while hydrologic processes such as rainfall, canopy interception, soil evaporation, root-water uptake, and temporal soil-moisture changes are not represented. Soil-water stress can therefore be represented through the prescribed water-availability factor, but the model does not predict the evolution of soil water or plant hydraulic stress during prolonged drought or rainfall events.

Fifth, the nighttime leaf energy balance was evaluated in Angers and Mainz, extending the original daytime calculation to account for nighttime radiative cooling and vegetation longwave emission. Background CO_2 was fixed at 420 ppm, and the empirical surface-temperature coefficients and wall albedo in Angers were site-specific. Another critical limitation is the absence of a two-way vegetation–atmosphere coupling framework. The calculated *H* and *LE* remain purely diagnostic outputs and do not actively update the prognostic air temperature or humidity fields. Likewise, a spatially uniform background wind speed is applied to all vegetation voxels, whereas actual within-canopy wind speed profiles and turbulence structures vary substantially depending on the canopy density and surrounding urban geometry. Thus, the current voxel-scale *H* and *LE* outputs must be interpreted as local equilibrium responses to a prescribed atmospheric condition. Further optimization of GPU memory allocation will be required for full-LEB applications to larger or higher-resolution domains.

Consequently, future developments will focus on coupling SOLWEIG-LEB with computational fluid dynamics (CFD) frameworks or multilayer urban canopy models. The high-resolution vegetation-voxel *H* and *LE* fields can be converted to atmospheric source terms using voxel leaf area, receiving air volume, and the latent heat of vaporization. Updated air temperature, humidity, and wind fields can then be returned to the leaf energy balance module.

6. Conclusions

In this study, we developed SOLWEIG-LEB v1.0 as an advanced extension of the vegetation representation within the SOLWEIG radiation model. The updated model replaces a single representative canopy transmissivity with path-dependent shortwave attenuation based on leaf area density (LAD) and discrete radiative paths, and solves a voxel-scale leaf energy balance for individual vegetation voxels to diagnose leaf temperature, vegetation longwave emission, and sensible and latent heat fluxes. Evaluation against observations in Angers showed leaf-temperature RMSEs of 1.72 and 1.61 °C in regions A and B, respectively, compared with 1.82 and 2.19 °C for Legacy SOLWEIG. MRT RMSEs were also lower in both vegetated regions. The Angers evaluation additionally assessed within-canopy PAR and tree transpiration, while supplementary leaf-temperature validation in Mainz covered four contrasting sky conditions (Appendix B). In Göteborg, SOLWEIG-LEB produced lower RMSEs for shortwave radiation, longwave radiation, and mean radiant temperature (MRT) than Legacy SOLWEIG, although positive biases increased slightly for shortwave radiation and MRT.

Under the evaluated conditions in Göteborg, the main changes in pedestrian MRT relative to Legacy SOLWEIG were primarily associated with LAD-based canopy attenuation, whereas the additional thermodynamic effect of the leaf-temperature calculation was small. The maximum absolute area-mean MRT difference between the full LEB and LAD-only configurations was approximately 0.04 °C under the canopy. Nevertheless, the full LEB successfully resolved spatial variations in leaf net radiation, leaf temperature, and sensible–latent heat partitioning within the canopy, providing critical biophysical information on vegetation thermal states and energy exchange beyond pedestrian MRT alone. In the transmissivity experiments in Göteborg (41 observation–simulation pairs), the reference full LEB configuration yielded a lower pooled MRT RMSE (4.38 °C) than any of the six fixed-transmissivity Legacy SOLWEIG configurations (4.76–10.06 °C; Appendix C). The

computational benchmarks showed relatively modest increases in per-timestep runtime (approximately 9.8 % relative to the legacy-equivalent GPU configuration) but substantially greater peak GPU memory demand when the full LEB configuration was activated. These results identify memory demand as an important consideration for large-domain or high-resolution applications.

SOLWEIG-LEB therefore extends the existing SOLWEIG radiation framework from pedestrian radiative assessment to the three-dimensional diagnosis of canopy thermal states and energy exchange while retaining its computationally efficient, prescribed-meteorological-forcing approach. The resulting spatial information may support future coupling with atmospheric or urban canopy models as volumetric source terms, as well as provide essential microclimatic inputs for applications such as biogenic volatile organic compound (BVOC) emission modelling.

Appendix A. Photosynthesis and stomatal coupling for transpiration and leaf temperature

Stomata regulate CO_2 uptake for photosynthesis and water vapor loss through transpiration. SOLWEIG-LEB uses the CANOAK photosynthesis–stomatal coupling to calculate stomatal conductance and link it to transpirational latent heat loss and leaf temperature.

A1. Photosynthesis and net assimilation

Photosynthesis is calculated using the C_3 photosynthesis model of Farquhar et al. (1980) and the coupling approach of Baldocchi (1994). The Rubisco-limited and electron-transport-limited assimilation rates are calculated as follows:

$$W_c = \frac{V_{c\,max}\,(C_i - \Gamma*)}{C_i + K_c\,(1 + C_{O_2}/K_o)}, \quad \text{(A1)}$$

$$W_j = \frac{J\,(C_i - \Gamma*)}{4\,(C_i + 2\Gamma*)}, \quad \text{(A2)}$$

where W_c and W_j are the Rubisco-limited and electron-transport-limited assimilation rates, respectively. Both rates account for photorespiration but are expressed before subtracting mitochondrial respiratory CO_2 release. $V_{c\,max}$ is the maximum carboxylation capacity, and J is the electron-transport rate. Assimilation, carboxylation capacity, and respiration rates are expressed in μmol CO_2 m^{-2} s^{-1} per unit one-sided leaf area. C_i is the intercellular CO_2 mole fraction, and Γ^* is the CO_2 compensation point at which uptake balances photorespiratory release in the absence of mitochondrial respiration. K_c and K_o are the Michaelis–Menten constants for CO_2 and O_2, respectively, and C_{O2} is the O_2 mole fraction. Gas mole fractions, Γ^*, K_c, and K_o have units of μmol mol^{-1}. The electron-transport rate J increases with incident light and approaches J_{max} according to the following saturating light-response function.

$$J = \frac{\alpha_J\, I_{PAR}}{\sqrt{1 + (\alpha_J\, I_{PAR}/J_{max})^2}}, \quad \text{(A3)}$$

where α_J is the effective light-response coefficient, I_{PAR} is the incident photosynthetically active radiation (PAR) photon flux (μmol photons m^{-2} s^{-1}), and J_{max} is the maximum electron-transport rate. J and J_{max} have units of μmol electrons m^{-2} s^{-1} per unit one-sided leaf area. The implementation selects the process giving the lower assimilation rate at an initial $C_i = 0.7C_a$ and retains this process when solving the coupled assimilation–stomatal conductance equations. C_a is the ambient CO_2 mole fraction. Positive net assimilation is subject to an empirical cap based on the capacity for photosynthetic product utilization or export (Collatz et al., 1991):

$$A = \min[A_*, \frac{V_{cmax}}{2} - R_d], \quad \text{(A4)}$$

$$A_* = W_{lim}(C_{i,*}) - R_d, \quad \text{(A5)}$$

where A is net CO_2 assimilation after capping, and A_* and $C_{i,*}$ are the net assimilation and intercellular CO_2 mole fraction from the coupled solution before capping. W_{lim} is the selected W_c or W_j, and R_d is mitochondrial respiration. When the cap is active, leaf-surface and intercellular CO_2 mole fractions and stomatal conductance are recalculated using the capped A.

A2. CO_2 diffusion and stomatal conductance

Assimilation and stomatal conductance are linked through CO_2 diffusion between the ambient air, leaf surface, and leaf interior:

$$C_s = C_a - \frac{A}{g_{b,CO_2}}, \tag{A6}$$

$$C_i = C_s - \frac{1.6\,A}{g_{s,w}}, \tag{A7}$$

where C_s is the leaf-surface CO_2 mole fraction. g_{b,CO_2} and $g_{s,w}$ are boundary-layer conductance for CO_2 and stomatal conductance for water vapor (mol m^{-2} s^{-1}), respectively, and the factor 1.6 represents the ratio of the molecular diffusivity of water vapor to that of CO_2 in air. Boundary-layer resistance for CO_2 is obtained by multiplying the water-vapor boundary-layer resistance $r_{b,vap}$ (s m^{-1}) by the water-vapor to CO_2 diffusivity ratio raised to the power of 2/3, then converted to molar conductance using the molar-volume conversion in Eq. (21). Stomatal conductance follows the Ball–Berry formulation in Eq. (22), with the water-stress adjustment in Eqs. (23) and (24). Residual stomatal conductance g_0 (mol m^{-2} s^{-1}) is used for non-positive net assimilation.

A3. Temperature responses and physiological parameters

The coefficients governing photosynthesis and respiration are updated with leaf temperature. The following Arrhenius function is applied to K_c, K_o, CO_2/O_2 specificity $S_{c/o}$, and R_d:

$$q(T_{\mathrm{veg}}) = q_{ref} \exp\left[\frac{E_a}{R_{gas}}\left(\frac{1}{T_{ref}} - \frac{1}{T_{veg}}\right)\right], \tag{A8}$$

where q represents one of these coefficients, and q_{ref} is its value at the reference temperature T_{ref} = 298.16 K. T_{veg} is leaf temperature (K), E_a is the temperature-response energy (J mol^{-1}), and R_{gas} is the universal gas constant (8.314 J mol^{-1} K^{-1}). $S_{c/o}$ is a dimensionless coefficient describing the relative preference of Rubisco for CO_2 over O_2 and decreases with increasing temperature because its E_a is negative.

V_{cmax} and J_{max} follow a response that peaks at the optimum temperature and decreases at higher temperatures (Medlyn et al., 2002):

$$X(T_{\mathrm{veg}}) = \frac{X_{opt} E_{\mathrm{d}} \exp(E_a \beta)}{E_{\mathrm{d}} - E_a + E_a \exp(E_{\mathrm{d}} \beta)}, \tag{A9}$$

$$\beta = \frac{1}{R_{\mathrm{gas}}}\left(\frac{1}{T_{opt}} - \frac{1}{T_{\mathrm{veg}}}\right), \quad \text{(A10)}$$

where X represents V_{cmax} or J_{max}, and X_{opt} is its value at the optimum temperature T_{opt} = 311 K for the corresponding voxel. In Eq. (A9), E_a and E_d are activation and deactivation energies (J mol^{-1}), respectively, and β has units of mol J^{-1}.

The physiological parameters follow the CANOAK broadleaved-canopy representation and implementation (Harley and Baldocchi, 1995; Baldocchi and Wilson, 2001). The light-response coefficient is set to α_J = 0.22 mol electrons mol^{-1} photons. The vertical variation in photosynthetic capacity is represented by $f_z = 0.35 + 0.65\zeta$, where ζ is voxel height above ground divided by canopy-top height in the same vertical column, constrained to 0–1. The voxel-specific capacities at the optimum temperature are set to $V_{cmax,opt} = 73 f_z$ μmol CO_2 m^{-2} s^{-1} and $J_{max,opt} = 170 f_z$ μmol electrons m^{-2} s^{-1}. Reference respiration is calculated as $R_{d,ref} = 0.004657 V_{cmax,opt}$ and multiplied by 0.4 when I_{PAR} > 10 μmol photons m^{-2} s^{-1}. The seasonal factor was set to 1 during the evaluation periods. The CO_2 compensation point is calculated as $\Gamma^* = C_{O2}/(2S_{c/o})$, with C_{O2} = 210000 μmol mol^{-1}.

A4. Coupling to transpiration and the leaf energy balance

Calculated stomatal conductance is converted to stomatal resistance using Eq. (21). Together with leaf boundary-layer resistance and the leaf-to-air vapor pressure deficit, this resistance is used to calculate latent heat flux LE in Eq. (18). During daytime, leaf temperature determined by the balance among net absorbed radiation, sensible heat flux, and latent heat flux is fed back into the physiological coefficients and photosynthesis–stomatal calculations. This procedure is repeated to solve the leaf energy balance coupled to transpiration and leaf temperature.

Appendix B. Additional leaf-temperature evaluation using observations from Mainz

B1. Observational data and numerical experiments

Additional leaf-temperature evaluation used the dataset reported by Simon et al. (2018) for the Landesmuseum courtyard in Mainz, Germany. The site consists of an approximately 43 × 48 m courtyard surrounded by buildings 10–16 m in height, and the observed tree was Platanus × acerifolia (Fig. B1). Leaf surface temperature was measured using an Arduino-based infrared thermometer equipped with a Melexis MLX90614ESF-DCI sensor, with a 5° field of view and an assumed leaf emissivity of 0.97 (Simon et al., 2018). The reported factory-calibrated accuracy was ±0.5 °C over 0–60 °C, and measurements taken several times per second were averaged over 5 min intervals. The sensor was mounted on a branch approximately 5 m above ground and directed towards a dense leaf cluster approximately 3 m below it. The reported observation area was approximately 540 cm^2 and remained shaded for most of the day. The model calculated the mean and minimum–maximum range of leaf temperatures for vegetation voxels within the estimated observation area at approximately 2 m above ground. The horizontal resolution was 1 m, and LAD was prescribed as 0.6 m^2 m^{-3}. Although the approximate observation area was reported, its precise location and spatial arrangement within the canopy could not be reconstructed from the available information; the voxel selection therefore represents an estimated sampling area rather than an exact match to the observed leaves.

The evaluation periods were 2–3, 6–7, 11–13, and 16–17 August 2015, corresponding to clear-sky, slightly cloudy, mostly cloudy, and fully cloudy conditions, respectively (Fig. B2). Observed leaf temperatures and ENVI-met results were extracted from the figures in Simon et al. (2018). In the original study, air temperature and relative humidity were measured within the courtyard, whereas wind speed and shortwave radiation were obtained from a meteorological station approximately 3 km southwest of the site. Because the site-specific air-temperature and humidity time series were unavailable for the present evaluation, off-site meteorological records were used as forcing for SOLWEIG-LEB. Wind speed was set to 1.3 m s^{-1}, CO_2 concentration to 420 ppm, and soil-water conditions to REW = 1. These off-site meteorological inputs may not fully represent the air conditions surrounding the observed leaves. Downward longwave radiation was estimated from air temperature, humidity, and a solar-radiation-based clearness index. Before sunrise, the index from the same morning was used, whereas the final daytime value was used after sunset. Leaf temperatures were compared with Legacy SOLWEIG ($T_{veg} = T_{air}$), SOLWEIG-LEB, and the ENVI-met results reported by Simon et al. (2018).

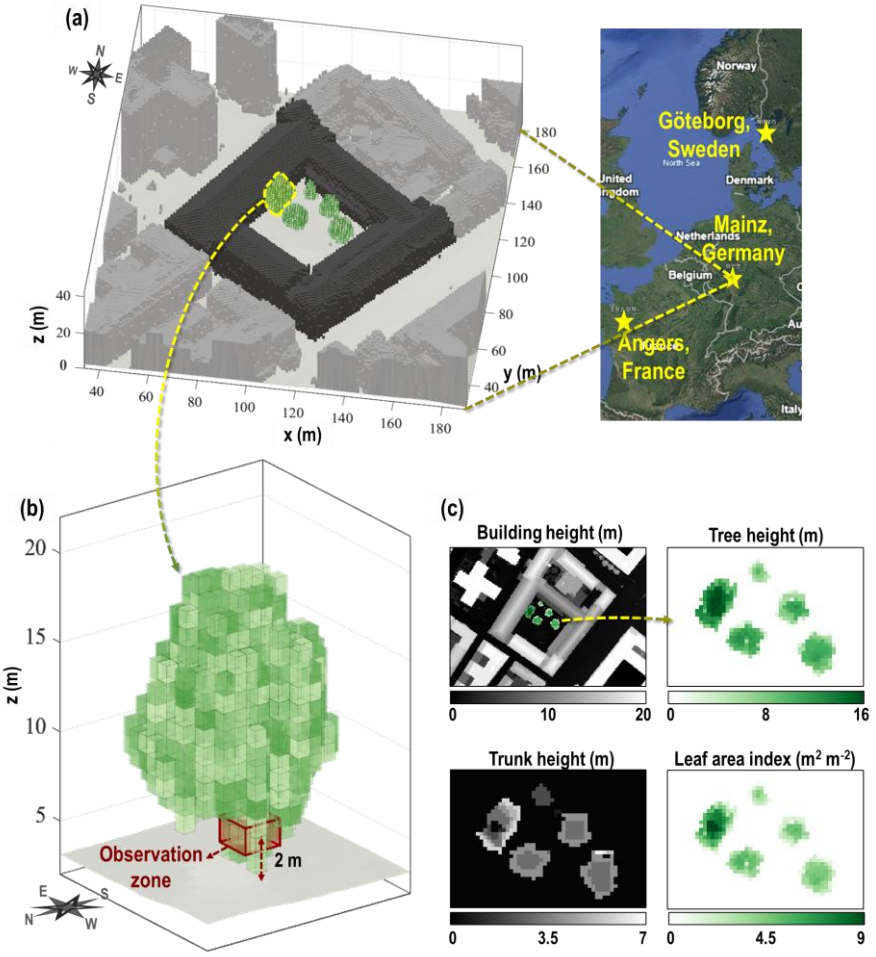

1115 **Figure B1. Mainz site and model domain used for leaf-temperature evaluation. (a) Site location and three-dimensional model domain, (b) vegetation-voxel representation of the evaluated tree and estimated observation zone, and (c) building height, tree height, trunk-zone height, and leaf area index used as model inputs.**

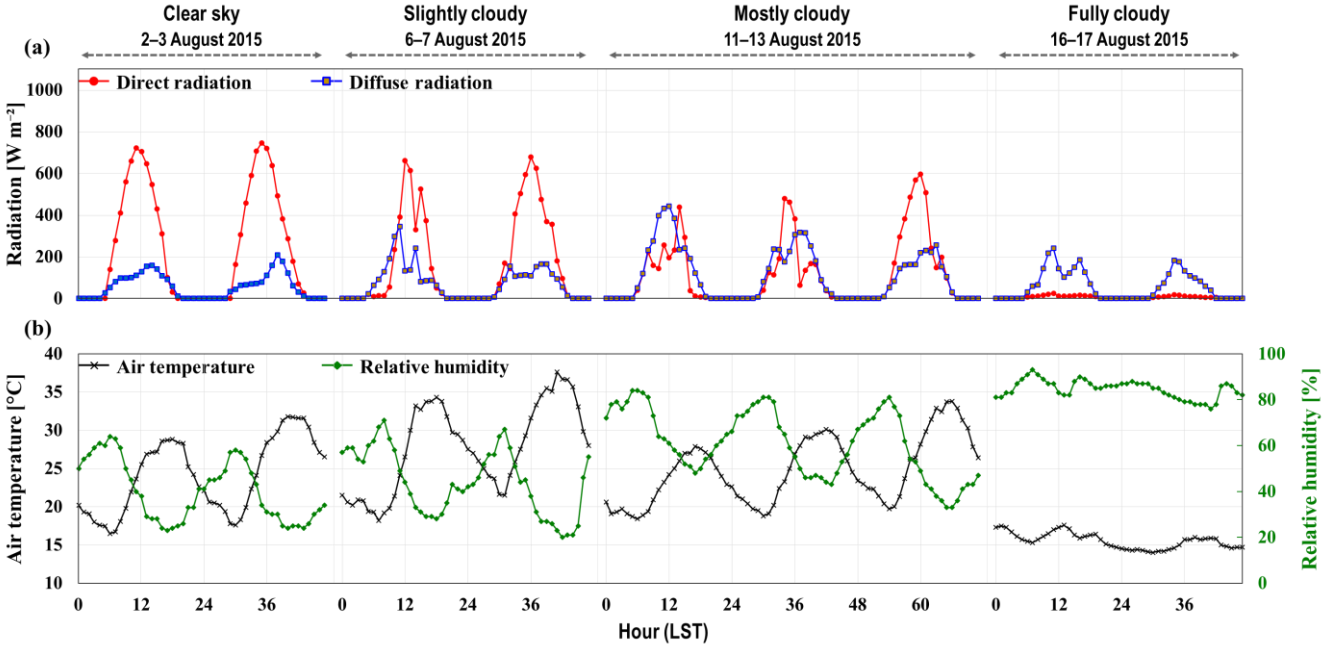

Figure B2. Meteorological forcing used for the Mainz simulations during four evaluation periods: clear-sky (2–3 August 2015), slightly cloudy (6–7 August 2015), mostly cloudy (11–13 August 2015), and fully cloudy (16–17 August 2015). (a) Direct and diffuse shortwave radiation and (b) air temperature and relative humidity.

B2. Leaf-temperature evaluation results

Figure B3 compares observed leaf temperatures with SOLWEIG-LEB, Legacy SOLWEIG, and the ENVI-met results reported by Simon et al. (2018) under four sky conditions. Overall, SOLWEIG-LEB reproduced the diurnal variations in leaf temperature under the different sky conditions and yielded smaller errors than the conventional $T_{veg} = T_{air}$ assumption, particularly under clear-sky and slightly cloudy conditions.

Under clear-sky conditions, pronounced diurnal variations were observed, with daytime leaf-temperature increases under strong solar radiation and cooling at night (Fig. B3a). SOLWEIG-LEB generally reproduced these variations, with an RMSE of 1.23 °C, lower than those of Legacy SOLWEIG (1.56 °C) and ENVI-met (1.42 °C; Table B1). By explicitly calculating the difference between leaf and air temperatures, SOLWEIG-LEB produced results closer to the observed leaf-temperature variations than the conventional isothermal assumption.

Under slightly cloudy conditions, SOLWEIG-LEB also reproduced the increases and decreases in leaf temperature associated with changes in solar radiation reasonably well (Fig. B3b). In particular, it calculated relatively lower leaf temperatures from around noon until after sunset, producing closer agreement with the observed diurnal variation. Accordingly, RMSE decreased from 2.08 °C in Legacy SOLWEIG to 1.45 °C in SOLWEIG-LEB. However, both models overestimated

leaf temperature during some nighttime periods. This is interpreted as reflecting uncertainty in the background meteorological forcing associated with the use of air temperature from a station approximately 3 km away.

Under mostly cloudy conditions, SOLWEIG-LEB reproduced the temporal variation in observed leaf temperature well, with a correlation coefficient of 0.99 (Fig. B3c). However, RMSEs were similar for SOLWEIG-LEB and Legacy SOLWEIG, at 1.20 and 1.19 °C, respectively, indicating no clear reduction in error relative to the conventional air-temperature assumption.

Under fully cloudy conditions, weaker solar heating substantially reduced the diurnal range of leaf temperature (Fig. B3d). SOLWEIG-LEB reproduced these variations, with an RMSE of 1.17 °C, lower than the ENVI-met value of 1.39 °C. However, Legacy SOLWEIG yielded a smaller RMSE of 0.92 °C. At night, the absence of shortwave energy input allows leaf temperature to fall below air temperature depending on the balance among net longwave radiation loss, sensible heat supplied by the air, and latent heat exchange. During this period, observed leaf temperatures were relatively close to the input air temperature, whereas SOLWEIG-LEB exhibited a mean bias of −1.02 °C over the entire evaluation period, calculating slightly lower leaf temperatures than Legacy SOLWEIG, which had a mean bias of −0.83 °C. These differences may be associated with leaf radiative cooling and uncertainties in the background meteorological and downward longwave radiation inputs.

Overall, SOLWEIG-LEB yielded lower RMSEs than ENVI-met under all four sky conditions and reproduced the diurnal variation in leaf temperature more accurately than Legacy SOLWEIG, particularly under clear-sky and slightly cloudy conditions. These improvements were limited under cloudy conditions, indicating that leaf-temperature performance may depend on radiative conditions and the accuracy of the background meteorological forcing.

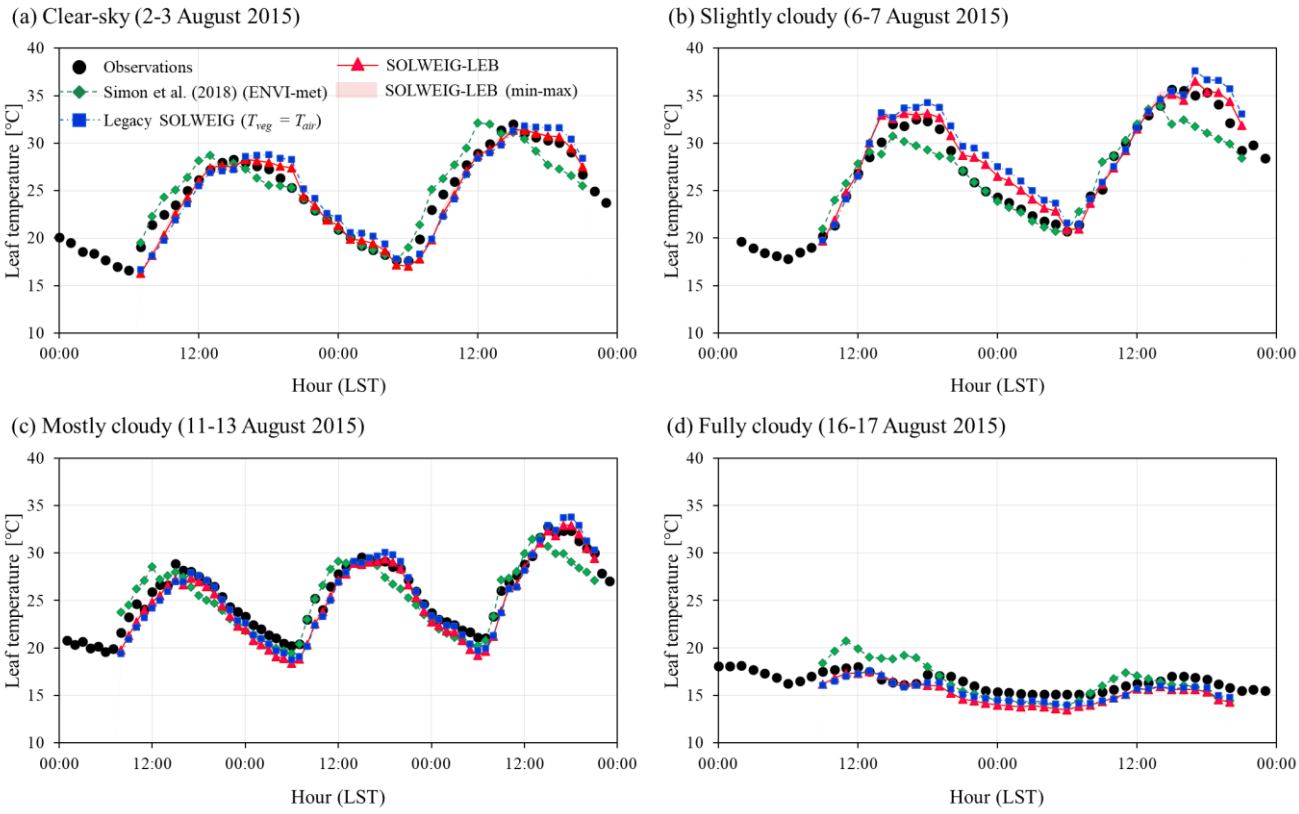

Figure B3. Comparison of observed and simulated leaf temperatures at the Mainz site under (a) clear-sky, (b) slightly cloudy, (c) mostly cloudy, and (d) fully cloudy conditions. Black circles indicate observations, green lines represent the ENVI-met results reported by Simon et al. (2018), blue squares indicate Legacy SOLWEIG (T_{veg} = T_{air}), and red triangles indicate SOLWEIG-LEB. Red shading represents the minimum–maximum range of simulated leaf temperatures within the estimated observation area.

Table B1. Statistical evaluation of leaf temperature at the Mainz site.

Period (2015)	Metric	Simon et al. (2018) (ENVI-met)	Legacy SOLWEIG	SOLWEIG-LEB
Clear-sky	N	39	39	39
08/02–03	r	0.94	0.94	0.97
	RMSE [°C]	1.42	1.56	1.23
	NRMSE	0.10	0.11	0.09
	MBE [°C]	0.18	-0.09	-0.34
Slightly cloudy	N	37	37	37
08/06–07	r	0.95	0.96	0.97
	RMSE [°C]	1.84	2.08	1.45
	NRMSE	0.12	0.13	0.09
	MBE [°C]	-0.72	1.47	0.91
Mostly cloudy	N	62	62	62
08/11–13	r	0.91	0.98	0.99
	RMSE [°C]	1.54	1.19	1.20
	NRMSE	0.12	0.09	0.10
	MBE [°C]	-0.55	-0.60	-0.89
Fully cloudy	N	36	36	36
08/16–17	r	0.77	0.91	0.89
	RMSE [°C]	1.39	0.92	1.17
	NRMSE	0.48	0.32	0.40
	MBE [°C]	0.21	-0.83	-1.02

Appendix C. Sensitivity of MRT to canopy and grid configurations in Göteborg

C1. Sensitivity experiment design

We compared changes in mean radiant temperature (MRT) associated with leaf area density (LAD), leaf orientation distribution, horizontal grid resolution, and fixed canopy transmissivity in Göteborg. Except for the changes specified in each experiment, all other model inputs were held constant.

(i) Leaf area density. To isolate the influence of leaf area per unit canopy volume on direct solar radiation attenuation, we held the canopy geometry and the spherical leaf orientation distribution (G_{proj} = 0.5) constant and assigned uniform LAD values of 0.2, 0.4, 0.6, 0.8, and 1.0 $m^2\ m^{-3}$ within the canopy. MRT was extracted at the original OP1 and OP2 coordinates for each condition. Changes in direct shortwave transmissivity were also compared at OP1 at 10:00 LST on 23 May and at OP2 at 14:00 LST on 7 July, when canopy shading occurred.

(ii) Leaf orientation distribution. The leaf projection function G_{proj} is the mean projected leaf area per unit leaf area, with the projection taken onto a plane perpendicular to the direction of radiation (Zeng et al., 2015). LAD was held at 0.6 $m^2\ m^{-3}$, and four leaf orientation distributions were considered: spherical, horizontal, vertical, and 45° inclined (Fig. C1a–d). For the spherical distribution, G_{proj} = 0.5 regardless of solar position. For the other three distributions, the leaf inclination angle was fixed, and leaf azimuths within each voxel were assumed to be uniformly distributed. The dependence of G_{proj} on solar elevation is expressed as follows:

$$G_{proj}(\eta,\gamma) = \frac{1}{2\pi}\int_0^{2\pi}|\sin\eta\cos\gamma + \cos\eta\sin\gamma\cos\varphi|d\varphi \quad \text{(C1)}$$

Here, η is the solar elevation angle, γ is the leaf inclination angle relative to the horizontal, and φ is the azimuthal difference between the leaf normal and the direction towards the sun. Equation (C1) represents the azimuthal average of the absolute dot product between the unit leaf normal and the unit vector pointing towards the sun. As solar elevation increases, the projection coefficient increases for horizontal leaves but decreases for vertical leaves (Fig. C1e).

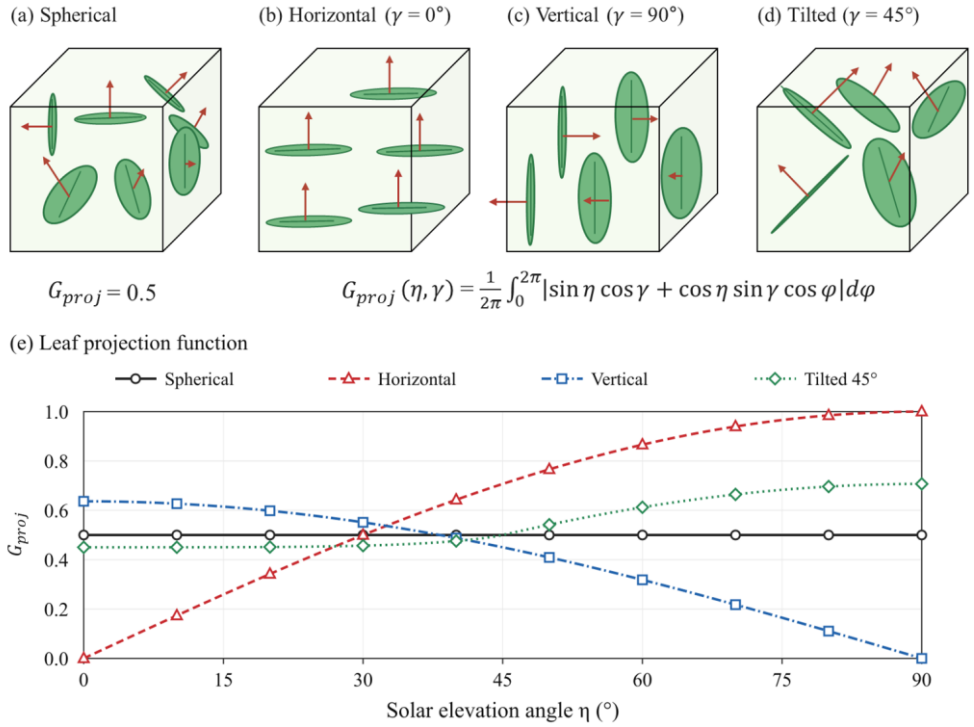

Figure C1. Leaf orientation distributions and the leaf projection function as a function of solar elevation. (a) Spherical, (b) horizontal, (c) vertical, and (d) 45° inclined leaf orientations, showing leaves and their normal vectors (red arrows). (e) Variation in G_{proj} with solar elevation angle η for the four distributions. Leaf azimuths were assumed to be uniformly distributed within each voxel for the vertical and 45° inclined distributions.

(iii) Horizontal grid resolution and sampling locations. To preserve the canopy geometry represented by the original 2 m grid as closely as possible, each original cell was subdivided into sixteen 0.5 m cells or four 1 m cells, while retaining the original canopy-top height, canopy-base height, and LAI. The 4 m grid was constructed by aggregating four adjacent 2 m cells. If any constituent cell contained canopy, the aggregated cell was classified as vegetated and assigned the maximum canopy-top height and minimum canopy-base height among the canopies it contained. LAI was calculated as an area-weighted mean including non-vegetated cells to conserve the total leaf area.

At each resolution, we examined the centres of non-building grid cells within a 3 m radius of the original OP1 and OP2 coordinates and extracted the MRT time series at the location yielding the lowest RMSE relative to observed MRT (Fig. C2).

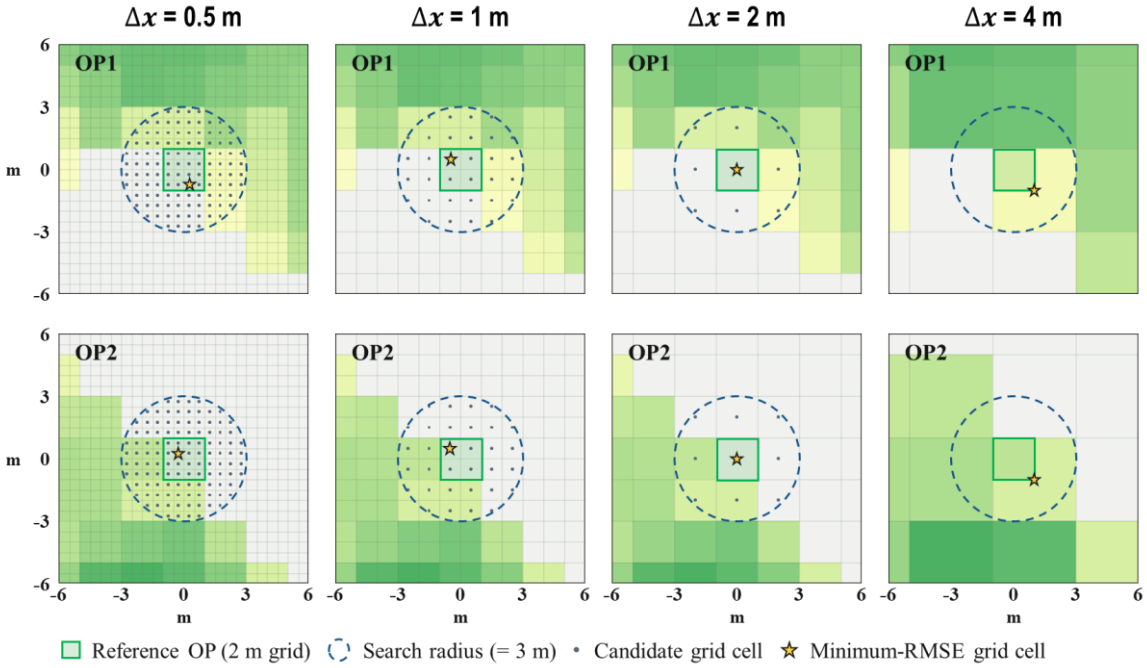

Figure C2. Canopy representation and candidate MRT sampling locations at OP1 (top) and OP2 (bottom) for horizontal grid resolutions of 0.5, 1.0, 2.0, and 4.0 m (left to right). Shades of green indicate canopy-top height, green squares mark the reference observation cells on the original 2.0 m grid, dashed circles show the 3 m search radius, dots indicate candidate sampling cells, and stars mark the minimum-RMSE cells.

(iv) Fixed canopy transmissivity in Legacy SOLWEIG. We compared the default fixed canopy transmissivity of 3 % in Legacy SOLWEIG with values of 5, 10, 20, 30, and 40 % for canopy-shaded locations. In each experiment, a single transmissivity value was applied uniformly to the entire canopy, while the meteorological inputs and canopy geometry were held constant.

C2. Sensitivity experiment results

Figure C3 compares MRT time series at OP1 on 23 May and at OP2 on 7, 10, and 12 July. The pooled RMSE was calculated from 41 paired observations and simulations across both sites (11 at OP1 and 30 at OP2).

(i) Leaf area density (Fig. C3a). Differences in MRT among LAD conditions occurred mainly from 06:00 to 11:00 LST at OP1 and during daytime hours other than 08:00–10:00 LST at OP2. During periods of canopy shading, lower LAD resulted in higher MRT, with particularly pronounced overestimation relative to observations at 0.2 m^2 m^{-3}. At OP1 at 10:00 LST on 23 May, increasing LAD from 0.2 to 0.6 m^2 m^{-3} reduced direct shortwave transmissivity from 0.357 to 0.045, downward shortwave radiation from 330.45 to 139.99 W m^{-2}, and MRT from 38.21 to 26.64 °C. At OP2 at 14:00 LST on 7 July, direct shortwave transmissivity likewise decreased from 0.151 to 0.003, and MRT decreased from 29.34 to 23.90 °C. At

both times, most direct solar radiation was already attenuated at an LAD of 0.6 m^2 m^{-3}, so further increases in LAD produced only small changes in MRT. The pooled RMSEs at LAD values of 0.2, 0.4, 0.6, 0.8, and 1.0 m^2 m^{-3} were 8.01, 5.05, 4.40, 4.31, and 4.36 °C, respectively, with differences of less than 0.1 °C over the range 0.6–1.0 m^2 m^{-3}.

(ii) Leaf orientation distribution (Fig. C3b). The diurnal variations in MRT were generally similar among the four leaf orientation distributions, but substantial differences occurred when the canopy partially attenuated direct solar radiation or when conditions transitioned between sun and shade. These differences appeared around 07:00 and 11:00 LST at OP1 on 23 May and around 06:00 and 11:00 LST at OP2 on 7 July. At OP1 at 11:00 LST on 23 May, the leaf projection coefficient was higher for horizontal leaves (0.76) than for vertical leaves (0.42), while direct shortwave transmissivity was lower (0.18 versus 0.39). Downward shortwave radiation was 244.18 and 371.04 W m^{-2} for horizontal and vertical leaves, respectively, and the corresponding MRT values were 32.33 and 38.27 °C, a difference of approximately 5.9 °C. By contrast, differences among leaf orientations were small when direct solar radiation was almost unattenuated or largely blocked. The pooled RMSE ranged from 4.40 to 4.55 °C over the full observation period, and no leaf orientation distribution consistently yielded the lowest error at both sites.

(iii) Horizontal grid resolution and sampling locations (Fig. C3c). At each resolution, the grid-cell centre with the lowest RMSE was selected within a 3 m radius of the original observation point. At grid resolutions of 0.5, 1, 2, and 4 m, the RMSEs at OP1 were 3.49, 3.62, 3.69, and 4.37 °C, respectively, while those pooled over the three observation days at OP2 were 4.82, 4.79, 4.61, and 4.23 °C. At OP2, the resolution that gave the closest agreement with observations also varied with time. At 11:00 LST on 7 July, direct shortwave transmissivity was 0.55 on the 0.5 and 1 m grids and 0.30 on the 2 and 4 m grids. Simulated MRT was approximately 36 °C on the two finer grids and 31–32 °C on the two coarser grids; the finer-grid results were closer to the observed value of 41.61 °C. In contrast, at 10:00 LST on 12 July, direct solar radiation was unattenuated on the 0.5–2 m grids, yielding MRT values of 54.61–54.81 °C. On the 4 m grid, direct shortwave transmissivity was 0.61 and MRT was 46.21 °C, closer to the observed value of 45.36 °C.

(iv) Fixed canopy transmissivity in Legacy SOLWEIG (Fig. C3d). In Legacy SOLWEIG, higher fixed transmissivity resulted in higher MRT during periods of canopy shading. At OP1 at 10:00 LST on 23 May, increasing transmissivity from 3 % to 40 % raised downward shortwave radiation from 125.55 to 351.69 W m^{-2} and MRT from 25.78 to 40.26 °C. At OP2 at 14:00 LST on 7 July, MRT likewise increased from 24.45 to 36.08 °C. The fixed transmissivity yielding the closest agreement with observations differed between the sites: 10 % at OP1 (RMSE = 2.98 °C) and 3 % at OP2 (RMSE = 5.07 °C). Across the same 41 observation–simulation pairs, the pooled RMSE for the six fixed-transmissivity cases ranged from 4.76 to 10.06 °C, compared with 4.38 °C for the Full LEB configuration.

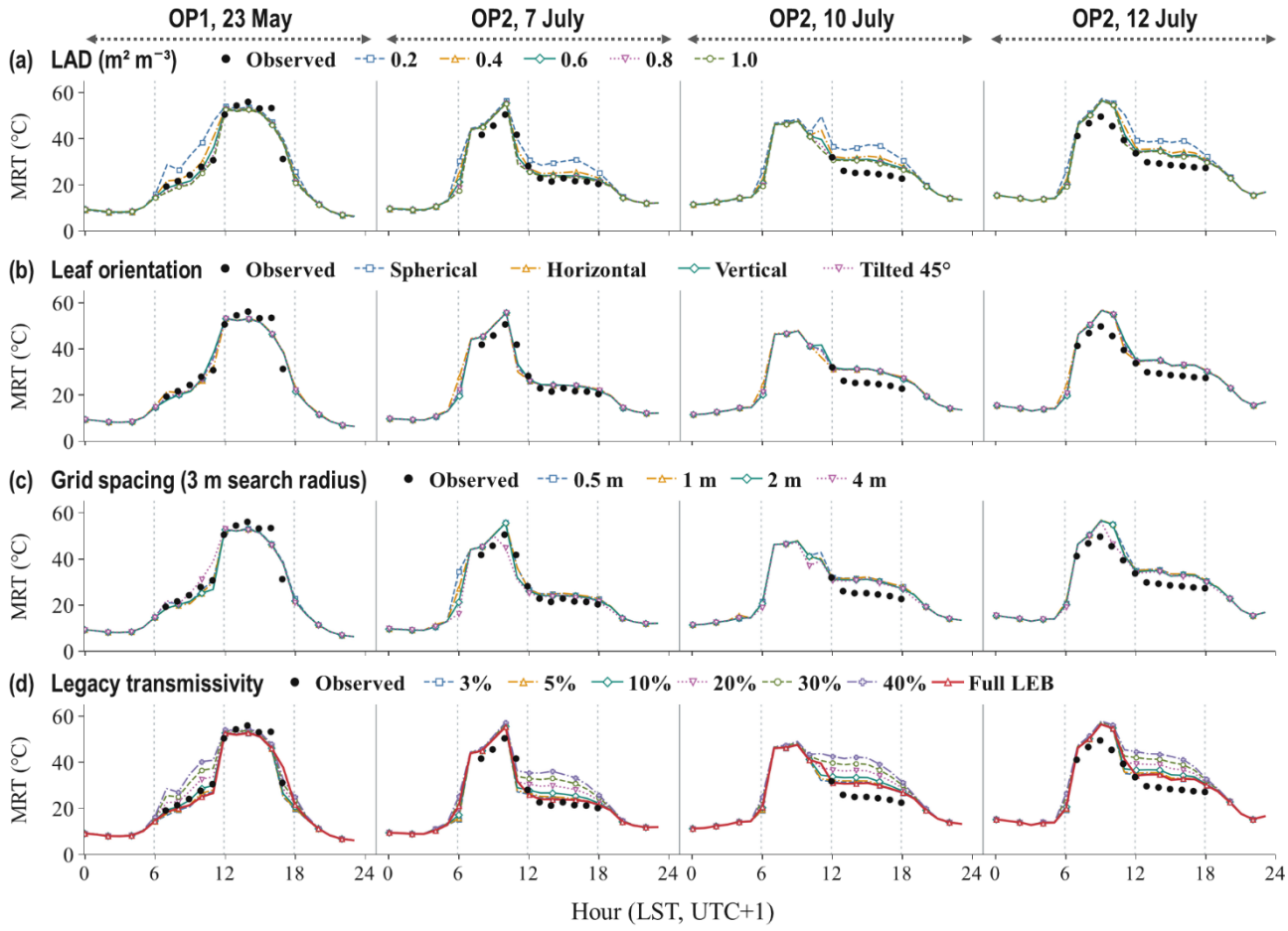

Figure C3. MRT time series for four observation days in Göteborg. From left to right, the columns show OP1 on 23 May and OP2 on 7, 10, and 12 July; black circles indicate observations. (a) Uniform LAD, (b) leaf orientation distribution, (c) horizontal grid resolution, and (d) fixed canopy transmissivity in Legacy SOLWEIG and the reference Full LEB simulation. Panel (c) uses sampling locations reselected within a 3 m radius, whereas panels (a), (b), and (d) use the original OP coordinates. All times are local standard time (LST, UTC+1).

C3. Implications, limitations, and future work

When evaluating radiative shielding by tree canopies, errors averaged over the full observation period should be distinguished from differences occurring when direct solar radiation partially penetrates the canopy. At the two representative times, direct shortwave transmissivity was already 0.05 or lower at an LAD of 0.6 m^2 m^{-3}, and further increases in LAD therefore produced little change in MRT. In contrast, during transitions between sun and shade, MRT varied with leaf orientation even at the same LAD. Furthermore, the fixed transmissivity that best matched observations at one site did not necessarily perform best at the other. This indicates that a single transmissivity value cannot readily represent the shading conditions at both sites and highlights the importance of distinguishing attenuation according to solar position and the radiative path through the canopy.

This comparison was limited to four observation days at two sites, and neither LAD nor leaf orientation distributions were measured directly for the individual canopies. The 0.5 and 1 m grids were generated by subdividing the original 2 m data and therefore did not incorporate additional fine-scale detail of the actual canopy boundaries. Moreover, because the same observations were used both to select sampling locations and to evaluate errors, the RMSEs obtained after reselection cannot by themselves establish the superiority of a particular grid resolution. Future evaluations should use measured high-resolution three-dimensional canopy geometry together with observations of within-canopy leaf density and orientation, keep the sampling locations fixed, and compare the timing of sun–shade transitions and MRT using independent observation days.

Code and data availability

Software name: SOLWEIG-LEB v1.0

Developers: Geon Kang, Jae-Jin Kim, Fredrik Lindberg, Eliott Bridoux, and Nils Wallenberg

Contact: Geon Kang (kg85112@gmail.com)

Year first available: 2026

Hardware required: A 64-bit computer with a CUDA-compatible NVIDIA GPU. GPU-memory requirements depend on the model-domain size and vegetation-voxel configuration.

Software required: Python 3.12, CUDA 12.x, CuPy 13.3.0, GDAL 3.6 or later, and the dependencies specified in environment.yml. The archived release was tested on Windows 11.

Programming language: Python with GPU acceleration via CuPy/CUDA

Program size: Approximately 243 MB compressed and 246 MB uncompressed (code and data)

Availability and cost: Open source and free of charge

License: GNU General Public License v3.0 or later (GPL-3.0-or-later)

Repository: Zenodo (Kang et al., 2026), https://doi.org/10.5281/zenodo.21904277

Data availability: The original model inputs, configurations, evaluation data, and postprocessing scripts are available in the Zenodo archive (Kang et al., 2026). The Angers observations are available from the Earth System Data Repository (Herpin et al., 2024).

Author contributions

GK conceived the study, developed and implemented SOLWEIG-LEB, performed the simulations, model evaluation, data analysis, post-processing, and visualization, and prepared the original manuscript. FL and NW contributed to the model conceptualization and methodology, provided technical guidance on the SOLWEIG framework, and reviewed and edited the manuscript. EB provided the observational and spatial data for the Göteborg evaluation, provided information on the measurement setup and study site, and reviewed and edited the manuscript. JJK supervised the study, acquired funding, provided scientific guidance and project administration, and reviewed and edited the manuscript. All authors reviewed and approved the final manuscript.

Competing interests

The contact author has declared that none of the authors has any competing interests.

Acknowledgements

During the preparation of this work, the authors used Google Gemini and OpenAI ChatGPT to improve language, readability, and textual organization. OpenAI Codex was used to assist with code review, debugging, and the implementation of GPU/CUDA parallelization. All AI-assisted text and code modifications were reviewed, edited, and validated by the authors. The authors take full responsibility for the content, source code, results, and conclusions of the publication.

Financial support

This work was supported by the National Research Foundation of Korea (NRF) grant funded by the Korea government (MSIT) (RS-2024-00341302) and by the Basic Science Research Program through the National Research Foundation of Korea (NRF) funded by the Ministry of Education (RS-2025-02317416).

References

Armson, D., Stringer, P., and Ennos, A. R.: The effect of tree shade and grass on surface and globe temperatures in an urban area, Urban For. Urban Green., 11, 245–255, https://doi.org/10.1016/j.ufug.2012.05.002, 2012.

Asawa, T., Oshio, H., and Yoshino, Y.: Comparison Between Thermal-Image-Based and Model-Based Indices to Detect the Impact of Soil Drought on Tree Canopy Temperature in Urban Environments, Remote Sens., 16, 4606, https://doi.org/10.3390/rs16234606, 2024.

Baldocchi, D.: A Lagrangian random-walk model for simulating water vapor, CO_2 and sensible heat flux densities and scalar profiles over and within a soybean canopy, Bound.-Lay. Meteorol., 61, 113–144, https://doi.org/10.1007/BF02033998, 1992.

Baldocchi, D.: An analytical solution for coupled leaf photosynthesis and stomatal conductance models, Tree Physiol., 14, 1069–1079, https://doi.org/10.1093/treephys/14.7-8-9.1069, 1994.

Baldocchi, D. D.: Measuring and modelling carbon dioxide and water vapour exchange over a temperate broad-leaved forest during the 1995 summer drought, Plant Cell Environ., 20, 1108–1122, https://doi.org/10.1046/j.1365-3040.1997.d01-147.x, 1997.

Baldocchi, D. D. and Bowling, D. R.: Modelling the discrimination of $^{13}CO_2$ above and within a temperate broad-leaved forest canopy on hourly to seasonal time scales, Plant Cell Environ., 26, 231–244, https://doi.org/10.1046/j.1365-3040.2003.00953.x, 2003.

Baldocchi, D. D. and Harley, P. C.: Scaling carbon dioxide and water vapour exchange from leaf to canopy in a deciduous forest. II. Model testing and application, Plant Cell Environ., 18, 1157–1173, https://doi.org/10.1111/j.1365-3040.1995.tb00626.x, 1995.

Baldocchi, D. D. and Wilson, K. B.: Modeling CO_2 and water vapor exchange of a temperate broadleaved forest across hourly to decadal time scales, Ecol. Model., 142, 155–184, https://doi.org/10.1016/S0304-3800(01)00287-3, 2001.

Błażejczyk, K., Broede, P., Fiala, D., Havenith, G., Holmér, I., Jendritzky, G., Kampmann, B., and Kunert, A.: Principles of the new Universal Thermal Climate Index (UTCI) and its application to bioclimatic research in European scale, Misc. Geogr., 14, 91–102, https://doi.org/10.2478/mgrsd-2010-0009, 2010.

Bruse, M. and Fleer, H.: Simulating surface–plant–air interactions inside urban environments with a three dimensional numerical model, Environmental modelling & software, 13, 373–384, https://doi.org/10.1016/s1364-8152(98)00042-5, 1998.

Campbell, G. S.: Extinction coefficients for radiation in plant canopies calculated using an ellipsoidal inclination angle distribution, Agr. Forest Meteorol., 36, 317–321, https://doi.org/10.1016/0168-1923(86)90010-9, 1986.

Campbell, G. S. and Norman, J. M.: An introduction to environmental biophysics, 2nd edn., Springer, New York, NY, https://doi.org/10.1007/978-1-4612-1626-1, 2000.

Collatz, G. J., Ball, J. T., Grivet, C., and Berry, J. A.: Physiological and environmental regulation of stomatal conductance, photosynthesis and transpiration: a model that includes a laminar boundary layer, Agr. Forest Meteorol., 54, 107–136, https://doi.org/10.1016/0168-1923(91)90002-8, 1991.

Farquhar, G. D., von Caemmerer, S., and Berry, J. A.: A biochemical model of photosynthetic CO_2 assimilation in leaves of C_3 species, Planta, 149, 78–90, https://doi.org/10.1007/BF00386231, 1980.

Fröhlich, D. and Matzarakis, A.: Spatial estimation of thermal indices in urban areas—basics of the SkyHelios model, Atmosphere, 9, 209, https://doi.org/10.3390/atmos9060209, 2018.

Granier, A., Bréda, N., Biron, P., and Villette, S.: A lumped water balance model to evaluate duration and intensity of drought constraints in forest stands, Ecol. Model., 116, 269–283, https://doi.org/10.1016/S0304-3800(98)00205-1, 1999.

Harley, P. C. and Baldocchi, D. D.: Scaling carbon dioxide and water vapour exchange from leaf to canopy in a deciduous forest. I. Leaf model parametrization, Plant Cell Environ., 18, 1146–1156, https://doi.org/10.1111/j.1365-3040.1995.tb00625.x, 1995.

Helletsgruber, C., Gillner, S., Gulyás, Á., Junker, R. R., Tanács, E., and Hof, A.: Identifying tree traits for cooling urban heat islands—a cross-city empirical analysis, Forests, 11, 1064, https://doi.org/10.3390/f11101064, 2020.

Herpin, S., Mballo, S., Manteau, M., Lemesle, D., Boukouya, A., Dubuc, B., Ledroit, L., Cannavo, P., Demotes-Mainard, S., and Bournet, P.-E.: A reduced-scale canyon street to study tree climate benefits: summer 2020 data with well-watered apple trees, Scientific Data, 11, 1015, https://doi.org/10.1038/s41597-024-03650-0, 2024.

Höppe, P.: The physiological equivalent temperature–a universal index for the biometeorological assessment of the thermal environment, Int. J. Biometeorol., 43, 71–75, https://doi.org/10.1007/s004840050118, 1999.

Huang, J., Cedeño-Laurent, J. G., and Spengler, J. D.: CityComfort+: A simulation-based method for predicting mean radiant temperature in dense urban areas, Building and Environment, 80, 84–95, https://doi.org/10.1016/j.buildenv.2014.05.019, 2014.

Johansson, E., Thorsson, S., Emmanuel, R., and Krüger, E.: Instruments and methods in outdoor thermal comfort studies–The need for standardization, Urban Clim., 10, 346–366, https://doi.org/10.1016/j.uclim.2013.12.002, 2014.

Jones, H. G., Archer, N., Rotenberg, E., and Casa, R.: Radiation measurement for plant ecophysiology, Journal of Experimental Botany, 54, 879–889, https://doi.org/10.1093/jxb/erg116, 2003.

Kang, G., Lindberg, F., Bridoux, E., Wallenberg, N., and Kim, J.-J.: SOLWEIG-LEB v1.0: model code, example inputs and postprocessing data (Version 1.0), Zenodo [code and data set], https://doi.org/10.5281/zenodo.21904277, 2026.

Kántor, N., Chen, L., and Gál, C. V.: Human-biometeorological significance of shading in urban public spaces—Summertime measurements in Pécs, Hungary, Landscape and urban planning, 170, 241–255, https://doi.org/10.1016/j.landurbplan.2017.09.030, 2018.

Konarska, J., Lindberg, F., Larsson, A., Thorsson, S., and Holmer, B.: Transmissivity of solar radiation through crowns of single urban trees–application for outdoor thermal comfort modelling, Theor. Appl. Climatol., 117, 363–376, https://doi.org/10.1007/s00704-013-1000-3, 2014.

Krayenhoff, E. S., Christen, A., Martilli, A., and Oke, T. R.: A multi-layer radiation model for urban neighbourhoods with trees, Bound.-Lay. Meteorol., 151, 139–178, https://doi.org/10.1007/s10546-013-9883-1, 2014.

Krč, P., Resler, J., Sühring, M., Schubert, S., Salim, M. H., and Fuka, V.: Radiative Transfer Model 3.0 integrated into the PALM model system 6.0, Geosci. Model Dev., 14, 3095–3120, https://doi.org/10.5194/gmd-14-3095-2021, 2021.

Lau, K. K.-L., Lindberg, F., Rayner, D., and Thorsson, S.: The effect of urban geometry on mean radiant temperature under future climate change: a study of three European cities, Int. J. Biometeorol., 59, 799–814, https://doi.org/10.1007/s00484-014-0898-1, 2015.

Leuzinger, S. and Körner, C.: Tree species diversity affects canopy leaf temperatures in a mature temperate forest, Agr. Forest Meteorol., 146, 29–37, https://doi.org/10.1016/j.agrformet.2007.05.007, 2007.

Lindberg, F. and Grimmond, C. S. B.: The influence of vegetation and building morphology on shadow patterns and mean radiant temperatures in urban areas: model development and evaluation, Theor. Appl. Climatol., 105, 311–323, https://doi.org/10.1007/s00704-010-0382-8, 2011.

Lindberg, F., Holmer, B., and Thorsson, S.: SOLWEIG 1.0–Modelling spatial variations of 3D radiant fluxes and mean radiant temperature in complex urban settings, Int. J. Biometeorol., 52, 697–713, https://doi.org/10.1007/s00484-008-0162-7, 2008.

Lindberg, F., Onomura, S., and Grimmond, C. S. B.: Influence of ground surface characteristics on the mean radiant temperature in urban areas, Int. J. Biometeorol., 60, 1439–1452, https://doi.org/10.1007/s00484-016-1135-x, 2016.

Lv, H., Dermann, A., Dermann, F., Petridis, Z., Köhler, M., and Saha, S.: Comparable diameter resulted in larger leaf area and denser foliage in the park trees than in street trees: A study on Norway maples of Karlsruhe city, Germany, Heliyon, 10, e23647, https://doi.org/10.1016/j.heliyon.2023.e23647, 2024.

Maronga, B., Banzhaf, S., Burmeister, C., Esch, T., Forkel, R., Fröhlich, D., Fuka, V., Gehrke, K. F., Geletič, J., Giersch, S., Gronemeier, T., Groß, G., Heldens, W., Hellsten, A., Hoffmann, F., Inagaki, A., Kadasch, E., Kanani-Sühring, F., Ketelsen, K., Khan, B. A., Knigge, C., Knoop, H., Krč, P., Kurppa, M., Maamari, H., Matzarakis, A., Mauder, M., Pallasch, M., Pavlik, D., Pfafferott, J., Resler, J., Rissmann, S., Russo, E., Salim, M., Schrempf, M., Schwenkel, J., Seckmeyer, G., Schubert, S., Sühring, M., von Tils, R., Vollmer, L., Ward, S., Witha, B., Wurps, H., Zeidler, J., and Raasch, S.: Overview of the PALM model system 6.0, Geosci. Model Dev., 13, 1335–1372, https://doi.org/10.5194/gmd-13-1335-2020, 2020.

Matzarakis, A., Rutz, F., and Mayer, H.: Modelling radiation fluxes in simple and complex environments—application of the RayMan model, Int. J. Biometeorol., 51, 323–334, https://doi.org/10.1007/s00484-006-0061-8, 2007.

Matzarakis, A., Rutz, F., and Mayer, H.: Modelling radiation fluxes in simple and complex environments: basics of the RayMan model, Int. J. Biometeorol., 54, 131–139, https://doi.org/10.1007/s00484-009-0261-0, 2010.

Mayer, H. and Höppe, P.: Thermal comfort of man in different urban environments, Theor. Appl. Climatol., 38, 43–49, https://doi.org/10.1007/bf00866252, 1987.

Medlyn, B. E., Dreyer, E., Ellsworth, D., Forstreuter, M., Harley, P. C., Kirschbaum, M. U. F., Le Roux, X., Montpied, P., Strassemeyer, J., Walcroft, A., Wang, K., and Loustau, D.: Temperature response of parameters of a biochemically based model of photosynthesis. II. A review of experimental data, Plant Cell Environ., 25, 1167–1179, https://doi.org/10.1046/j.1365-3040.2002.00891.x, 2002.

Middel, A., Selover, N., Hagen, B., and Chhetri, N.: Impact of shade on outdoor thermal comfort—a seasonal field study in Tempe, Arizona, Int. J. Biometeorol., 60, 1849–1861, https://doi.org/10.1007/s00484-016-1172-5, 2016.

Miller, B. D., Carter, K. R., Reed, S. C., Wood, T. E., and Cavaleri, M. A.: Only sun-lit leaves of the uppermost canopy exceed both air temperature and photosynthetic thermal optima in a wet tropical forest, Agr. Forest Meteorol., 301–302, 108347, https://doi.org/10.1016/j.agrformet.2021.108347, 2021.

Morakinyo, T. E. and Lam, Y. F.: Simulation study on the impact of tree-configuration, planting pattern and wind condition on street-canyon's micro-climate and thermal comfort, Building and environment, 103, 262–275, https://doi.org/10.1016/j.buildenv.2016.04.025, 2016.

Moser-Reischl, A., Franceschi, E., Rahman, M. A., Rodrigues-Leite, J., Pretzsch, H., Pauleit, S., and Rötzer, T.: Spatial and temporal dynamics of the leaf area index (LAI) of selected tree species in urban environments, Urban For. Urban Green., 107, 128795, https://doi.org/10.1016/j.ufug.2025.128795, 2025.

Moser, A., Rötzer, T., Pauleit, S., and Pretzsch, H.: Structure and ecosystem services of small-leaved lime (Tilia cordata Mill.) and black locust (Robinia pseudoacacia L.) in urban environments, Urban For. Urban Green., 14, 1110–1121, https://doi.org/10.1016/j.ufug.2015.10.005, 2015.

Nice, K. A., Coutts, A. M., and Tapper, N. J.: Development of the VTUF-3D v1.0 urban micro-climate model to support assessment of urban vegetation influences on human thermal comfort, Urban Clim., 24, 1052–1076, https://doi.org/10.1016/j.uclim.2017.12.008, 2018.

Oke, T. R.: Boundary layer climates, 2nd edn., Routledge, London, https://doi.org/10.4324/9780203407219, 2002.

Park, C. Y., Lee, D. K., Krayenhoff, E. S., Heo, H. K., Hyun, J. H., Oh, K., and Park, T. Y.: Variations in pedestrian mean radiant temperature based on the spacing and size of street trees, Sustain. Cities Soc., 48, 101521, https://doi.org/10.1016/j.scs.2019.101521, 2019.

Park, C. Y., Lee, D. K., Krayenhoff, E. S., Heo, H. K., Ahn, S., Asawa, T., Murakami, A., and Kim, H. G.: A multilayer mean radiant temperature model for pedestrians in a street canyon with trees, Building and Environment, 141, 298–309, https://doi.org/10.1016/j.buildenv.2018.05.058, 2018.

Ross, J.: The radiation regime and architecture of plant stands, Springer, Dordrecht, https://doi.org/10.1007/978-94-009-8647-3, 2012.

Ryu, Y.-H., Bou-Zeid, E., Wang, Z.-H., and Smith, J. A.: Realistic representation of trees in an urban canopy model, Bound.-Lay. Meteorol., 159, 193–220, https://doi.org/10.1007/s10546-015-0120-y, 2016.

Scholz, T., Hof, A., and Schmitt, T.: Cooling effects and regulating ecosystem services provided by urban trees—novel analysis approaches using urban tree cadastre data, Sustainability, 10, 712, https://doi.org/10.3390/su10030712, 2018.

Schuepp, P. H.: Tansley Review No. 59. Leaf boundary layers, New Phytol., 125, 477–507, https://doi.org/10.1111/j.1469-8137.1993.tb03898.x, 1993.

Simon, H., Lindén, J., Hoffmann, D., Braun, P., Bruse, M., and Esper, J.: Modeling transpiration and leaf temperature of urban trees–A case study evaluating the microclimate model ENVI-met against measurement data, Landscape and urban planning, 174, 33–40, https://doi.org/10.1016/j.landurbplan.2018.03.003, 2018.

Thorsson, S., Lindberg, F., Eliasson, I., and Holmer, B.: Different methods for estimating the mean radiant temperature in an outdoor urban setting, Int. J. Climatol., 27, 1983–1993, https://doi.org/10.1002/joc.1537, 2007.

Wallenberg, N., Holmer, B., Lindberg, F., and Rayner, D.: An anisotropic parameterization scheme for longwave irradiance and its impact on radiant load in urban outdoor settings, Int. J. Biometeorol., 67, 633–647, https://doi.org/10.1007/s00484-023-02441-3, 2023.

Wallenberg, N., Lindberg, F., Holmer, B., and Thorsson, S.: The influence of anisotropic diffuse shortwave radiation on mean radiant temperature in outdoor urban environments, Urban Clim., 31, 100589, https://doi.org/10.1016/j.uclim.2020.100589, 2020.

Wallenberg, N., Holmer, B., Lindberg, F., Lönn, J., Maesel, E., and Rayner, D.: A simple step heating approach for wall surface temperature estimation in the SOlar and LongWave Environmental Irradiance Geometry (SOLWEIG) model, Geosci. Model Dev., 19, 1321–1336, https://doi.org/10.5194/gmd-19-1321-2026, 2026.

Zeng, Y., Li, J., Liu, Q., Hu, R., Mu, X., Fan, W., Xu, B., Yin, G., and Wu, S.: Extracting leaf area index by sunlit foliage component from downward-looking digital photography under clear-sky conditions, Remote Sens., 7, 13410–13435, https://doi.org/10.3390/rs71013410, 2015.

de Wit, C. T.: Photosynthesis of leaf canopies, Agricultural Research Reports, 663, Pudoc, Wageningen, https://edepot.wur.nl/187115, 1965.